UNIVERSITEIT VAN PRETORIA
UNIVERSITY OF PRETORIA
YUNIBESITHI YA PRETORIA

Experimental investigation of free-surface jet-impingement cooling by means of TiO_2-water nanofluids

by

Nicolas Wilken

Submitted in partial fulfilment of the requirements for the degree

MASTER OF ENGINEERING

Department of Mechanical and Aeronautical Engineering

University of Pretoria

December 2019

Supervisors: Prof M. Sharifpur and Prof J.P. Meyer

Abstract

Title: Experimental investigation of free-surface jet-impingement cooling by means of TiO_2-water nanofluid

Supervisors: Prof M. Sharifpur and Prof J.P. Meyer

Department: Mechanical and Aeronautical Engineering

Degree: Master of Engineering (Mechanical Engineering)

The exponential advancements in the field of electronics and power generation have resulted in increased pressure on the thermal management of these systems where the desire for enhanced heat transfer is prevalent. A technique for enhancing heat transfer that has gained sufficient attention over the past two decades is to suspend nano-sized metallic particles in a base fluid in order to enhance its thermophysical properties. Fluids produced in such a manner are commonly termed nanofluids. Due to the promising heat transfer capabilities of nanofluids, many industrial applications are beginning to implement these fluids in their thermal practices. One of the potential applications where nanofluids may be used which has received a great deal of research attention is jet-impingement heat transfer. Concerning the existing publications on nanofluid jet impingement, most works within the steady state regime are limited to the cooling of Al_2O_3-water nanofluids, while transient studies do not account for cooling without the effects of boiling phenomena and for surfaces other than steel.

In this study, six particle volume fractions of TiO_2-water ranging between 0.025 and 1% were prepared and characterised for appropriate cooling tests. The study was conducted within both the steady and transient state with the main objective of evaluating the thermal performance of the selected nanofluid and to determine the optimum particle concentration for jet-impingement cooling applications. Therefore, an experimental rig was designed and manufactured where a copper target surface of 42 mm was impinged upon by a 1.65 mm orifice nozzle at a non-dimensional nozzle-to-target height of 4. The results indicated that the use of nanofluids in impingement applications produced adverse effects, depending on the particle fraction considered.

With respect to the steady-state cooling tests, the copper surface was subjected to a constant heat flux of 145 watt and cooled by the different fluids at Reynolds numbers ranging between approximately 10 000 and 30 000. A maximum enhancement of 14.75% was observed in the measured Nusselt numbers, which occurred at a particle volume concentration of 0.05%. When increasing the volume fraction above 0.1%, unfavourable effects were observed for the heat transfer of the system in comparison with the base case tests of DI-water. Such trends were characterised by the trade-off between the enhancement in thermal conductivity and viscosity, both of which were increased with an increase in particle concentration. As for the effect of Reynolds number on the resulting thermal performance, a directly proportional relation was shown and could be described by the forced convection effect. The transient impingement tests showed that particle concentrations less than 0.1% produced an enhancement in cooling efficiency, while those of higher volume fractions showed negative effects. According to these tests the maximum enhancement was also obtained at a volume fraction of 0.05% and produced an average cooling efficiency enhancement of 16%.

The results of the investigation clearly showed that the use of TiO_2-water nanofluids in jet-impingement cooling applications produced thermal enhancement depending on the selected particle concentration.

Publication

Journal paper

N. Wilken, M. Sharifpur, J.P. Meyer; Experimental investigation of free-surface jet-impingement cooling by means of TiO_2-water nanofluid, under preparation.

Acknowledgements

I would like to thank my supervisors, Prof M. Sharifpur and Prof J.P. Meyer, for the guidance offered during this research. I would also like to thank Mr C. Govinder and Mr D.M. Keetse, for the assistance, guidance and technical knowledge shared with me during the construction of the experimental rig and the completion of the experimental investigation. Concerning the nanofluid preparation and characterisation, I would like to thank Mr S. Giwa, for all his time and efforts. Additionally, I would like to thank the University of Pretoria and the National Research Foundation for providing me with the opportunity, necessary facilities and required funding to complete this study. Lastly, I would like to thank my family and friends, especially my brother, William Wilken, for all the love, support and assistance during this investigation.

Table of contents

List of figures

List of tables

Nomenclature

Symbols

A	Area	m^2
c_p	Specific heat	$J/kg \cdot K$
C	Concentration	mol/m^3
D or d	Diameter	mm
D_{AB}	Mass diffusivity	m^2/s
e	Electronic charge of particles	C
EB	Energy balance	
h	Heat transfer coefficient	$W/m^2 \cdot K$
H	Nozzle height	mm
I	Current	A
k	Thermal conductivity	$W/m \cdot K$
K_B	Boltzmann constant	J/K
L	Length	m
m	Mass	kg
$\dot{m}$	Mass flow rate	kg/s
$\vec{n}$	Wall normal unit vector	
p	Pressure	Pa
$\dot{q}$	Heat flux	W/m^2
$\dot{Q}$	Rate of heat transfer	W
r	Radius	mm
R	Resistance	Ω
t	Time	s
T	Temperature	°C or K
U	Velocity	m/s
V	Volume	m^3
V	Voltage	V
$\dot{V}$	Volume flow rate	m^3/s

Dimensionless parameters

Pr	Prandtl number
Re	Reynolds number
Nu	Nusselt number
Sc	Schmidt number
Sh	Sherwood number
R_f	Recovery factor
E_f	Impingement cooling/heating effectiveness
M_c	Mach number
I	Turbulence intensity
f	Relative nozzle area
H/D	Nozzle height to nozzle diameter ratio
R/D	Radial position to nozzle diameter ratio
z/D	Axial position to nozzle diameter ratio
p_{jet}/D	Jet pitch to nozzle diameter ratio
A_f	Free area

Greek letters

α	Diffusion coefficient	m^2/s
β	Thermal expansion coefficient	$1/K$
δ_{nl}	Nanolayer thickness	nm
θ	Non-dimensionalised temperature	
η	Intrinsic viscosity	
μ	Dynamic viscosity	$kg/m \cdot s$
ρ	Density	kg/m^3
τ	Thickness	mm
ν	Kinematic viscosity	m^2/s
φ	Volume fraction	%
ϕ	Weight concentration	%

ψ	Sphericity

Subscripts

aw	Adiabatic wall
b	Bulk fluid
bf	Base fluid
nf	Nanofluid
c	Copper
c	Cluster
c	Critical
conv	Convective
e	Equivalent
e	Exit
eff	Effective
esf	Empirical shape factor
electric	Electric
fluid	Fluid
fp	Freezing point
F	Far field
h	Hydraulic
i	Index
max	Maximum
mass	Mass
nl	Nanolayer
np	Nanoparticle
r	Recovery
t	Total
TC	Thermocouple
weight	Weighted
w	Wall
s	Surface
j	Jet

pc	Proportional constant
o	Initial
o	Stagnation
∞	Ambient

Abbreviations

CNT	Carbon nanotube
DI	Deionised
EG	Ethylene glycol
HTF	Heat transfer fluid
IHC	Inverse heat conduction
MWCNT	Multi-walled carbon nanotube
MWNT	Multi-walled nanotube
PG	Propylene glycol
SWNT	Single-walled nanotube
TCNT	Transparent carbon nanotube
TNT	Titania nanotube
UV	Ultraviolet
VIS	Visible

1. Introduction

1.1. Background

Rapid growth within the fields of science and technology as a whole has resulted in tremendous advancements over the past few years. Leading these advancements are advancements in the field of electronics and power generation where heat transfer forms an integral part [1]. In association with these developments, the desire for systems and components to be miniaturised while maintaining or enhancing their overall performance and storage capacity has grown prevalent. Consequently, increased pressure has been placed on the thermal management in these systems and devices, and the demand for enhanced and effective heat transfer is now greater than ever.

The enhancement of heat transfer may be procured through several different means or mechanisms. Some common examples are fluid injection or suction, manipulation of surface size, shape and roughness, the vibration of the heated surface, applying an electrical or magnetic field to the heated surface and increasing the overall temperature gradient in the system. Additionally, some research studies have shifted their focus from modifying the heated surface to rather enhancing the thermal properties of the working fluid. An example of improving the properties of the heat transfer medium dates back to the work of Maxwell [2]. According to Maxwell's theory, the thermal properties of a fluid can be enhanced by scattering solid particles of micro-scaled size in the base fluid. Unfortunately, the use of these particles results in blockages, corrosion and many other unfavourable occurrences.

Due to the advancements of modern-day technology, it is now possible to produce particles of a smaller, nano-scaled size. When these "nanoparticles" are dispersed in a base fluid, the resulting mixture is termed a "nanofluid" and offers many new and exciting possibilities for enhanced heat transfer and thermal performance. Nanofluids have a larger relative surface area, better stability of suspension, reduced erosion within channels and are small enough to behave like fluid molecules and hence eliminate the problem of clogging within small passageways. In addition, these fluids offer a greater heat transfer enhancement than that of the fluids containing micro-sized particles, as proposed by Maxwell. Subsequently, nanofluids have gained substantial research interest and have been considered in a large number of research works where their thermophysical behaviour, as well as potential application in real-life systems, has been considered.

The use of nanofluids has received considerable interest in the field of jet impingement. Impingement cooling is an effective way to generate high cooling rates and therefore remove large heat fluxes. Compared with conventional convective heat transfer, the heat transfer coefficient of jet impingement heat transfer is several times or even magnitudes larger and is thus used in many different fields and industrial practices [3].

According to literature, the thermal properties of the working fluid will greatly affect the heat transfer features of jet-impingement cooling [4]. Conventionally, impingement systems use fluids of low thermal conductivity, such as water or mixtures of water and ethylene glycol (EG), which ultimately limit the system's performance. By introducing nanoparticles into these "base fluids", not only is it possible to modify the thermophysical properties of the working fluid, but it is also possible to enhance the overall heat transfer performance of the impingement cooling process.

1.2. Nanofluid jet impingement

Impinging jets are an established technique used for providing high heat transfer coefficients between the impinging fluid and the target surface. Among the many possible surface-related modifications, it has been found that it is necessary to improve the thermophysical properties of the heat transfer fluid (HTF) in order to enhance the heat transfer performance of jet-impingement cooling.

Nanofluids are an innovative category of fluid produced by suspending nanoparticles within a base fluid in an attempt to create a homogeneous colloid. Due to their enhanced thermal properties, nanofluids may become a promising working fluid of augmenting heat transfer in jet-impingement cooling systems [4]. Over the past two decades, extensive experimental and numerical research has been done on jet impingement heat transfer using nanofluids. In these studies, numerous variables were investigated. However, the main objective was predicting the thermal behaviour and overall suitability of nanofluids in the impingement cooling processes.

Upon comparing the many experimental works already recorded on nanofluid jet impingement, it should be noted that there is a lack of data relating to steady-state jet impingement of varying volume fractions of TiO_2-water nanofluids. Furthermore, with respect to the transient cooling of nanofluid jets, all published works appear to only focus on the steel industry and hence do not present transient data for target surfaces of varying material compositions. Additionally, these transient studies are also limited to cooling with the consideration of boiling effects and do not account for pure convective impingement cooling.

1.3. Problem statement

Despite the substantial number of works focused on jet-impingement cooling by means of nanofluids, there is a significant lack of experimental data for the steady-state impingement of fluids other than Al_2O_3-water. Furthermore, the current library of transient impingement studies are also restricted to only steel surfaces where the effects of boiling phenomena are accounted for. Consequently, there is sufficient research potential for the jet impingement cooling of a non-steel target surface using a non-aluminium nanofluid within both steady and transient state.

1.4. Aim

The purpose of this study was to experimentally investigate the heat transfer characteristics and overall cooling efficiency of varying volume concentrations of TiO_2-water nanofluids for the free-surface jet-impingement cooling of a copper target surface. During the study, both steady- and transient state cooling tests were considered.

1.5. Objectives

The primary objectives of this investigation were as follows:

- to prepare and characterise different volume concentrations of TiO_2-water nanofluids that are of suitable stability for the appropriate jet-impingement cooling tests;
- to obtain the average steady-state heat transfer coefficients and non-dimensional Nusselt numbers for the different particle volume fractions of TiO_2-water at different Reynolds numbers;
- to formulate a reliable correlation capable of predicting the average steady-state Nusselt number as a function of both TiO_2-water volume fraction and Reynolds number;

- to obtain the non-dimensionalised transient cooling curves of the copper target surface for the different particle concentrations of TiO_2-water nanofluids;
- to investigate the influence of Reynolds number on the overall heat transfer performance of steady state jet-impingement cooling;
- to investigate the effect of nanoparticle concentration on the overall heat transfer performance of both steady- and transient state jet-impingement cooling by means of TiO_2-water nanofluids;
- to identify the optimum particle concentration for both steady- and transient state jet impingement cooling by means of TiO2-water nanofluids.

These objectives were met by means of an experimental rig that was designed and manufactured to obtain the required data and information. The experimental system is defined in further detail in Chapter 3.

1.6. Scope of work

The study investigated the overall heat transfer characteristics and cooling performance of TiO_2-water nanofluids in the application of jet-impingement cooling. During the experimental tests, six different volume fractions of nanofluid, namely 0.025, 0.05, 0.01, 0.25, 0.5 and 1%, were considered and compared with a working fluid of pure deionised (DI) water. In addition to investigating the effect of nanoparticle concentration, the influence of Reynolds number on the performance of jet-impingement cooling was also accounted for. For such an exploration, the Reynolds number was varied within the range of 10 000 to 30 000.

A single nozzle diameter and non-dimensional nozzle-to-target surface distance was considered throughout the investigation and thus remained fixed at 1.65 mm and 4 respectively. During the steady-state runs, a constant heat flux was applied to the target surface through an electrical power input of 145 watt. The transient cooling analysis of the copper target surface was initiated once the surface had been heated to a temperature of 105 ℃, at which point the heater power was switched off.

The preparation of the different TiO_2-water nanofluid volume concentrations was conducted using a single-step preparation technique. During this process, a concentrated form of the respective nanofluid was diluted with a calculated volume of water and then subjected to sonication to break down particle agglomeration and ensure the production of a homogeneous colloid. For volume fractions of ≤ 0.1 %, a surfactant of sodium dodecyl sulphate (SDS) was used to enhance fluid stability. This surfactant was mixed into the appropriate fluid samples using a magnetic stirrer. Once a fluid was prepared, it was subjected to viscosity measurements as well as visual stability and constant viscosity versus time stability tests.

Additionally, and as stated in Section 1.5, the scope of the study also involved the design and construction of an experimental rig used for conducting the required investigations.

1.7. Overview of dissertation

The following chapter contains the literature review, in which the fundamental theory of nanofluid design, preparation and characterisation are presented. In addition, the study focuses on the physics and experimental techniques of jet impingement heat transfer. In conjunction with this information, the study also serves as a summary of the various experimental works reporting on jet impingement by means of nanofluid for both steady-state and transient applications.

The constructed experimental set-up, as well as the experimental procedure and data reduction technique, is discussed in Chapter 3. Furthermore, this chapter also presents the overall uncertainties of the relevant variables and parameters, as determined by the uncertainty analysis presented in Appendix B.

In Chapter 4, the preparation technique, as well as the overall characterisation and stability analysis of the various nanofluid mixtures, is provided. Additionally, this chapter also pays attention to the verification of the particle morphology of the TiO_2-nanofluids, as specified by the manufacturer.

Including the validation study of the experimental model, Chapter 5 also presents the experimentally determined heat transfer data for the jet impingement tests for both the steady and transient cases. Following the steady-state test data, the chapter also defines the proposed correlation derived for the prediction of the Nusselt number for free-surface jet impingement through TiO_2-water nanofluid.

The final chapter, Chapter 6, serves as a conclusion of the previous chapters and therefore provides a summary of the investigation and its outcomes. Additionally, the chapter also presents the suggested recommendations for future works and investigations.

Regarding the appendices included in this dissertation, Appendix A is dedicated to the calibration process of the different thermocouples used in the investigation and therefore focuses on the overall process conducted, as well as the resulting calibration factors and calibration tests completed. Appendix B contains the uncertainty analysis for the different variables and parameters used in the data reduction process, as discussed earlier.

2. Literature review

2.1. Introduction

This chapter deals with the fundamental theory of nanofluid design, preparation, stability and thermophysical properties. In addition to the theory of nanofluids, the chapter also highlights the physics of jet impingement heat transfer and summarises major experimental works, both steady and transient, which reported on jet impingement heat transfer using nanofluids.

2.2. Design of nanofluids

A nanofluid may be defined as a suspension of nanoparticles in a base fluid, where the particles have been dispersed in such a way that a homogeneous colloid is obtained [5]. Concerning the general design and composition of nanofluids, the following components are worth defining:

Nanoparticles: Based on the above description of nanofluids, nanoparticles are the solid particles that are suspended or blended in the base fluid in order to produce the new compound termed a "nanofluid". In terms of particle classification, Krajnik et al. [6] define the following particle groups:

- metallic nanoparticles such as Cu, Al, Fe and Ag;
- non-metallic nanoparticles such as Al_2O_3, CuO and ZnO;
- organic nanoparticles such as natural fibres of nano-scaled size. Nanofluids consisting of such particles are referred to as "bio-" or "green" nanofluids.

A schematic representation of a typical nanoparticle is presented in Figure 2.1.

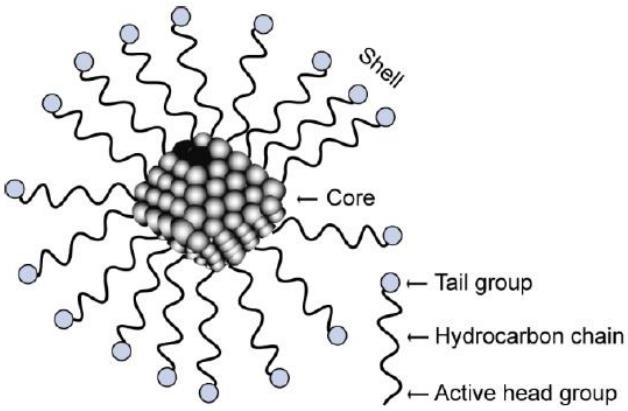

Figure 2.1. Schematic representation of a typical nanoparticle adapted from Das et al. [7]

Figure 2.1 indicates that a typical nanofluid consists of two main structures; a core, either ceramic or metallic, and a thin shell, which is often molecular and divided into three portions, namely a tail group, a hydrocarbon chain and an active head group [7].

In general, most nanofluids are prepared with nanoparticles occupying less than 1% of the overall volume of the fluid mixture. Furthermore, it should be noted that more than one nanoparticle may be used to prepare a nanofluid. Fluids consisting of multiple nanoparticles are termed "hybrid nanofluids".

Base fluid: This is the fluid in which the nanoparticles are suspended or the fluid in which the thermophysical properties are to be enhanced. Some of the fluids that are typically used as base fluids in nanofluid preparation are presented in Table 2.1.

Table 2.1. Common base fluids used in nanofluid preparation

Class of fluid	Examples
Water	Distilled or deionised
Vegetable oils	Coconut or canola oil
Organic liquids	Butanol or ethylene glycol
Polymeric solutions	-

Additives: Due to stability requirements and other external factors, most nanofluids require the addition of additives such as surfactants, corrosion inhibitors, anti-wear additives, disinfectants and fungicides. Of the various additives used in nanofluids, the most important are those used for improving the stability of the nanofluid (surfactants). These additives are discussed in further detail in Section 2.4.2.

Scale: Some effects of nanofluids depend on the size of the particles suspended in the base fluid. These effects are often termed the “volume effects”.

The above factors and parameters are all of great importance when manufacturing or preparing nanofluids because they directly influence the resulting thermophysical and chemical properties of the synthesised fluid. The possible methods typically used to prepare nanofluids are discussed in detail in Section 2.3.

2.3. Preparation of nanofluids

How a nanofluid is prepared contributes significantly to the enhancement of the thermophysical properties of its base fluid, as well as the stability of the prepared nanofluid as a whole. Typically, there are two major methods in nanofluid preparation:

- the single-step method;
- the two-step method.

Of these methods, it is the two-step method that is more commonly used for nanofluid preparation; however, both the single-step and two-step methods are discussed in detail below.

2.3.1. Single-step method

The single-step preparation method is a physical or chemical process, where the synthesis and dispersion of nanoparticles occur simultaneously avoiding processes such as drying, storing and mixing of the nanoparticles in the base fluid [1]. Common examples of these preparation methods are physical and chemical vapour condensation, wet grinding with ball mills, chemical reduction and chemical precipitation [8].

Since particle synthesis and dispersion occur simultaneously, greater uniformity of particles is obtained, as well as reduced particle aggregation. Therefore, the overall nanofluid stability is much better than that obtained through a two-step preparation method. As for feasibility and practicality, the single-step method is not cost-effective and thus not suitable for commercial-scale production. Furthermore, this particular method of preparation is also limited to base fluids with low vapour pressure, according to Ghodsinezhad et al. [8].

2.3.2. Two-step method

During the two-step preparation method, synthesis and dispersion of nanoparticles do not occur simultaneously, but rather through two distinct procedures. During the initial step, dry nanoparticles are synthesised using physical or chemical procedures and then dispersed homogeneously within the base fluid during the second step. Typical devices utilised for adequate nanoparticle dispersion include ultrasonic mixers and homogenisers [5].

Concerning feasibility, this method of preparation may be used for mass production and therefore enables the production of nanofluids in both an affordable and economical manner. Due to these factors, the two-step preparation method is the most common way of formulating nanofluids and is discussed in the works of many researchers.

It should be noted that although the two-step method allows for the affordable production of nanofluids, it is highly susceptible to the agglomeration of the nanoparticles due to the strong intermolecular forces that exist as a direct result of the large particle surface area in comparison with particle volume. Therefore, making a homogeneous dispersion by employing the two-step method remains a challenge.

Irrespective of the preparation method chosen, there is still much room for further research on the preparation of different nanofluids (different particles, different base fluids, etc.). The need for such research is heavily emphasised in the work of Sharifpur and Meyer [5], where the need to understand nanofluid preparation and the resulting nanofluid stability is discussed.

Section 2.4 further elaborates on the topic of nanofluid stability and the corresponding technology and methods associated with this topic of interest.

2.4. Nanofluid stability

Agglomeration is the term used when the particles suspended in a nanofluid begin to stick together or form clusters as a direct result of the Van der Waal's and cohesive forces that exist between these particles. When this occurs, the thermophysical properties of the nanofluid are altered by means of the diminishing of the Brownian motion of the particles, the amplification of the frictional resistance and the increase in pressure drop across the fluid [1].

Due to inconsistencies resulting from the altered thermophysical properties of the nanofluid, steady performance is no longer possible and the nanofluid as a whole is deemed unstable. Therefore, preparing a stable and durable nanofluid remains a prerequisite in terms of optimising its thermal properties [9].

2.4.1. Indication of stability

The stability of a nanofluid may be deemed a function of various parameters such as nanoparticle type, particle volume fraction, particle shape and size, type and concentration of surfactant, temperature and method of preparation [10].

As for investigating the stability of these fluids, a variety of techniques exist for ranking nanofluid stability. Some of the more commonly used techniques reported on in literature are identified and discussed as follows:

- Sediment photograph capturing: One of the simplest forms of deducing a nanofluid's stability is by means of visual inspection or sediment photograph capturing. This technique involves photographing samples of the nanofluid at fixed time intervals (hours, days, weeks, etc.) to allow for the visual observation of sediment formation and deposition of the suspended nanoparticles.

For samples of nanofluids with generally high stability, test times may be reduced by using a centrifuge. During the test, the sample is centrifuged at a known RPM and the time taken for sedimentation to begin is measured [11]. One example of this type of stability measurement is reported by Yu et al. [12].

- Zeta potential test: According to Ghodsinezhad et al. [8], nanoparticles have two distinct layers of ions that travel with them as they diffuse throughout the solution. Therefore, zeta potential refers to the electrical potential across the boundary of this double layer and is used to predict the colloidal stability of the fluid. The greater the absolute value of zeta potential, the greater the nanofluid stability.
  Table 2.2, adapted from Ghadimi et al. [9], serves as an indication of the relationship between zeta potential and nanofluid stability.

Table 2.2. Relationship between the stability of nanofluids and zeta potential

Zeta potential (mV)	Nanofluid stability
0	Very little or no stability
15	Little stability with settling
30	Moderate stability with sedimentation
45	Good stability with possible settling
60	Excellent stability, a little settling

Although a zeta potential test allows for a quantitative description of a suspension's stability, it is restricted when analysing fluids with high viscosities and/or low particle concentrations.

- UV-VIS spectrophotometry: Another technique for quantitatively studying the stability of nanofluids is ultraviolet visible (UV-VIS) spectrophotometry. This method entails that light in the UV and visible region is used in conjunction with a spectrophotometer to measure the difference in intensities of the incident and emergent light passing through the sample [11].
  Despite this technique applying to a wider range of fluids, more so than the zeta potential method, it is not suitable for solutions containing CNTs or those of very high particle concentrations because high concentrations result in darker solutions and thus make it difficult to reliably measure incident and emergent light intensities.

- Tracking of a measurable nanofluid parameter: Another form of indicating nanofluid stability or continuity is to track a measurable parameter of the fluid, such as thermal conductivity or viscosity, over a set time interval to show that no deviation occurred (showing continuity in the property as opposed to time).

Despite the various techniques, no single technique is capable of determining the stability of a nanofluid alone. Therefore, as highlighted by Sharifpur and Meyer [5], the different techniques must be used in conjunction with one another for the best possible indication of a fluid's stability.

2.4.2. Methods to enhance stability

Despite the difficulties associated with overcoming the strong intermolecular forces that exist in nanofluids and result in the development of agglomeration and sedimentation, some techniques may be used to reduce such occurrences and hence enhance overall fluid stability. These techniques may be broadly categorised as either chemical or physical treatment methods. The more commonly used techniques are discussed in detail in the following sections.

2.4.2.1. Chemical treatments

As highlighted by Ghadimi et al. [9], chemical treatment methods aim to change the surface properties of the suspended nanoparticles and to suppress the formation of particle clusters with the purpose of attaining stable suspensions. Of the various methods available, common reported on techniques include surfactant addition and pH adjustment.

Surfactant addition:

Surfactants or "dispersants" are complex chemical compounds that are both an easy and economical way to enhance the stability of a nanofluid. These compounds can affect the surface characteristics of a mixture and therefore are capable of lowering the interfacial tension between the base fluid and the suspended nanoparticles. The outcome of these effects is improved nanoparticle dispersibility (increased suspension time of nanoparticles in the base fluid) [12].

When a surfactant is used in a nanofluid, it is termed a dispersant. Dispersants generally consist of a hydrophobic tail portion (usually a long-chain hydrocarbon) and a hydrophilic polar head group. Depending on the desired application, dispersants may be used to convert nanoparticles from hydrophilic to hydrophobic and vice versa.

When classifying surfactants, the composition of the head is used. Based on this classification method, the following four possible classes of surfactants are available for use:

- non-ionic surfactants;
- anionic surfactants;
- cationic surfactants;
- amphoteric surfactants.

Table 2.3 presents these classes of surfactants, the composition of the head and some common examples of each surfactant class.

Table 2.3. Composition of surfactant head for different surfactant classes as well as examples of the classes

Surfactant class	Composition of surfactant head	Examples
Non-ionic	No charge group on surfactant head	Polyethylene oxide, alcohols and other polar groups
Anionic	Negatively charged head groups	Long-chain fatty acids, sulfosuccinates, alkyl sulphates, phosphates and sulfonates
Cationic	Positively charged head groups	Protonated long-chain amines and long-chain quaternary ammonium compounds
Amphoteric	Zwitterionic head groups, where charge depends on the pH of the surfactant	Betaines and certain lecithins

Despite their low cost and easy application, it should be noted that surfactants pose the risk of limiting the nanofluid's thermal conductivity by increasing the thermal resistance that exists between the nanoparticles and base fluid [12]. Furthermore, depending on exposed conditions, surfactant interactions with nanoparticles may deteriorate with time. Therefore, care and consideration should be taken when selecting a suitable surfactant [11].

pH adjustment:

The pH value at which a particular molecule carries no net electric charge or where hydration forces are negligible is termed the isoelectric point (IEP). When a nanofluid's pH value approaches or is equal to the IEP, zeta potential and the repulsive forces between the nanoparticles and the base fluid are zero and hence the

fluid becomes unstable [13]. To enhance the stability of nanofluids, one must ensure that the hydration forces between the nanoparticles are high [14].

The pH adjustment of nanofluids is conducted by means of acid treatment, which increases the hydrophilic properties of the nanoparticles [15]. Based on this increase, more hydroxyl groups are formed, leading to an increase in zeta potential and a more stable fluid [11].

The effects of pH on nanofluid stability have been observed by various researchers such as [16-18], where pH values for CNT/deionised (DI) water, Al_2O_3-water and Cu-water were found to be 10, 8.9 and 9.5 respectively. However, it should be noted that a stable nanofluid should have a pH value of approximately 7 due to the simple fact that an extremely low- or high-value pH may damage the heat transfer surface in which the fluid is to be used by means of corrosion (particularly at high-temperature ranges) [14].

2.4.2.2. Physical treatments

As stated before, the two-step preparation method is highly susceptible to particle agglomeration as a direct result of the strong intermolecular forces that exist between the different particles. Therefore, nanofluids prepared in this way require adequate treatment to ensure stable solutions.

In addition to making use of chemical treatments such as surfactant addition and pH adjustment, many researchers report using state-of-the-art equipment to physically break down the aggregation of particles using ultrasonic, magnetic and shear force [8, 9, 11]. Common examples of physical treatments include ultrasonic baths, homogenisers, magnetic stirrers and shear stirrers, where treatment varies based on the type and concentration of particles, the base fluid and whether or not other treatment techniques were used prior to the physical treatment.

In addition to the effects of various nanofluid components on the required treatment time to produce stable solutions, Ghodsinezhad et al. [8] report that treatment time, particularly for ultrasonication, also affects the thermophysical properties of the nanofluid.

2.4.3. Previous works reporting on stability

The following table was formulated on the review papers of [9, 13] and serves as an indicator of the various works where nanofluid stability has been reported. Regarding these works, it should be noted that Table 2.4 only contains a selected number of entries and that the works should be consulted for further examples.

Table 2.4 illustrates the appropriate works in terms of the researcher, the type of base fluid and nanoparticles considered, the stability process(es) used and lastly, the overall reported stability of the resulting fluid.

Table 2.4. Summary of previous works reporting on nanofluid stability processes and reported stability

Researcher	Base fluid	Nanoparticle	Stability process(es)	Reported stability
Oh et al. [19]	Distilled water	Al_2O_3	Ultrasonic cleaner for 15 hours	Sedimentation occurred minutes after preparation
Oh et al. [19]	EG	Al_2O_3	Ultrasonic cleaner for 15 hours	Sedimentation occurred minutes after preparation
Chiesa et al. [20]	Mineral oil	Al_2O_3	Ultrasonication (duration not specified)	For several days
Chiesa and Das [20]	Isoparaffinic polyalphaolefin	Al_2O_3	Ultrasonication (duration not specified)	For several days
Wang et al. [21]	Distilled water	Al_2O_3	Ultrasonication for 15 minutes, pH control and surfactant addition of SDBS	N/A
Witharana et al. [22]	EG	Al_2O_3	Ultrasonication (duration not specified)	More than 2 months

Witharana et al. [22]	Propylene glycol (PG)	Al_2O_3	Ultrasonication (duration not specified)	More than 2 months
Witharana et al. [22]	EG	ZnO	Ultrasonication (duration not specified)	More than 2 months
Das et al. [23]	Distilled water	Al_2O_3	Ultrasonication for 11 hours	More than 12 hours of stability
Witharana et al. [22]	Propylene glycol	ZnO	Ultrasonication (unknown duration)	More than 2 months
Chung et al. [24]	Ammonium poly	ZnO	Ultrasonic horn for 1 hour	Over 10 000 hours
Das et al. [23]	Distilled water	CuO	Ultrasonication for 11 hours	More than 12 hours of stability
Hwang et al. [25]	Distilled water	CuO	N/A	Stable
Hwang et al. [25]	EG	CuO	N/A	Stable
Song et al. [26]	Pure water	Stainless steel	SDS used as a surfactant	10 days
Song et al. [26]	Pure water	Stainless steel	CTAB used as a surfactant	10 days
Bandyopadhyaya et al. [27]	Pure water	SWNTs	GA used as a surfactant	Over a few months
Islam et al. [28]	Pure water	SWNTs	SDBS used as a surfactant in addition to ultrasonic bath for 16-24 hours	3 months
Wu et al. [29]	Pure water	SWNTs	Humic acid used as a surfactant	More than 10 days
Xie et al. [30]	Decene	TCNTs	Oleylamine used as a surfactant	2 months
Chen et al. [31]	EG	TNT	Ultrasonic bath for 48 hours	Over 2 months
Yu et al. [32]	Pure water	MWNTs	SDBS used as a surfactant in addition to ultrasonic horn for varying times	90 days
Wusiman et al. [33]	Distilled water	MWCNTs	SDS and SDBS used as a surfactant in addition to ultrasonic mixing for 20 minutes	Long-term stability
Kim et al. [34]	Pure water	CNTs	SDBS used as a surfactant	More than 1 day
Kim et al. [34]	Pure water	CNTs	CTAB used as a surfactant	More than 1 day
Yu et al. [35]	Kerosene	Fe_3O_4	Oleic acid used as surfactant followed by ultrasonic horn for 30 minutes	Reduced particle size and good stability

Through analysis of Table 2.4, it is evident that a significant degree of research has been done on producing stable nanofluids. In addition, the table also illustrates the wide variety of stability techniques that may be used in conjunction with one another and should thus be considered carefully when preparing all nanofluids in the current investigation.

2.5. Thermophysical properties of nanofluids

Despite the tremendous interest and research that has been conducted on nanofluids over the past 20 years, no complete and comprehensive theory has accurately predicted the thermophysical behaviour of nanofluids. Consequently, various models and relations have been formulated by researchers in an attempt to numerically model these fluids properties.

In this section, conventionally reported thermophysical properties, namely density, specific heat, thermal expansion coefficient, thermal conductivity and viscosity, as well as the multiple models developed for each, are discussed and compared.

2.5.1. Density

Cheremisinoff [36] and Pak and Cho [37] both used the principles of the mixing theory to formulate a theoretical model used for predicting the density of solid-liquid mixtures. The model is as follows:

$$\rho_{nf} = (1-\varphi)\rho_{bf} + \varphi\rho_{np} \tag{2.1}$$

where the volume concentration of the nanoparticles was approximated employing the following relation:

$$\varphi = \frac{\emptyset \cdot \rho_{bf}}{\emptyset \cdot \rho_{bf} + \rho_{np}(1-\emptyset)} \tag{2.2}$$

Many authors used the model to predict the density of different nanofluids; however, the experimental measurements of these densities were shown to be much lower than those predicted by the model. Possible deviations in these quantities may be because the effects of the nanolayer, existing between the nanoparticles and base fluid, have not been taken into consideration.

Sharifpur et al. [38] proposed a new model for approximating the density of a nanofluid, where the nanolayer and its effects on the nanofluid density were considered. In their model, shown by equation 2.3, the mass and volume of the nanoparticles and base fluid, as well as the nanolayer thickness and nanoparticle radius were all used in the approximation of the fluid density.

$$\rho_{nf} = \frac{m_{np} + m_{bf}}{V_{bf} + \dfrac{V_{np}\left(r_{np} + \delta_{nl}\right)^3}{r_{np}^3}} \tag{2.3}$$

where the nanolayer thickness, δ_{nl}, was expressed by the following relation:

$$\delta_{nl} = -0.0002833 r_{np}^2 + 0.0475 r_{np} - 0.1417 \tag{2.4}$$

Furthermore, based on the proposition of equation 2.3, a similar correlation was formulated for calculating the volume fraction of nanoparticles in a base fluid. This revised model was characterised as follows:

$$\varphi = \frac{V_{np}}{V_{nf}} = \frac{V_{np}}{V_{bf} + \dfrac{V_{np}\left(r_{np} + \delta_{nl}\right)^3}{r_{np}^3}} \tag{2.5}$$

2.5.2. Specific heat

Similar to their proposed correlation for approximating nanofluid density, Pak and Cho [37] also used mixing theory to approximate the specific heat of nanofluids. This proposed model or correlation was a volume fraction relation between the thermophysical properties of the base fluid and nanoparticles and was rendered as follows:

$$c_{p_{nf}} = (1-\varphi)c_{p_{bf}} + \varphi c_{p_{np}} \tag{2.6}$$

An alternative expression for nanofluid specific heat is proposed in the work of Balla et al. [39], where thermal equilibrium between the suspended nanoparticles and surrounding base fluid was assumed. The model was formulated as follows:

$$c_{p_{nf}} = \frac{\varphi c_{p_{np}} \rho_{np} + (1-\varphi) c_{p_{bf}} \rho_{bf}}{\rho_{nf}} \tag{2.7}$$

O'Hanley et al. [40] compared both models discussed above with experimental data obtained for the specific heats of different types of nanofluids. They investigated water-based nanofluids with particle concentrations ranging from 5 wt.% to 50 wt.%. Upon analysing the data, it was found that the predictions of the simple volume fraction model (equation 2.6) deviated significantly from the experimental data, whereas the predictions of the thermal equilibrium model (equation 2.7) were in excellent agreement with the test results. Based on these results, they recommended using the thermal equilibrium model for approximating the specific heat of nanofluids.

2.5.3. Thermal expansion coefficient

Regarding the principles of the mixing theory, the thermal expansion coefficient is another thermophysical property of nanofluids, typically approximated by such means.

Ghodsinezhad et al. [8] note that the volumetric thermal expansion coefficient is typically larger for base fluids than for solid nanoparticles and that this trait is directly proportional to temperature. The typical expression used to predict the property as defined by Pak and Cho [37] is as follows:

$$\beta_{nf} = \varphi \beta_{np} + (1-\varphi)\beta_{bf} \tag{2.8}$$

Contrary to the above model, Ho et al. [41] offer an alternative expression that, similar to Balla et al. [39], assumes thermal equilibrium between the base fluid and the suspended nanoparticles. The resulting model was expressed as follows:

$$\beta_{nf} = \frac{\varphi \beta_{np} \rho_{np} + (1-\varphi)\beta_{bf} \rho_{bf}}{\rho_{nf}} \tag{2.9}$$

In the work of Ho et al. [41], the volumetric expansion coefficient of Al_2O_3 particles in a base fluid of water was experimentally measured and compared with the predicted quantities of equations 2.8 and 2.9. Based on their observations, it was noted that equation 2.9, the thermal equilibrium model, produced a more accurate and reliable correlation between the experimental and theoretical data.

2.5.4. Thermal conductivity

The desired enhancement of the thermal properties of nanofluids is often discussed in terms of the enhancement within the base fluid's thermal conductivity. As a result, thermal conductivity is a key concept when analysing heat transfer in nanofluids and is deemed an important transport property in terms of the practical application of these fluids [42].

According to Aybar et al. [43], the enhancement of thermal conductivity is a result of four major mechanisms, namely Brownian motion of the nanoparticles, the nanolayer, clustering of the nanoparticles and the nature of heat transport in the nanoparticles. Each of these mechanisms are discussed in the following section.

2.5.4.1. Brownian motion

For general cases, where particle size is large, the effect of Brownian motion is neglected. However, when particles approach the nanoscale, Brownian motion and its effects on the surrounding fluid involve heat transfer and thus cannot be ignored.

Aybar et al. [43] state that the Brownian motion of nanoparticles may contribute to the enhancement of a fluid's thermal conductivity by means of the movement of the nanoparticles and the micro-convection of fluid around each individual particle. Of these different methods, theoretical analysis has shown the former to be negligible and the latter to produce minor effects [44, 45].

Das et al. [7] emphasise the importance of nanoparticle interaction between nanoparticles and liquid molecules in developing a model to predict nanofluid behaviour. Therefore, several models have been formulated to predict thermal conductivity, taking into account the effects of particle Brownian motion. Some of the models are presented in Table 2.5.

Table 2.5. Nanofluid thermal conductivity models accounting for effects of Brownian motion

Researcher	Model	Remarks
Xuan et al. [46]	$k_{nf} = k_{bf}\left(\frac{k_{np}+2k_{bf}-2\varphi(k_{bf}-k_{np})}{k_{np}+2k_{bf}+\varphi(k_{bf}-k_{np})} + \frac{\rho_{np}\varphi c_{p_{np}}}{2k_{bf}}\sqrt{\frac{K_B T}{3\pi\mu r_c}}\right)$	The model takes into account the Brownian motion, aggregation structure of nanoparticle clusters and includes the fluid temperature in its approximation. Not capable of predicting a linear increase of conductivity with temperature.
Jang et al. [47]	$k_{nf} = k_{bf}(1-\varphi_{eff}) + BK_{np}\varphi_{eff} + B_{pc}\frac{d_{bf}}{d_{np}}k_{bf}Re_{d_{np}}^2\varphi_{eff}$ where B is a constant for the Kapitza resistance per unit area, B_{pc} is a proportional constant and Re_{dp} is calculated as follows: $Re_{d_p} = \frac{\alpha d_{np}}{(l_m \cdot \mu)_{bf}}$ Note: l_m is the liquid mean path	The model contains four modes of energy transport: collisions of base fluid molecules, thermal diffusion in nanoparticle fluids, collisions between nanoparticles and thermal interaction of dynamic nanoparticles with the base fluid molecules.
Evans et al. [44]	$k_{nf} = k_{bf}\left(1 + 3\varphi\frac{\gamma-1}{\gamma+2}\right)$ where γ is the ratio between the particle radius and the equivalent matrix thickness.	Considers a homogeneous situation where all volumes of the fluids diffuse together with the nanoparticles. Assumes particles are well dispersed in the base fluid. The model shows that the ratio of the thermal conductivity contribution caused by Brownian motion with respect to the thermal conductivity of the base fluid is proportional to the thermal diffusivity of the nanoparticle and the base fluid.

2.5.4.2. Nanolayer

Nanolayer is the expression or term used to define the solid-like, liquid layers at the interface of the base fluid and nanoparticles in a nanofluid. Although very little is known about the thermal properties of this particular layer, it is believed that it acts as a thermal bridge between a solid nanoparticle and a base fluid and thus is critical to enhancing thermal conductivity [48].

Table 2.6 summaries a few of the different models developed that relate nanofluid conductivity to the "solid-like" nanolayer.

Table 2.6. Nanofluid thermal conductivity models accounting for effects of nanolayer

Researcher	Model	Remarks
Yu and Choi [48]	$k_{nf} = \left[\frac{k_{np}+2k_{bf}+2(k_{np}-k_{bf})\left(1+\frac{\delta_{nl}}{r_{np}}\right)^3\varphi}{k_{np}+2k_{bf}-(k_{np}-k_{bf})\left(1+\frac{\delta_{nl}}{r_{np}}\right)^3\varphi}\right]k_{bf}$	A renovated Maxwell model to take into account the effects of the nanolayer. Assumes that the nanolayer around each particle may be combined with

		the particle to form an equivalent particle. Limited to suspensions with spherical particles.
Yu et al. [49]	$k_{nf} = \left[1 + \frac{D_{esf}\cdot\varphi_e\left(\frac{1}{3}\sum_{j=a,b,c}\frac{k_{pj}-k_{bf}}{k_{pj}+(D_{esf}-1)k_{bf}}\right)}{1-\varphi_e\left(\frac{1}{3}\sum_{j=a,b,c}\frac{k_{pj}-k_{bf}}{k_{pj}+(D_{esf}-1)k_{bf}}\right)}\right]k_{bf}$ where the empirical shape factor, D_{esf}, is defined as: $D_{esf} = 3\psi^{-\psi}$ and k_{pj}, the equivalent thermal conductivities along the axes of the complex ellipsoid where *j=a, b, and c*. Furthermore, the equivalent volume concentration for complex ellipsoids is defined as follows: $\varphi_e = V_r\varphi$ where V_r is the volumetric ratio.	Extension of the Hamilton-Crosser model suspensions of nanospherical particles to include the effect of the nanolayer. The model is capable of predicting the thermal conductivity of nanofluids containing CNTs in a base fluid of oil.
Zhou et al. [50]	$k_{nf} = k_{bf}\left[1 + \frac{3\varphi_t b\left(\frac{P_L+2P_T}{3P_0}\right)}{1-\varphi_t b\left(\frac{P_L+2P_T}{3P_0}\right)}\right]$ where b is a dipole factor defined as follows: $b = \frac{[\bar{k}(r_{np}+\delta_{nl})-k_{bf}]}{[\bar{k}(r_{np}+\delta_{nl})+2k_{bf}]}$ $\boldsymbol{P}_0, \boldsymbol{P}_L$ and $\boldsymbol{P}_T$ are the dipole moments of sphere, sphere longitudinal field and sphere transverse field respectively and φ_t is the total volume fraction of the coated particles and is expresses as follows: $\varphi_t = \varphi_o\left(1 + \frac{\delta_{nl}}{r_{np}}\right)^3$	Models the effect of interfacial nanolayers and the mutual interaction of nearest neighbouring inclusions on the effective thermal conductivity of nanofluids. The model accounts for the effects of volume fraction, particle radius and nanoshell thickness.

2.5.4.3. Nanoparticle clustering

Initial sections of the current literature review focus on the potential preparation methods of nanofluids, as well as the various parameters influencing their stability and continuity. In terms of the two-step method, it is stated that nanoparticles are produced separately and then dispersed in the base fluid. Therefore, to ensure a homogeneous solution and minimise the potential for particle agglomeration, many different treatment techniques, discussed in Section 2.4.2, are used. The relationship of thermal conductivity and particle clustering in nanofluids is reported in several publications.

Wang et al. [51] state that nanoparticle clusters act like local percolation (filter) structures and therefore contribute positively to the enhancement of effective thermal conductivity. Similarly, Prasher et al. [52] report on the enhancement of thermal conductivity under the presence of particle clusters; however, they justify this statement through the use of the effective medium theory and the explanation of aggregation kinetics.

Contrary to the previous works, Karthikeyan et al. [53] observed the opposite effects on thermal conductivity when particle clustering was present. They explain that nanoclusters are more likely to settle in the base fluid as a result of their larger mass. Due to the resulting particle gradient in the fluid, large regions of "particle-free" zones, which have high thermal resistance, are formed and therefore result in reduced thermal conductivity of the fluid.

Other notable works relating to nanoparticle clustering and thermal conductivity enhancement include those of [54-56].

2.5.4.4. Hybrid models and other effects

In addition to the different mechanisms responsible for the enhancement of thermal conductivity, Aybar et al. [43] identify important factors to take into consideration when accurately modelling the thermal conductivity of nanofluids. These factors include the following:

- temperature;
- pH;
- dispersion;
- size and shape of nanoparticles;
- nanoparticle settling time.

Although there is still no single model that takes into account all these parameters, some investigators have made progress in proposing models that consider some of these effects. Such models are generally deemed "hybrid models". Table 2.7 summarises a selected number of the models identified in the review of Aybar et al. [43].

Table 2.7. Examples of hybrid models for predicting nanofluid thermal conductivity

Researcher	Model	Remarks
Avsec [57]	$k_{nf} = k_{bf}\left[\frac{k_{np}+\left(\frac{3}{\psi}-1\right)k_{bf}-\left(\frac{3}{\psi}-1\right)\varphi_{eff}\left(k_{bf}-k_{np}\right)}{k_{np}+\left(\frac{3}{\psi}-1\right)k_{bf}+\varphi_{eff}\left(k_{bf}-k_{np}\right)}\right] \times \left(1 + C_{ft}Re^{O_{co}}Pr^{S_{co}}\right)$ where C_{ft}, O_{co} and s_{co} are constants and the effective particle volume, φ_{eff}, is defined as follows: $\varphi_{eff} = \varphi\left(1+\frac{\delta_{nl}}{r_{np}}\right)^3$	A combined model based on statistical Nano mechanics, which accounts for the influence of both Brownian motion and the formation of the nanolayer.
Corcione [58]	$k_{nf} = k_{bf}[1 + 4.4Re_{d_{np}}^{0.4}Pr^{0.66}\varphi_{np}^{0.66}\left(\frac{T}{T_{fp}}\right)^{10}\left(\frac{k_{np}}{k_{bf}}\right)^{0.03}$ where the Reynolds number, $Re_{d_{np}}$, is expressed as: $Re_{d_{np}} = \frac{2\rho_{bf}K_BT}{\pi\mu_{bf}^2 d_{np}}$	Empirical relation, based on experimental data of literature, with a 1.86% standard deviation of error. Model accounts for influence of particle volume fraction, temperature and nanoparticle diameter.
Kumar et al. [59]	$k_{nf} = k_{bf}\left(1 + A\bar{u}_{np}\frac{\varphi r_{bf}}{k_{bf}(1-\varphi)r_{np}}\right)$ where the average particle velocity, $\bar{u}_{np}$, is defined as follows: $\bar{u}_{np} = \sqrt{\frac{2K_BT}{\pi\mu d_{np}^2}}2$	Hybrid model to account for enhancement based on the stationary particle model and moving particle model. Modelled by drawing a parallel to the kinetic theory of gas and accounts for the dependence of thermal conductivity on particle size, volume fraction and temperature.

2.5.4.5. Traditional models

As may be perceived from these mechanisms and their associated models used for predicting thermal conductivity, a significant degree of research has been conducted in an attempt to accurately model this particular thermophysical characteristic. However, regardless of the diverse models available, there is still no single and complete model accounting for all possible mechanisms and factors that influence the enhancement of thermal conductivity. Therefore, many experimental investigators prefer to make use of traditional models when validating and correlating their results [60].

Table 2.8 provides a summary of the more common, traditional models that are often reported by various nanofluidic specialists and researchers.

Table 2.8. Traditional models used for predicting nanofluid thermal conductivity

Researcher	Model	Remarks
Maxwell [2]	$k_{nf} = k_{bf}\left[1 + \frac{3\left(\frac{k_{np}}{k_{bf}}-1\right)\varphi}{\left(\frac{k_{np}}{k_{bf}}+2\right)-\left(\frac{k_{np}}{k_{bf}}-1\right)\varphi}\right]$	Used for statistically homogeneous and volume fraction suspensions, where nanoparticles are non-interacting uniform-sized spherical particles that are randomly distributed in the base fluid.
Hamilton et al. [61]	$k_{nf} = k_{bf}\left[\frac{k_{np}+(E_{esf}-1)k_{bf}+(E_{esf}-1)(k_{np}-k_{bf})\varphi}{k_{np}+(E_{esf}-1)k_{bf}-\varphi(k_{np}-k_{bf})}\right]$	Adaption of [2] where shape factor, E_{esf}, is introduced. $E_{esf} = 3/\psi$, where ψ is the nanoparticle sphericity, which is defined as the surface area of a sphere, which has the same volume as a single nanoparticle to the surface area of the nanoparticle. E_{esf} is equivalent to 3 and 6 for spherical and cylindrical particles respectively.
Wasp et al. [62]	$k_{nf} = k_{bf}\left[\frac{k_{np}+2k_{bf}-2\varphi(k_{bf}-k_{np})}{k_{np}+2k_{bf}+\varphi(k_{bf}-k_{np})}\right]$	An alternate expression or special case for [61] where particle sphericity is equal to 1.
Bruggeman [63]	$k_{nf} = \frac{1}{4}\left[(3\varphi-1)k_{np} + (2-3\varphi)k_{bf}\right] + \frac{k_{bf}}{4}\sqrt{\Delta}$ where: $\Delta = \left[(3\varphi-1)^2\left(\frac{k_{np}}{k_{bf}}\right)^2 + (2-3\varphi)^2 + 2(2+9\varphi-9\varphi^2)\left(\frac{k_{np}}{k_{bf}}\right)\right]$	Reported to be the most accurate model for predicting the thermal conductivity of suspensions with spherical particles, Suresh et al. [42]

When comparing the quantities obtained through the traditional models with those of experimental values, it is reported that these models tend to underpredict the true thermal conductivity of nanofluids. Because these models were formulated before the age of nanofluids, they do not account for all parameters influencing thermal conductivity enhancement and therefore such an underprediction is expected [42].

2.5.5. Viscosity

The viscosity of a fluid is an indicator of its ability to resist flow and is scientifically defined as the ratio of the fluid's shear stress to shear rate. According to Meyer et al. [10], the viscosity of a fluid is of paramount importance when considering the industrial application and thermal efficiency of nanofluids, because the advantageous enhancement of thermal conductivity, achieved by nanoparticle addition, may be undermined by the accompanying increase in fluid viscosity. This increase is especially applicable to applications that involve flow, because pumping power requirements and flow properties, such as the Reynolds numbers, heat transfer coefficients and pressure drops, are heavily dependent on fluid viscosity.

According to reviews by Meyer et al. [10] and Kumar et al. [64], approximating the viscosity of nanofluids may be done by a number of different formulas classified as either classical theoretical models, models based on these classical models, new theoretical models and empirical models. Based on their research and reviews, these models are discussed in the following sections.

2.5.5.1. *Classical theoretical models*

According to Ottermann [65], these models were developed prior to the invention of nanofluids and thus are restricted in their applications to the modern field of nanotechnology and nanofluids as a whole. Table 2.9 summarises the classical models discussed by [10, 64].

Table 2.9. Summary of classical theoretical models for predicting nanofluid viscosity

Researcher	Model	Remarks
Einstein [66]	$\mu_{nf} = \mu_{bf}(1 + 2.5\varphi)$	Linear model established for fluids containing spherical particles with low volume fractions of $\varphi \leq 2\%$ Assumed that no interaction between particles occurs.
Krieger et al. [67]	$\mu_{nf} = \mu_{bf}\left[1 - \frac{\varphi}{\varphi_{max}}\right]^{-\eta\varphi_{max}}$	A semi-empirical model for shear viscosity, which is based on randomly mono-dispersed particles of hard spherical shape. Valid for virtually the whole spectrum of nanoparticles. φ_{max} is the maximum concentration at which flow can occur (value of 0.605 for high shear rate) and the intrinsic viscosity, η, is typically 2.5 for spherical particles.
Nielsen [68]	$\mu_{nf} = \mu_{bf}(1 - \varphi)e^{\frac{\varphi}{1-\varphi}}$	Power-law model developed for predicting the viscosity of fluids containing a volume fraction greater than 2%.
Batchelor [69]	$\mu_{nf} = \mu_{bf}(1 + 2.5\varphi + 6.2\varphi^2)$	Modification of Einstein's viscosity equation by introducing the effects of Brownian motion (particle interaction). Model developed by considering isotropic suspensions of rigid and spherical nanoparticles. Model approaches that of Einstein for very low particle volume concentrations.

2.5.5.2. *Models based on classical theoretical models*

The models presented in Table 2.10, although deemed classical models were developed based on or modified from the previous models in Table 2.9.

Table 2.10. Summary of models developed from classical theoretical models for predicting nanofluid viscosity

Researcher	Model	Remarks
Brinkman [70]	$\mu_{nf} = \mu_{bf}(1 - \varphi)^{-2.5}$	An extension of Einstein's model. Suitable for a volume fraction of $\varphi \leq 4\%$.
Lundgren [71]	$\mu_{nf} = \mu_{bf}\left(1 + 2.5\varphi + \frac{25}{4}\varphi^2 + f(\varphi^3)\right)$	Taylor series expansion of φ and is referred to as the reduction of Einstein's model.
Taylor [72]	$\mu_{nf} = \mu_{bf}\left[1 + 2.5\varphi\left(\frac{\mu' + \frac{2}{3}\mu_{bf}}{\mu' + \mu_{bf}}\right)\right]$ where μ' is the viscosity of the liquid droplet.	An extension of Einstein's model for liquid containing drops of another liquid in suspension. Assumed that liquid drops are spherical. Surface tension must be high to retain sphericity and thus this model is only valid for such a condition.
Mooney [73]	$\mu_{nf} = \mu_{bf}\exp\left(\frac{2.5\varphi}{1-\upsilon\varphi}\right)$	Based on similar logic to Einstein's model and is similarly limited to spherical particles. Semi-empirical model as the interaction data, υ, was left to be found via empirical means (υ represents the crowding factor and will be different for particle suspensions consisting of two different diameters).

Frankel et al. [74]	$\mu_{nf} = \frac{9}{8}\mu_{bf}\left(\frac{\left(\frac{\varphi}{\varphi_{max}}\right)^{\frac{1}{3}}}{1-\left(\frac{\varphi}{\varphi_{max}}\right)^{\frac{1}{3}}}\right)$	Developed using the asymptotic technique to describe the viscosity of the suspension within the concentrated limit where maximum volume fraction is obtainable. Model assumes uniform solid spheres and is a complement of Einstein's model from the diluted to the concentrated regime.
Graham [75]	$\mu_{nf} = \mu_{bf}\left(1 + 2.5\varphi + 4.5\left[\frac{1}{\left(\frac{h_s}{dnp}\left(2+\frac{h_s}{dnp}\right)\right)\left(1+\left(\frac{h_s}{dnp}\right)^2\right)}\right]\right)$ where h_s is the minimum separation distance between two spheres	Similar to both Einstein and [74] when the lower and upper solid volume fraction limit tends to zero and infinity respectively. Based on spherical particles with constant diameter and equidistance apart from one another. Assumed zero inertial, Brownian motion, Van der Waals and electroviscous forces.

2.5.5.3. New theoretical models

Despite the significant number of classical models available, the majority of researchers have had little success when using the models to accurately predict the viscosity of a nanofluid. A simple explanation for this result may be that the classical models were developed before the development of nanofluid technology. Therefore, most classical models have been formulated around particle concentration and hence many critical parameters affecting nanofluid viscosity have been neglected. Such parameters include nanolayer, capping layer, temperature, particle shape, volume concentration, interparticle spacing and pH [5, 10]. Some of the more significant modern or "new theoretical" models are presented in Table 2.11.

Table 2.11. Summary of new and significant theoretical models

Researcher	Model	Remarks
Haisheng et al. [76]	$\mu_{nf} = \mu_{bf}\left(1 - \frac{\varphi_a}{\varphi_m}\right)^{-[\eta]\varphi_m}$ where $\varphi_a = \varphi\left(\frac{r_a}{r_p}\right)^{3-D}$, where D is the fractal index and r_a and r_p are the radii of the agglomerates and primary particles respectively.	Similar to [67] and taking into consideration the effects of particle agglomeration on fluid viscosity (agglomeration results in larger particles forming). Model acknowledges that particle size affects the composition of the fluid and hence its thermophysical properties.
Masoumi et al. [77]	$\mu_{nf} = \mu_{bf} + \frac{\rho_{np}V_B d_{np}^2}{72C_1\delta}$	Model based on Brownian motion and takes into account the five parameters of volumetric fraction, temperature, particle diameter, particle density and the base fluid's physical properties. Shows acceptable agreement with experimental data for models with nanofluids with single and two-base fluids.
Masoud Hosseini et al. [78]	$\mu_{nf} = \mu_{bf}\exp\left[m + \alpha\left(\frac{T}{T_0}\right) + \omega(\varphi_h) + \gamma\left(\frac{d_{np}}{1+r}\right)\right.$ where the empirical constants, α, ω and γ, are obtained via experimental means.	Dimensionless model taking into account the viscosity of the base fluid, the hydrodynamic volume fraction of nanoparticles (φ_h), the diameter of nanoparticles (d_{np}), the thickness of the capping layer (r) and temperature.

2.5.5.4. Empirical models

The final classification of models used in predicting nanofluid viscosity is that of empirical models. Graf [79] recommends that experimental results should be presented in such a manner to allow for easy and effective comparison with the various theoretical models. Equation 2.10 illustrates the suggested exponential model in which experimental results are to be expressed and which is valid for particle volume concentrations of up to 35%.

$$\mu_{nf} = \mu_{bf}(1 + [\eta]\varphi + [\eta]^2\varphi^2 + [\eta^3]\varphi^3 + [\eta^4]\varphi^4 + \cdots) \tag{2.10}$$

In addition to representing experimental results in a general form, Graf [79] also states that the intrinsic viscosity may be obtained experimentally because there is difficulty in approximating its value for a power of 3 and above by means of theoretical procedures.

Based on Avsec [57], the above expression was further modified to take into account the nanolayer interaction effect. The resulting model or "Renewed Ward model", as referred to by Ghadimi et al. [9], was expressed as follows:

$$\mu_{nf} = \mu_{bf}\left(1 + [\eta]\varphi_{eff} + [\eta]^2\varphi_{eff}^2 + [\eta^3]\varphi_{eff}^3 + [\eta^4]\varphi_{eff}^4 + \cdots\right) \tag{2.11}$$

where the effective volume concentration, referred to in Table 2.7, was expressed as follows:

$$\varphi_{eff} = \varphi\left(1 + \frac{\delta_{nl}}{r_{np}}\right)^3 \tag{2.12}$$

where δ_{nl} and r_{np} are the nanolayer thickness and particle radius respectively.

To date, many empirical models have been developed for specific nanofluids under certain experimental conditions. However, despite all these correlations available for predicting the viscosity of nanofluids, Sharifpur et al. [5] emphasise the fact that no single hybrid model has yet been developed which takes into consideration all the different parameters influencing nanofluid viscosity. As a result, the existing correlations or models are still limited in their accuracy and require further research and development in order to produce a model that is both accurate, reliable and capable of predicting the viscosity of a nanofluid in real-life industrial applications (a model that will accurately operate outside experimental conditions).

2.6. Jet impingement heat transfer

Impinging jets are liquid or gaseous flows that are directed towards a surface or rigid wall [80]. When a fluid impinges onto a surface, the resulting boundary layer is reduced in thickness and therefore offers little resistance to heat and/or mass transfer rates [81]. The result of this behaviour is enhanced degrees of heat transfer when compared with wall-parallel flows.

Due to the "impressive" heat transfer capabilities and associated advantages, various industrial applications have begun to adopt jet impingement into their heating and cooling operations. Some common examples of areas where this technology is used are the textile and paper industry, gas turbine cooling processes and, as expected, electronic component cooling due to the substantial compactness of the technology [80].

The following section focuses on exploring the various types and configurations available, as well as the different parameters involved in the physics and behaviour of jet impingement heat transfer. Furthermore, a brief overview is given of the conventional procedures associated with experimental jet impingement for both steady- and transient state investigations. Lastly, relevant experimental works reporting on nanofluid jet impingement both within the steady- and transient state are summarised and included in appropriate tables.

2.6.1. Jet classification and geometry

To specify the characteristics of jet impingement, single jets are generally differentiated by the medium in which they exude, the level of confinement allocated to their dischargement path and their nozzle shape or geometry. A jet that exudes into a medium of equivalent density is termed a submerged jet, whereas a jet of alternative composition to that of the ambient, is classified as a free-surface jet. Depending on the presence of confinement structures directly obstructing the radial spread of the jet, jets may further be categorised as confined or unconfined jets. With respect to the available nozzle shapes often used in jet impingement applications, jets are generally distinguished as being circular or planar slot jets.

2.6.1.1. Submerged and free-surface jets

Submerged jets, as previously stated, are those where a fluid jet is expelled into a region containing the same fluid at rest. In submerged configurations, velocity gradients within the jet create shearing at the edges which, in turn, transfer momentum outwards. Such an interaction between the jet and stagnant fluid results in the development of a potential core near the jet centre line [82], which, according to Webb et al. [83], is defined as the region where the jet velocity remains largely unaffected by the spreading of the jet due to entrainment. In terms of the stagnation or impingement region, the axial velocity of the jet strongly decelerates, while the velocity in the wall tangential direction increases. This region, recognised for its high normal and shear stresses, plays an important role in influencing the local transport properties [80]. As for the region following deflection or impingement, submerged jets tend to continuously decelerate, while their jet thickness and resulting boundary layer increase. Due to this behaviour, the convective heat transfer in the flow direction of the wall jet typically decreases [80].

Contrary to the above jet classification, free-surface jets tend to display different characteristics. Free-surface jets undergo relaxation once exiting the jet nozzle as a direct result of the lack of shearing between the fluid jet and the low-density ambient medium or fluid [80]. As a result of this occurrence, entrainment of the surrounding fluid may also be seen as negligible and thus the potential core may be ignored [82]. Additionally, an increased mass flow of the descending jet is also neglected, and the velocity profile develops into a constant velocity. After impingement, the corresponding boundary layer of the free-surface jet at the wall originates from the jet centre and continuously increases in the direction of the flow until its thickness matches that of the jet height [80].

Figure 2.2 graphically illustrates the contrasting flow regions originating from submerged and free-surface jets.

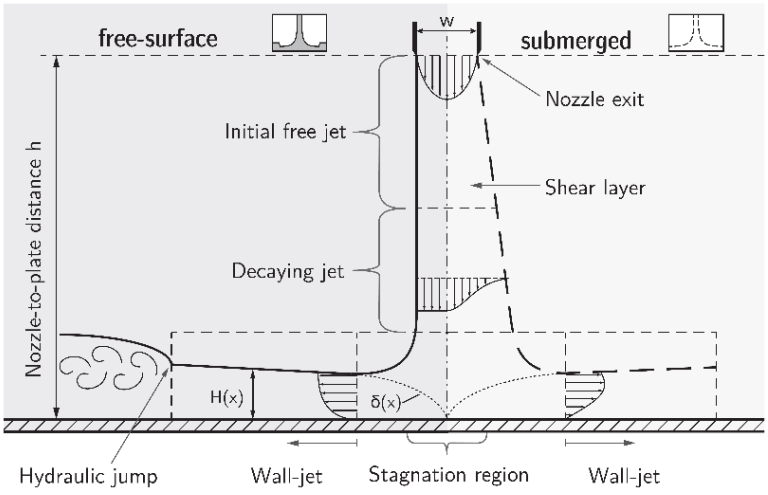

Figure 2.2. Distinct flow regions of an impinging jet field for submerged and free-surface jets adapted from Bieber et al. [80]

2.6.1.2. Confined and unconfined jets

An impinging jet is under confined conditions if the radial spread is confined within a narrow channel, usually between the impingement surface and the orifice plate [84]. In this particular configuration, the fluid exiting the jet is limited in its expansion, once impinging upon the target surface, and in some cases may get recirculated. As a result, the fluid becomes entrained back into the impinging jet [82]. Despite the reported lower heat transfer coefficients associated with this jet configuration, many industrial applications, especially those in electronic cooling, often require the jet to be confined by a solid boundary at the level of the nozzle exit [85].

Based on this description, it is clear that an unconfined jet is one where no constraints are instilled above the impinging surface and hence the jet fluid is free to expand once deflecting upon the target surface. As a result of this expansion freedom, no recirculation or entrainment of the jet occurs.

When considering the suitability of the available confinement options, both have their own merits and difficulties in terms of heat transfer application. According to Choo et al. [86], confined jets offer the advantage of a more compact design, while unconfined jets prove simpler in design and thus are easier to fabricate. The same paper also reports that the thermal performance of the two confinement options is similar when under fixed pumping power; however, confined jets perform 20 to 30% lower when exposed to a fixed flow rate condition.

Zuckerman et al. [87] report that confined jets produce lower average Nusselt numbers when compared with unconfined jets of the same experimental set-up. Behnia et al. [85] report that confined jets also tend to have decreased average heat transfer rates; however, they emphasise that there are no noticeable effects on the stagnation heat transfer coefficient. Contrary to the previous statement, Glynn et al. [84], report on the decrease of heat transfer coefficients due to confinement of impinging jets and associate such a decrease with the recirculation of fluid heated by the target surface.

2.6.1.3. Nozzle geometry

In their review of jet impingement heat transfer and physics, Zuckerman and Lior [87] refer to the strong influence of nozzle geometry on the resulting turbulence effects, and ultimately on the heat and mass transfer of the system.

Possibly the most common form of geometry used in jet impingement set-ups is the circular jet, which is obtained by means of a straight, circular tube with a circular nozzle exit [88]. Assuming that the nozzle is pipe-shaped, the exit velocity of the fluid will match a parabolic profile, which is common for general pipe flow. As a result, the dimensionless heat transfer profile along the impinging wall will be represented by high values within the zone of impingement [80].

Slot or "planar jets" are defined as long, thin jets with a two-dimensional velocity profile [89]. The general trends associated with these jets are mostly very similar to those of circular jets, except for significant quantitative differences [90]. According to Chen et al. [91], slot jets provide higher cooling effectiveness, better controllability, uniformity and thus may be viewed as superior to circular jets. Additionally, slot jets are capable of providing efficient cooling for applications with decreasing component dimensions but continuously increasing heat fluxes (such as compact electronic packages). Although it may be argued that slot jets possess many benefits over circular jets, Zuckerman and Lior [87] do, however, report on the many structural disadvantages that are characteristic of such a jet geometry.

2.6.1.4. Alternative configurations

Conventional jet impingement heat transfer applications use a single jet of chosen configuration and geometry, discussed above, to cool or heat a target surface that is traditionally a flat plate. However, "creative designers", as they are referred to by Zuckerman and Lior [87], tried to modify these traditional designs in an attempt to obtain higher heat transfer coefficients. These modified designs aim to improve the heat transfer performance of the system at an acceptable pressure drop and energy consumption and are constrained by strength, space and cost considerations.

Some of the possible variations and modifications of traditional jet impingement designs, presented in the review by Zuckerman and Lior [87], are discussed in the following sections:

<u>Induced swirl flow:</u>

In addition to deviating from the use of common nozzle geometries, discussed previously, some investigators modified their nozzles to structure swirl into the flow before allowing it to make contact with the impingement surface. As a result of the introduced swirl, flow speeds were rapidly increased while maintaining the nozzle mass flow rate [92].

According to Hee et al. [93], flow swirl may assist in producing more uniform Nusselt number distributions along the target surface; however, it comes at the cost of lower peak values. Additionally, these benefits are only obtained at low nozzle-to-target surface distances. Nozaki et al. [94] state that jet swirl may result in decreased stagnation zone heat transfer due to the formation of recirculatory regions directly under the swirling jet.

<u>Jet impingement angle:</u>

A common variation in jet design is to impinge the fluid at a particular angle rather than normal to the target surface. This angle of impingement may be required due to some unique feature of the hardware design or may be motivated by the need to reduce particular jet losses or interactions [87]. According to Tawfek [95],

the jet inclination is reported to generate elliptical isoclines of the Nusselt number and therefore distorts the overall heat transfer contours across the impingement surface. They note that Nusselt numbers tend to decrease as the impingement incidence angle becomes smaller than 90°.

Pulsed or unsteady jets:

Most of the investigations relating to jet impingement heat transfer were conducted under steady-state conditions, i.e. where flow characteristics and boundary conditions were fixed with time. However, despite the prevalence of such investigations, some researchers have modified their investigations to account for unsteady flow and boundary conditions. For example, in the work of Göppert et al. [96], a pulsed jet was used in conjunction with a flat target plate to investigate the influence of an unstable jet on the overall heat transfer of the system. They concluded that the tendency for the jet to mix with the surrounding fluid was increased and thus resulted in a loss of energy and speed at which the jet could reach the target surface. The Nusselt numbers across the plate were also found to decrease by up to 50% in comparison with a jet under steady-state conditions.

Jet arrays:

The use of multiple jet nozzles over an impingement surface has been found to offer improvements in the efficiency and uniformity of transfer properties for slot and circular jet nozzles. However, when more than one nozzle is used in an impingement set-up, a new phenomenon, known as jet interaction, must be considered. In jet arrays, adjacent jets interact with one another and result in new flow regions, termed fountain regions. Depending on jet-to-jet spacings, jet-to-target surface distances and the level of confinement on the system, jet arrays may either produce beneficial or detrimental effects.

Table 2.12 summarises the various jet height and spacing effects on jet array impingement.

Table 2.12. Summary of jet height and spacing effects on jet array impingement adapted from Zuckerman and Lior [87]

H/D	Effect on jet array impingement
<0.25	Highly constrained flow may have strong cross flow and additional back pressure. Additional flow acceleration expected to shift peak Nusselt number laterally by 0.5-1.5D.
0.25-1.0	Fountain flow may greatly affect heat transfer in confined array.
1-2	Mild fountain effects may occur. The flow will be influenced by the confinement wall.
2-8	Shear layers may interact with one another. Important to maintain sufficient jet pressure. The best performance of jet arrays tends to lie in this range.
8-12	Minimal confinement effects. Need to ensure that neighbouring jets remain separate.
>12	The confinement wall does not influence flow. Nozzle type and jet spacing are dominant in the flow field. Nusselt number is affected by energy losses of the jet approaching the wall. Need to ensure that neighbouring jets remain separate.

Alternative target surface geometry and configuration:

In addition to adapting the jet type, angle and geometry, as well as the number of impinging jets used in the system, modifications to the impingement and target surface may also be made. Therefore, despite the works reporting impingement upon flat target surfaces, many works exist where surface geometry has been varied or modified to enhance heat transfer performance.

For example, in the research of Gau et al. [97], surface curvature effects were studied, where concave and convex targets were cooled by employing jet impingement. Similarly, Fleischer et al. [98] studied curvature

effects on jet-impingement cooling; however, they used a cylindrical target. Gau et al. [99] experimentally studied the impingement of rib-roughened walls in an attempt to obtain larger degrees of heat transfer.

2.6.2. Non-dimensional parameters

The non-dimensional parameters that are typically associated with jet impingement heat transfer are defined and discussed in the following sections.

2.6.2.1. Reynolds number

The Reynolds number, named after Osborne Reynolds, is an important non-dimensional parameter that is used to differentiate whether or not a fluid flowing past a body or in a duct is steady or transient. As emphasised by Everts [100], it serves as the ratio of the inertia ($\rho U^2/D$) to viscous ($\mu U/D^2$) forces and is portrayed as follows:

$$Re = \frac{\rho \cdot U \cdot L_c}{\mu} = \frac{UL_c}{\upsilon} \tag{2.13}$$

where the characteristic length, L_c, may either be replaced by the nozzle diameter (D) for circular jets or the hydraulic diameter, D_h, for other geometries.

In classifying jet flow, the following ranges of Reynolds numbers are considered:

- dissipated laminar flow if Re<300;
- fully developed laminar flow if 300<Re<1 000;
- transitional flow if 1 000<Re<3 000;
- fully developed turbulent flow if Re>3 000.

2.6.2.2. Prandtl number

According to Cengel et al. [101], in convective heat transfer, the dimensionless Prandtl number is used to express the relative magnitudes of momentum and heat diffusion in the velocity and thermal boundary layers. Named after the German physicist Ludwig Prandtl, the parameter is defined as follows:

$$Pr = \frac{\upsilon}{\alpha} \tag{2.14}$$

2.6.2.3. Schmidt number

Similar to the Prandtl number, the Schmidt number is the corresponding quantity when considering mass convection and is expressed as follows:

$$Sc = \frac{\upsilon}{D_{AB}} \tag{2.15}$$

As indicated by the above expression, the Schmidt number is therefore the relative magnitude of molecular momentum and mass diffusion in the velocity and concentration boundary layers respectively [101].

2.6.2.4. Nusselt number

The Nusselt number is a dimensionless heat transfer coefficient that represents the ratio of convective heat transfer to that of conduction [100]. Depending on the flow regime, the Nusselt number can be represented by various correlations or functions consisting of other non-dimensional parameters; however, a more general expression is as follows:

$$Nu = \frac{h_{conv} L_c}{k} \tag{2.16}$$

where the convective heat transfer coefficient, h_{conv}, is defined as:

$$h_{conv} = \frac{-k\left[\frac{\partial T}{\vec{n}}\right]}{T_j - T_w} \tag{2.17}$$

and $k\partial T/\vec{n}$ provides the temperature gradient component normal to the wall.

2.6.2.5. Sherwood number

The corresponding quantity in mass convection is the dimensionless Sherwood number. Named after Thomas Sherwood, this is the non-dimensional property used to indicate the effectiveness of mass convection and is, essentially, the ratio of convective mass transfer to the rate of diffusive mass transport [101]. The parameter is defined as follows:

$$Sh = \frac{h_{mass} L_c}{D_{AB}} \tag{2.18}$$

where the mass transfer coefficient, h_{mass}, is defined as follows:

$$h_{mass} = \frac{-D_{AB}\left[\frac{\partial C}{\partial \vec{n}}\right]}{C_j - C_w} \tag{2.19}$$

and $\partial C/\vec{n}$ provides the mass concentration gradient component normal to the wall.

2.6.2.6. Recovery factor and impingement cooling or heating effectiveness

In addition to the above parameters, Zuckerman and Lior [87] and Carlomagno and Ianiro [89] refer to the non-dimensional recovery factor which describes the amount of kinetic energy transferred into and retained in thermal form as the jet slows down. It is expressed as follows:

$$R_f = \frac{T_r - T_j}{T_o - T_j} = \frac{T_r - T_j}{U_j^2/2c_p} \tag{2.20}$$

where T_r is termed the "recovery temperature", which, under the special condition of the jet temperature being equal to that of the ambient, can further be termed the adiabatic wall temperature.

In the case of impingement jets that are not isothermal with the surrounding environment, another important parameter is the impingement cooling or heating effectiveness, defined as follows:

$$E_f = \frac{T_{aw} - T_r}{T_0 - T_\infty} \tag{2.20}$$

where T_{aw} represents the adiabatic wall temperature, which is different from T_r as a result of the effects due to jet mixing with the ambient. For perfect cooling or heating performance, the effectiveness, E_f, should have a value of 1 (T_{aw} would be equal to the fluid stagnation temperature at the nozzle exit), while a value of 0 indicates that the temperature change between jet and ambient does not affect the fluid temperature at the wall [89].

2.6.2.7. Other non-dimensional parameters

According to Zuckerman and Lior [87], the non-dimensional parameters selected to describe impinging jet heat transfer include the fluid properties discussed in Sections 2.6.2.1 to 2.6.2.6, as well as those presented in Table 2.13.

Table 2.13. Additional non-dimensional parameters selected to describe impinging jet heat transfer

Non-dimensional parameter	Description
H/D	Nozzle height to nozzle diameter ratio
R/D	Radial position from the centre of the jet
z/D	Vertical position measured from the impingement surface
I	Turbulence intensity (usually evaluated at the jet nozzle)
M_c	Mach number based on nozzle exit, averaged, velocity
f	Relative nozzle area (total nozzle exit area divided by the total target area)
p_{jet}/D	Jet centre-to-centre spacing (pitch) to diameter ratio (valid for multiple jets)
A_f	Free area (1 minus the relative nozzle area)

2.6.3. Jet impingement research

The improvement and prediction of jet impingement behaviour may be conducted using either experimental or numerical investigations. Because this study focuses primarily on the experimental impingement of TiO_2-water nanofluids, the numerical works will be neglected.

Therefore, Section 2.6.3. focuses on the experimental techniques and investigations of jet impingement heat transfer problems. Subsequently, the following section defines the general experimental procedures used in the experimental modelling of jet impingement heat transfer, as well as summarises the multiple works where nanofluid is reported as the heat transfer fluid.

2.6.3.1. General experimental techniques

Typically, the experimental investigations of jet impingement heat transfer focus on the measurement of flow field characteristics and the heat transfer coefficients of the impinging target surface. In these studies, single or multiple jets with pre-determined nozzle geometry, angle and degree of confinement are positioned above a solid target. A pump or blower then proceeds to force the heat transfer fluid out of the jet nozzle and onto the solid surface, where calibrated instrumentation collects information about the fluid and target surface properties [87]. With this data recorded, it is possible to conduct the appropriate calculations and post-processing techniques that are needed to deduce theoretical observations and relations on the experimental results.

To minimise energy losses, which would influence the applicable measurements and hence result in an increased level of uncertainty, the back of the target surface is generally insulated with an appropriate material of the researcher's choice. Through these precautionary steps, the energy, generated by the surface, travels in a single-dimensional pathway, normal to the surface and with uniform heat flux.

The surface heat transfer coefficient is evaluated as follows:

$$h = \frac{\dot{q}}{(T_s - T_F)} \tag{2.21}$$

where T_s and T_F are the surface and far-field temperature values respectively and the surface heat flux is found by one of the following methods:

- When the target surface is insulated by means of an adiabatic material so that heat losses to the external environment are negligible, then the total electric power may be calculated as the input power. Subsequently, the heat flux may be approximated as follows:

$$\dot{q} = \frac{I^2 R}{A} = \frac{VI}{A} \tag{2.22}$$

- Alternatively, many research studies use Fourier's law of one-dimensional heat conduction to define the surface heat flux, illustrated as follows:

$$\dot{q} = -k\left(\frac{dT}{dz}\right) \tag{2.23}$$

where k is the thermal conductivity of the target surface and $\frac{dT}{dz}$ is the temperature gradient across the surface.

In obtaining temperature measurements required for the temperature gradient, temperature sensors are generally placed in discrete locations or for the entire target surface, through non-contact optical devices (i.e. infrared radiometers and thermally sensitive paints). However, in most cases, thermocouples are the preferred mechanism of taking temperature measurements and thus it is of great importance to make sure that they are embedded in or bonded carefully to the target surface [87].

With respect to monitoring fluid flow and pressure within the jet impingement system, volumetric or mass flow meters and pressure transducers are utilised at predetermined positions.

As reported previously, the Nusselt number is the dimensionless parameter that indicates the ratio of convective to conductive heat transfer and is found using equation 2.16. However, in an attempt to illustrate the dependency of this quantity on other dimensionless parameters, many researchers prefer to present their experimental results by means of an empirical correlation, which is typically expressed as follows:

$$Nu = CRe^n Pr^m f\left(\frac{H}{D}\right) \tag{2.24}$$

where C, n and m are constants, determined by the experimental investigation and $f\left(\frac{H}{D}\right)$ is an empirically determined function of nozzle height to target surface.

Note: Additional dimensionless parameters may be added to the expression in equation 2.24 to account for other effects of interests, such as jet pitch, pressure losses, surface geometry and curvature, and impingement angle.

In some experimental works, investigators focused on analysing the transient cooling behaviour of impinging jets. In these works, the target surface was not subject to a constant heat flux, but rather was heated to a predetermined temperature and then rapidly cooled down. Industrial applications of transient cooling are typically associated with quenching techniques, such as those used in the steel industry and generally involve additional physics such as boiling phenomena.

The rate of heat transfer, $\dot{q}$, of the test specimen under transient condition is generally assumed to be proportional to the temperature gradient and is expressed as follows:

$$\dot{q} = -\rho C_p \left(\frac{V}{A}\right)\frac{dT}{dt} \tag{2.25}$$

With the surface heat flux known, the surface heat transfer coefficient may be approximated as indicated by equation 2.21. Alternatively, Nayak et al. [102] offer the following expression to determine the heat transfer coefficient:

$$h = \frac{\rho \cdot C_p \cdot \tau \cdot CR}{T_s - T_c} \tag{2.26}$$

where τ represents the target's thickness and CR, the maximum cooling rate, is defined as follows:

$$CR = \frac{T_1 - T_2}{t_2 - t_1} \tag{2.27}$$

In addition to these calculations, some works used inverse heat conduction (IHC) analysis, which used the cooling curves generated from the transient temperature data of the target surface to produce the appropriate heat transfer coefficients. The IHC model is based on the minimisation method, developed by Beck et al. [103], and consists of two sub-models. For the first model, a one-dimensional estimation is used to predict the heat transfer coefficient, while the second is used to directly compute the two-dimensional temperature distribution of the target surface. At each time step, one of the required boundary conditions may be inversely estimated by the first sub-model to minimise the least squares errors between the computed and measured temperature values [104]. Fortunately, due to technological advancements and software development, IHC solvers such as INTEMP have been developed to perform the necessary computations required to find these surface temperatures and heat fluxes [105].

2.6.3.2. Previous works reporting on jet impingement by means of nanofluids

Tables 2.14 and 2.15 originate from previous experimental works that report on steady-state and transient jet impingement, where nanofluids have been considered as the heat transfer fluid. Therefore, these tables summarise the jet configurations, considered target surfaces and heating information, as well as the type, size, concentration and flow regime of the nanofluid used in the investigation. Furthermore, the tables also identify whether or not additional heat transfer physics, namely that of boiling phenomena, have been considered in the appropriate works.

Table 2.14. Steady-state works reporting on nanofluid jet impingement

Researcher	Type of jet and nozzle geometry	Target surface	Base fluid	Nanoparticle	Particle size [nm]	Particle concentration	Flow regime	Boiling inclusion	Remark(s)
Gherasim et al. [106]	Free surface and confined. Single circular nozzle.	Flat aluminium surface heated by seven 200W cartridge heating elements.	Water	Al_2O_3	47	0-6 vol.%	Fully developed laminar	No	Nusselt number increases with Re and particle concentration, while decreases with disk to nozzle spacing.
Jaberi et al. [107]	Free surface and confined. Single circular nozzle	Flat aluminium disk heated by 1 000W heating wire.	Water	Al_2O_3	15	0.0198 - 0.0757 wt.%	Fully developed turbulent	No	Convective heat transfer increases up to a certain particle concentration, after which an increase in concentration gives adverse results.
Li et al. [108]	Submerged and confined. Single circular nozzle.	Copper heated by a ceramic package resistance heater.	Water	Cu	25 100	1.5-3 vol.%	Transitional to fully developed turbulent	No	Nanofluids exhibit a remarkable increase in heat transfer rates.
Liu et al. [109]	Free surface and unconfined. Single circular nozzle.	Copper block heated by a ribbon electric heater.	Water	CuO	50	0.1-2 wt.%	Fully developed turbulent	Yes	Critical heat flux increases by 25% for nanofluids.
Lv et al. [81]	Free surface and unconfined. Single circular jet.	Copper surface heated by a heating disk.	Water	SiO_2	N/A	1-3 vol.%	Fully developed turbulent	No	Convective heat transfer increases with an increase in volume fraction and Re number. Heat transfer coefficient is highest when jet impinges vertically (90° to target surface).
Naphon et al. [110]	Free surface and confined. Single circular jet.	Mini-rectangular fin heat sink for cooling of a computer processing unit.	DI-water	TiO_2	21	0.4 vol.%	N/A	No	Higher cooling rates are observed for the use of nanofluids in comparison with pure water.
Nguyen et al. [111]	Submerged and confined. Single circular nozzle.	Flat aluminium surface heated by two 100W heaters.	DI-water	Al_2O_3	36	0-6 vol.%	Fully developed turbulent	No	Adverse effects on heat transfer behaviour are observed when using nanofluids.
Nguyen et al. [112]	Submerged and confined. Single circular nozzle.	Flat aluminium surface heated by two 100W heaters.	DI-water	Al_2O_3	36	0-5 vol%	Transitional to fully developed turbulent	No	Nanofluid produces a clear erosion effect on the target surface.

Sun et al. [113]	Free surface and unconfined. Single circular and square nozzle.	Flat copper surface heated by two 50W ceramic heating cores.	DI-water	Cu	N/A	0.1-0.5 wt.%	Transitional to fully developed turbulent	No	Convective heat transfer coefficient increases with mass fraction and appears higher for the circular nozzle than for the square nozzle.
Sun et al. [3]	Free surface and unconfined. Single circular nozzle with/without swirling effects.	Copper heated by four 50W ceramic heaters. Multiple target surface structures considered.	DI-water	Ag-MWCNTs	N/A	0.01-0.05 wt.%	Fully developed turbulent	No	Heat transfer performance increases with the mass fraction of nanoparticles and appears better under swirling conditions.
Teamah et al. [114]	Free surface and confined. Single circular jet.	Stainless steel plate heated by saturated steam generated by three electric heaters of 6kW capacity.	DI-water	Al_2O_3	36	0-10 vol.%	Fully developed turbulent	No	Heat transfer increases as the Re number increases at constant particle concentration.
Tie et al. [4]	Multiple free surface and confined jets with circular nozzles.	Copper block heated by six cartridge heaters.	Water	Cu	26	0.17-0.68 vol.%	Fully developed turbulent	No	Depending on combinations used, nanofluids may result in either positive or adverse effects on heat transfer rates.
Wongcharee et al. [115]	Free surface and unconfined. Single circular nozzle with/without swirling effects.	Stainless steel plate heated by an electric heater.	Water	TiO_2	30-50	0-2.5 vol.%	Fully developed turbulent	No	Under similar operating conditions, swirling jets produce superior heat transfer to conventional jets. Heat transfer performance increases with mass fraction of nanoparticles.
Yousefi et al. [116]	Free surface and unconfined. Single-slot jet.	V-shaped Inconel plate heated by a maximum power supply of 720W.	Water	Al_2O_3	15	0.02-0.15 vol.%	Fully developed laminar	No	Convective heat transfer increases up to a certain particle concentration, after which a further increase produces negative effects.
Zeitoun et al. [117]	Free surface and confined. Single circular jet.	Both copper and aluminium plates heated with a heat flux within the range of 60-100kW/m^2.	Water	Al_2O_3	10	0-10 wt.%	Transitional to fully developed turbulent	No	Nusselt number increases up to 100% for higher concentrations at the same Re number.
Zhou et al. [118]	Multiple submerged and confined circular jets.	Copper surfaces, with and without pin fins, heated by four heating rods with a power rating of 80W.	Water	Ag	4.8	0.02-0.12 wt.%	Dissipated to fully developed laminar flow	No	Heat transfer coefficient of the target surface with pin fins is greater than for the surface without pin fins. Both cases show enhanced cooling with the use of nanofluids.

Table 2.15. Transient state works reporting on nanofluid jet impingement

Researcher	Type of jet and nozzle geometry	Target surface	Base fluid	Nanoparticle	Particle size [nm]	Particle concentration	Flow regime	Boiling phenomena	Remark(s)
Mitra et al. [119]	Multiple free surface and unconfined circular nozzles (tube bank).	Steel heated to ±930 ℃	Water	TiO_2 MWCNT	20-70	0.01 Wt.% 0.1 Wt.%	Fully developed laminar	Yes	Heat transfer performance increases marginally by using nanofluids.
Modak et al. [120]	Free surface and unconfined. Single circular nozzle.	Stainless steel heated to 500 ℃	Water	Al_2O_3	<100	0-0.6 vol.%	Fully developed turbulent	Yes	Nanofluids exhibit a remarkable increase in heat transfer rates and result in quicker cooling time.
Nayak et al. [102]	2 Free surface and unconfined circular nozzles.	Steel heated to 700 ℃	DI-water	Al_2O_3 TiO_2	20	0-0.07 Wt.%	N/A	Yes	Depending on the combinations used, nanofluids may result in either positive or adverse effects on heat transfer behaviour.
Sarkar et al. [121]	Free surface and unconfined. Single circular nozzle.	Stainless steel plate heated to 1 050 ℃	DI-water	Cu-Al LDH	57.69	0-200 PPM	Fully developed turbulent	Yes	Convective heat transfer increases up to a certain particle concentration, after which an increase in concentration gives adverse results.
Singh et al. [122]	Free surface and unconfined. Single circular nozzle	Steel plate heated to 1 100 ℃.	Water	TiO_2 SiO_2 Al_2O_3	50 70 20	0.1-1 wt.%	Fully developed laminar	Yes	Nanofluids exhibit a remarkable increase in heat transfer rates and result in quicker cooling time.
Tiara et al. [105]	Free surface and unconfined. Single circular nozzle.	Stainless steel heated to 900 ℃	DI-water	Cu-Al LDH	N/A	120 PPM	N/A	Yes	Heat transfer coefficient showed an increasing trend with a decrease in surface temperature for all concentrations. Deposition of nanoparticles occurs on target surface.
Tiara et al. [123]	Free surface and unconfined. Single circular nozzle.	Stainless steel heated to 900 ℃	Water	Al_2O_3	14	0-20 PPM	N/A	Yes	Heat transfer coefficient showed an increasing trend with a decrease in surface temperature for all concentrations. Deposition of nanoparticles occurs on target surface.

An initial analysis of Tables 2.14 and 2.15 indicates that a substantial number of researchers shifted their focus towards the use of nanofluids for jet-impingement cooling applications. Of the many works considered, it is shown that conventional impingement configurations are single free-surface confined set-ups, which use a circular-shaped nozzle to cool a flat target surface. As for nanofluid selection, although several particle types were considered, investigations appear to favour Al_2O_3 particles and remain restricted to water-based fluids, regardless of the flow conditions considered.

Regarding the nature of the different types of impingement cooling, it is shown that almost all steady-state works, with exception of [109], were conducted for pure convective heat transfer, while the entire range of transient works includes the effects of boiling phenomena. Additionally, it is also indicated that all transient state investigations were conducted for flat target surfaces of stainless steel and hence are limited in their focus and application.

Despite the fact that the consensus of Tables 2.14 and 2.15 is that nanofluids enhance the thermal performance of jet-impingement cooling, it should be noted that some works do report on adverse effects when exceeding a particular particle concentration. Examples of works where adverse effects were noted are [4, 102, 107, 111, 121]. Additionally, it may also be concluded that the degree of heat transfer enhancement is directly proportional to the Reynolds number of the system (a higher Reynolds number results in higher jet impingement heat transfer).

Based on the nature and general trends of the presented works, there is sufficient research potential in investigating both the steady- and transient state cooling of a non-steel target surface using varying volume concentrations of none-Al_2O_3-water nanofluids. Therefore, this study investigates the cooling of a heated copper target surface using TiO_2-water nanofluids for both steady- and transient state conditions.

2.7. Summary and conclusions

A nanofluid is a homogeneous solution where nanoparticles are suspended in a base fluid by means of a single-step or two-step approach in an attempt to enhance its thermal properties. Depending on the preparation method chosen, fluid stability may vary and can be tested and improved upon by many different techniques.

In terms of effectively modelling nanofluids and their appropriate thermophysical properties, it was shown that no single model has been developed which accounts for all parameters that source the respective behaviour of the fluid. Therefore, despite the wide range of traditional, modified and empirical correlations available, further development of a more accurate and reliable model capable of operating in non-experimental environments is required. Justification of a hybrid model is prevalent among the prediction of nanofluid thermal conductivity and viscosity respectively.

The classification of jet impingement configurations was shown to vary depending on the relationship of impingement and ambient fluid, the level of confinement instilled upon the set-up and the selected nozzle geometry. Furthermore, additional classification was found to depend on the number of jets, target surface geometry, impingement angle and other conditions utilised in the desired application. The most important dimensionless parameters and relations pertaining to jet impingement were defined and discussed in this chapter.

Upon analysis of general experimental procedures, alternative methods to approximate the surface heat flux and heat transfer coefficient of jet impingement studies were discussed, with substantial importance being

placed on the nature of the flow and boundary conditions. The review of experimental works indicated that most investigators considered steady-state conditions, while only a few accounted for transient cooling. Furthermore, with respect to these transient works, no investigator deviated from stainless steel without the influence of boiling phenomena. With respect to the noted trends, the present study investigates the cooling of a heated copper target surface by means of TiO_2-water nanofluids for both steady- and transient state cooling applications.

3. Experimental description

3.1. Introduction

The purpose of this chapter is to define the configuration of the experimental set-up, which was used to conduct the appropriate jet-impingement cooling tests utilising both pure water and varying volume fractions of TiO_2-water nanofluid. In addition to the basic make-up of the test rig, each of the main components is further defined to provide details of their instrumentation and overall purpose. Lastly, the data reduction techniques, experimental procedure and resulting experimental uncertainties are also included in this chapter.

3.2. Experimental set-up

Figure 3.1 schematically represents the experimental set-up used in the study. As indicated in the figure, the free-surface single-jet impingement system accommodated fluid delivery by means of a multi-tank and pump system. Fluid flow within this particular system may be classified as either open or closed depending on the configuration of the return valve that connected the main reservoir and drainage tank.

In addition to the fluid delivery system defined above, the set-up also consisted of a heated target surface or test section, a data acquisition system and, lastly, safety devices and mechanisms that were implemented to prevent nanofluid exposure. The nature of the systems is discussed in further detail below.

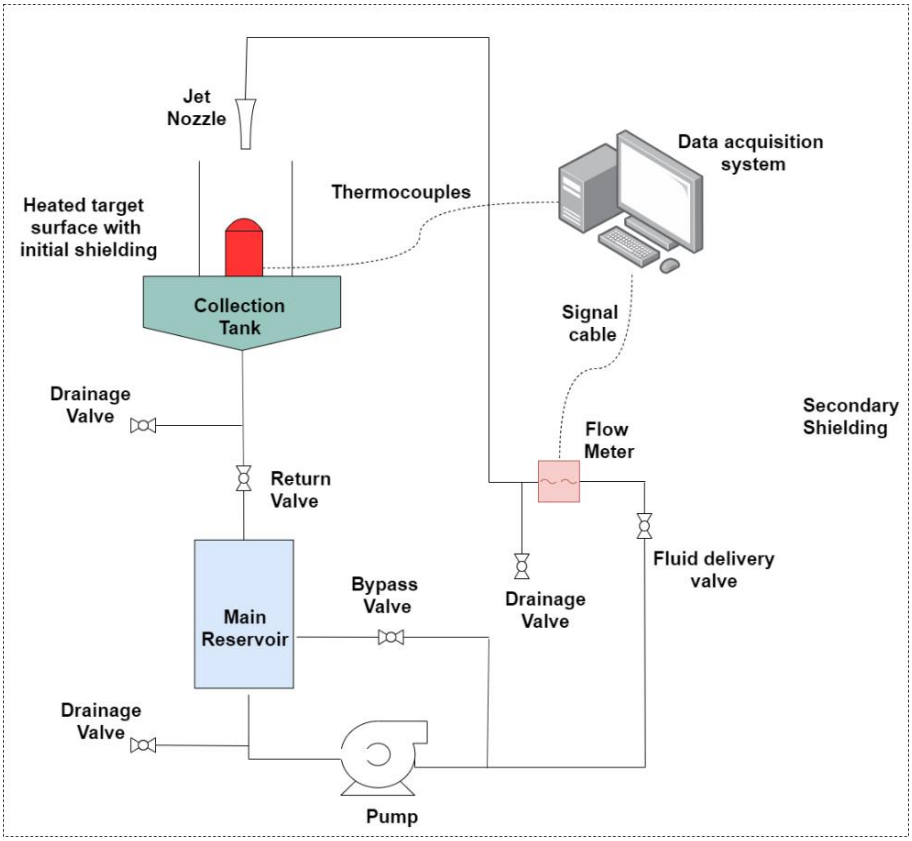

Figure 3.1. Schematic representation of experimental set-up used for jet-impingement cooling tests

3.2.1. Fluid delivery system

As shown in Figure 3.1, the applicable fluid circuit consisted of a reservoir tank, a centrifugal pump (BADU 45/16 Spa pump, supplied by Speck Pumps), an ultrasonic flow meter (Type 8081, supplied by Bürkert), an orifice jet nozzle (1.65 mm diameter Lechler nozzle, supplied by Industrial Nozzles and Systems) and a customised drainage tank (manufactured by Kare Sheet Metal Products).

The initial reservoir or tank, with a maximum capacity of 10 litres, was employed to store the 6 litres of fluid used for the jet cooling tests. A K-type thermal couple (1.5mm RS Pro Type K thermocouples supplied by RS components) was placed in the reservoir to monitor the fluid temperature and hence ensure that all tests commenced at approximately the same initial fluid temperature. In addition to the tank thermocouple, another thermocouple was also placed in the jet to observe the impinging fluid temperature. For the experimental investigation, the jet nozzle was positioned 6.6 mm or H/D= 4, above the heated target surface.

For the investigation, a wide range of Reynolds numbers were considered by means of adjusting the flow rate of the fluid exiting the orifice jet nozzle. These flow rates were monitored by the ultrasonic flow meter and were controlled through a solid-state relay system that was connected to the centrifugal pump. Additionally, a bypass or return line was also available, should the flow rate require further adjustment beyond the extent offered by the pump control system.

Once exiting the jet nozzle, the HTF was impinged upon the heated target surface and collected in the customised drainage tank, at which point it could either be stored, drained for collection or allowed to return to the main fluid reservoir. The functionality was controlled through two ball valves. In addition to the main drainage valve located at the base of the drainage tank, an additional two valves were positioned at the base of the main fluid reservoir and along the fluid delivery line to assist in draining of all residual nanofluid. The use of the additional drainage valves was also beneficial in terms of flushing the system with water to ensure that no nanofluid deposition occurred, especially within the flow meter.

3.2.2. Test section

The test section or heated target surface consisted of a round copper bar with an initial diameter of 62.45 mm and a total length of 100.01 mm. The bar was tapered at the one end to produce a reduced diameter of 42 mm that would allow for a larger total surface heat flux.

To facilitate the heating of the specimen, six cartridge heaters of 220 V and 100 W power capacity (Marathon Heaters INC, USA) were placed in holes drilled into the base of the cylinder. Similar to the pump, these heaters were also connected to a solid-state relay system to allow for the control of the electrical power input. The total electrical power input was observed through the use of a type 2053-amp meter (Yokogawa, Japan) and a type 2052-voltmeter (Yokogawa, Japan), which were connected in series and parallel to the heaters respectively.

The tapered side of the test specimen included five holes of 1.5 mm diameter, which were drilled at various axial levels from the surface of the bar. Each of these holes was approximately 15 mm deep and was manufactured to house five K-type thermocouples (1.5mm RS Pro Type K thermocouples supplied by RS components), which would track the temperature data of the specimen during the experimental runs. To reduce any electrical interference, the thermocouples had an insulated hot junction. To prevent any air gaps which could potentially result in disturbances or fluctuations in the thermocouple readings, each of the holes was filled with a thermal paste (silicone heat transfer compound supplied by Unick Chemical Corp.) with a thermal conductivity rating of 0.628 W/m·K. In order to reduce thermal losses, the copper bar was insulated

by means of a polytetrafluoroethylene (PTFE) casing. The PTFE housing, with the copper bar, was positioned on a customised stand, which sat above the manufactured collection tray.

In addition to monitoring the electrical heat input and heat transfer through the copper specimen, five T-type thermocouples were also positioned around the edge of the copper surface to capture the thermal data of the HTF after impingement upon the target surface. By means of the thermal readings and those of the jet inlet temperature, it was possible to approximate and monitor the total fluid heat transfer as well.

Figure 3.2 schematically depicts the overall geometry of the copper test specimen, the locations of the six cartridge heaters inserted into its base and the axial locations of the five internal K-type thermocouples.

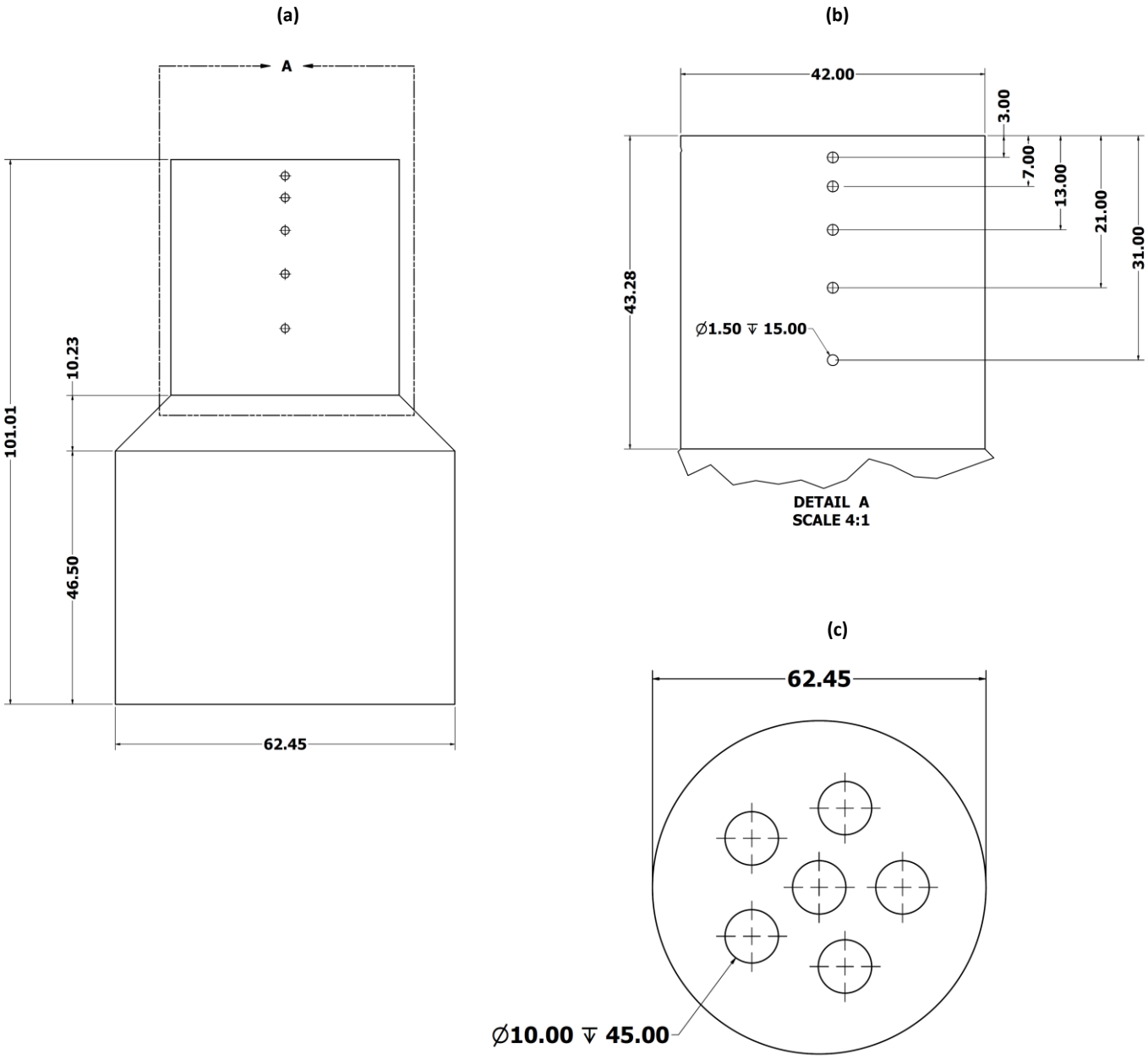

Figure 3.2. Schematic representation of (a) copper test specimen, (b) the axial locations of the five internal thermocouples and (c) positioning of the six cartridge heaters within the base of the copper specimen

3.2.3. Data acquisition system

All thermal and current output data generated by the thermocouples and ultrasonic flow meter respectively was recorded using an SCXI-1303 data logger (National Instruments, USA). The data logger had a 32-channel input capacity and was connected to a computer where a LabView program was used to sample data at a predetermined frequency. Once an experimental run was completed, the appropriate data files were saved to the computer, at which point they might undergo post-processing.

For the purpose of the investigation, all post-processing activities were conducted using spreadsheets generated on Microsoft Excel and coded scripts that were created within Python. Before using these tools to apply the data reduction technique discussed in section 3.3, the raw recorded data was firstly adjusted according to the appropriate calibrations factors (discussed in Appendix A).

3.2.4. Safety system

In addition to the different applications and properties of nanofluids, Krajnik et al. [6] emphasise the importance of understanding the potential health and safety risks associated with the use of these fluids. They report that nanoparticles are the main occupational health and safety risk (OHS) associated with nanofluids and thus a comprehensive understanding of different particles and their resulting toxicology is required.

According to Sajid et al. [124], nanoparticle toxicology depends on a number of factors, namely size, nature, reactivity, mobility, stability, surface chemistry and charge, the occurrence of agglomeration, and lastly, the storage medium and time. Mechanisms of potential exposure to nanoparticles such as dermal penetration, respiratory intake via inhalation and digestive intake by means of ingestion are discussed. For the purpose of this study, only the former two mechanisms of exposure were considered applicable and therefore had to be prevented for the health and safety of the investigator and laboratory staff.

To prevent exposure to the nanofluid and nanoparticles used in the experimental tests, different safety structures were included on the test rig. As indicated in Figure 3.1, these structures are classified as initial shielding and secondary shielding components. The initial shielding refers to the barrier that surrounds the test specimen and therefore prevents splashing of the fluid once impingement has occurred. The initial shielding consisted of a Perspex cylinder attached to a platform and a Perspex lid that fitted around the jet nozzle to reduce fluid evaporation. The secondary shielding included the external polycarbonate housing that surrounded the entire test rig, as well as the drip tray in which the set-up sat. By means of this secondary shielding, any leaks or rogue expansion of nanofluid, following impingement upon the target surface, was contained. Lastly, the rig was also equipped with an emergency shower system should thorough cleansing of the system be required. This system was connected to a nearby water supply, positioned behind the test rig.

Although safety systems or structures were included in the design and manufacturing of the test set-up, it was still of the utmost importance to ensure that the correct caution and protective personal equipment (PPE) was used throughout the various cooling tests. The PPE included chemical-resistant gloves, safety goggles, a respiratory mask and a certified dust or laboratory coat.

Figure 3.3 provides a photographic representation of the experimental rig and the various components and systems discussed above.

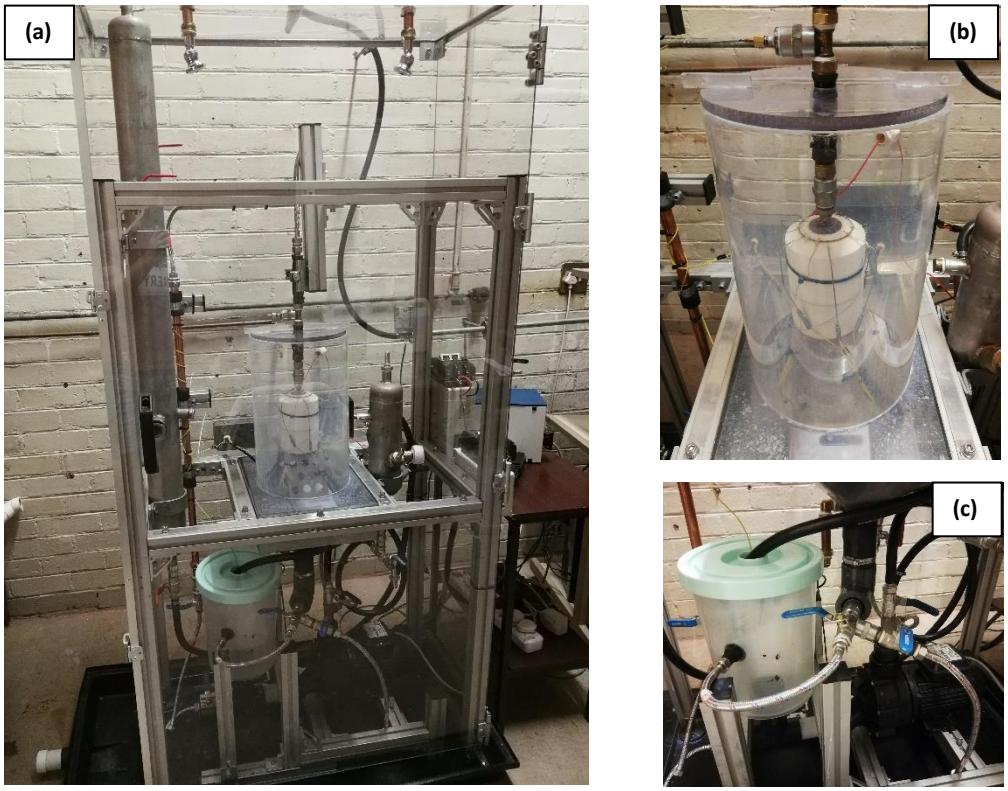

Figure 3.3. Photographic representation of (a) overall jet impingement experimental set-up, (b) close-up of jet and target surface and (c) close-up of main tank and drainage valves

3.3. Data reduction

The bulk fluid temperature was determined by taking the average of the inlet jet temperature and the mean exit temperature of the fluid, once it had impinged upon the target surface. This temperature value was the temperature for which all HTF properties were calculated and was defined as follows:

$$T_b = \frac{T_j + \bar{T}_e}{2} \tag{3.1}$$

The mean exit fluid temperature, shown above, was determined as follows:

$$\bar{T}_e = \frac{T_{e,1} + T_{e,2} + T_{e,3} + T_{e,4} + T_{e,5}}{5} \tag{3.2}$$

The properties of pure water were determined using the thermophysical correlations for liquid water as proposed by Popiel et al. [125]. The thermophysical properties of the different nanofluid volume fractions were approximated by means of a number of equations and measurements, which are discussed in the following chapter.

The mass flow rate of fluid during the different cooling tests was approximated through the following expression:

$$\dot{m} = \rho \dot{V} \tag{3.3}$$

where $\dot{V}$ is the volume flow rate, determined from the current output of the ultrasonic flow meter, and ρ is the appropriate fluid density at the bulk fluid temperature.

To determine the exit fluid velocity, the volume flow rate ($\dot{V}$) and jet cross-sectional area (A_j) were utilised as follows:

$$U = \frac{\dot{V}}{A_j} \tag{3.4}$$

Using the expression defined in Section 2.6.2, the Reynolds number within the system was calculated as follows:

$$Re = \frac{\rho \cdot U \cdot D_j}{\mu} \tag{3.5}$$

where all fluid properties were determined at the bulk fluid temperature.

Based on the readings of the amp and voltmeter respectively, the total electrical power input into the heated specimen at a particular power setting was determined as follows:

$$\dot{Q}_{electric} = V \cdot I \tag{3.6}$$

With the input electrical power known, as well as the arrangement of the different thermocouples in the system, the heat flux of the copper specimen was determined in various ways. One such method, assuming that no heat loss occurred between the specimen and the surroundings, was to divide the electrical input power by the area of the target surface. This approximation is presented as follows:

$$\dot{q} = \frac{\dot{Q}_{electric}}{A_s} \tag{3.7}$$

Another method, used in [81, 118] and [126], was to assume one-dimensional heat transfer and then to use Fourier's law of heat conduction to determine the heat flux through the copper cylinder. The heat flux across any two thermocouple levels of the copper specimen was determined as follows:

$$\dot{q} = -k_c \cdot \frac{\Delta T}{\Delta x} \tag{3.8}$$

where k_c is the thermal conductivity of the copper target surface and ΔT and Δx are the temperature and spacing differences between the respective thermocouple levels. Because several thermocouples were placed at different levels in the specimen, a weighted heat flux was calculated as follows:

$$\dot{q}_{weight} = \frac{\sum_{i=1}^{4}(\Delta x \cdot \dot{q})_{i,i+1}}{\sum_{i=1}^{4}\Delta x_{i,i+1}} \tag{3.9}$$

As for the final approach to calculating the heat flux, equation 3.10 was also used as follows:

$$\dot{q} = \frac{\dot{m}c_p\left(T_j - T_e\right)}{A_s} \tag{3.10}$$

where c_p is the specific heat of the fluid at the bulk fluid temperature, T_j is the inlet jet temperature, T_e is the average exit temperature of the fluid and A_s is the surface area of the target surface.

For the purpose of the investigation, the approach described by equations 3.8 and 3.9 was used, while the other techniques were used for energy balance purposes and to validate the physics of the experimental model. This validation will be elaborated on in Chapter 5.

With the heat flux of the copper specimen known, the surface temperature of the specimen, based on any of its five internal thermocouples, was approximated as follows:

$$T_{s,i} = T_{TC,i} - \frac{\dot{q}_{weight}\Delta x_{s,i}}{k_c} \tag{3.11}$$

where $T_{TC,i}$ is the temperature reading of the applicable thermocouple and $\Delta x_{s,i}$ is the distance between the surface and the position of the appropriate thermocouple.

The average surface temperature was found by averaging the five surface temperature values as follows:

$$\bar{T}_s = \frac{T_{s,1} + T_{s,2} + T_{s,3} + T_{s,4} + T_{s,5}}{5} \tag{3.12}$$

With the heat flux, surface temperature and jet temperature available, the average surface heat transfer coefficient was determined as follows:

$$h = \frac{\dot{q}}{T_s - T_j} \tag{3.13}$$

The average Nusselt number was approximated using the following expression:

$$Nu = h \cdot \frac{D_j}{k} \tag{3.14}$$

where D_j is the jet nozzle diameter and k is the thermal conductivity of the HTF at the bulk fluid temperature.

As indicated earlier, the arrangement and nature of the different thermocouples used in the test rig allowed the monitoring of heat transfer within both the copper specimen and the HTF. The heat transfer quantities were determined as follows:

$$\dot{Q}_c = \dot{q}_{weight} \cdot A_s \tag{3.15}$$

$$\dot{Q}_{fluid} = \dot{m} \cdot c_p \cdot (T_e - T_j) \tag{3.16}$$

Because the total electrical power supplied to the target surface was also known, the following energy balance was employed:

$$\dot{Q}_{electric} \approx \dot{Q}_c \approx \dot{Q}_{fluid} \tag{3.17}$$

Based on equation 3.17, the heat transfer rate of the copper specimen was compared with that of the electrical power input and HTF by employing the following energy balances:

$$EB = \left| \frac{\dot{Q}_{electric} - \dot{Q}_c}{\dot{Q}_{electric}} \right| \times 100 \tag{3.18}$$

$$EB = \left| \frac{\dot{Q}_c - \dot{Q}_{fluid}}{\dot{Q}_c} \right| \times 100 \tag{3.19}$$

The many steady-state impingement tests indicated that the average energy balance between the electrical input power and the copper specimen was approximately 12.63%, while that of the specimen and HTF was 6.92%.

With respect to the transient cooling analysis of the different HTFs, the cooling curves of surface temperature versus time were generated and analysed. In order to eliminate the effects of jet inlet temperature on the analysis, the transient surface temperature of the specimen, with respect to time, was non-dimensionalised as follows:

$$\theta = \frac{T_s - T_j}{T_j} \tag{3.20}$$

3.4. Experimental procedure

The experimental investigation aimed to analyse both the steady-state and transient cooling of a heated copper cylinder by means of DI-water and varying volume fractions of TiO_2-water nanofluids. With respect to the particle concentrations considered, nanofluid mixtures of 0.025, 0.05, 0.1, 0.25, 0.5 and 1% were prepared and tested. Due to the varying nature of the different impingement tests conducted, the experimental procedure is defined separately for both the steady-state and transient cooling tests in the next section.

3.4.1. Steady-state jet impingement tests

Once the appropriate HTF had been introduced into the main fluid reservoir, the power dial controlling the six cartridge heaters was adjusted to produce the desired electrical power input based on the readings of the amp and voltmeter respectively. For the purpose of the investigation, the power input was approximately 145 W and was generated at a setting of 35% on the solid-state relay control. To monitor the heating process, the five internal thermocouple readings were observed via the LabView program on the computer. This process generally took five minutes to heat the copper specimen from ambient temperature to 50 ℃.

While heating the target surface, the power dial controlling the centrifugal pump was adjusted to produce the required volume flow rate for the respective impingement test. Based on the initial calibration of the test rig, the power settings ranged between 45 and 100% on the solid-state relay and were capable of producing Reynolds numbers in the range of 10 000 to 30 000.

Once the specimen reached the desired temperature of 50 ℃, the circuit breaker for the pump was switched on and the impingement cooling process was initiated. As these tests were to be done for a constant surface heat flux, the power supply to the heaters remained undisturbed for the duration of the runs. Based on the initial calibration tests, initiated at a temperature of 50 ℃, steady-state conditions were achieved within the

first minute of cooling. Regarding the recording and post-processing of the data, the cooling data was recorded immediately after the pump was turned on for a duration of three minutes. To obtain the time-averaged steady-state data, only the final minute of each cooling run was considered.

Upon completion of each experimental run, the return valve between the drainage tank and the main fluid reservoir was opened. Once the HTF had returned to the reservoir, it was allowed to cool down to a temperature of 21 to 23 ℃. The thermocouple positioned within the main reservoir was used to monitor this temperature value to ensure that each test was initiated at approximately the same fluid temperature. Each fluid test was repeated at least three times to ensure repeatability and reliability of data.

3.4.2. Transient state jet impingement tests

In addition to the steady-state impingement runs, the investigation also sought to compare the overall efficiency of the various TiO_2-water nanofluids for transient cooling. These tests were conducted through heating the copper specimen to a predetermined temperature, turning off the heaters and initiating the impingement cooling process. A temperature value of 105 ℃ was selected for the initial specimen temperature to obtain transient cooling data where the effects of boiling phenomena were ignored; a case that has not been considered in the cited works pertaining to transient impingement by means of nanofluids.

Regarding the pump settings used in the investigation, the time-sensitive nature of the transient surface temperature would not allow for the time required for the stabilisation of flow rates at lower pump power settings and thus only the maximum power setting of 100% was considered. Once initiating the cooling process, the thermal data of the five internal thermocouples was recorded until reaching a temperature value of below 40 ℃. This particular temperature value was chosen based on the fact that cooling appeared rapid until approximately 35 ℃, at which point the time to reach a constant temperature was greater than the amount of fluid available to the system.

Once obtaining the appropriate surface temperature data with respect to time, the data was non-dimensionalised through the use of equation 3.20 in an attempt to eliminate the effects of the inlet jet temperature. Similar to the steady-state tests, upon completion of each run, the fluid was returned to the main reservoir where it was allowed to cool before conducting the next experimental run. Each test was repeated in an attempt to improve the reliability of the data.

3.4.3. Post-testing procedure

Once both the steady-state and transient tests had all been completed for a given HTF (either water or a particular volume fraction of TiO_2-water nanofluid), the fluid was pumped from the main fluid reservoir to the drainage tank, at which point it was drained. To ensure that the maximum amount of fluid was collected from the system, the additional two drainage valves, discussed in Section 3.2.1, were also used. Once ensuring that the system had been drained sufficiently, distilled water was pumped throughout the system in order to ensure that no particle deposition occurred and to remove any contaminants that could potentially inhibit the flow through the relatively small diameter of the orifice jet nozzle. This process was repeated several times to ensure that the system was cleaned thoroughly before testing with a new fluid.

In addition to cleaning the fluid delivery system between the different fluid tests, the copper target surface was also cleaned of all residual nanoparticles and impurities that could potentially inhibit the heat transfer of the surface.

3.5. Uncertainties

All uncertainties were approximated within the 95% confidence level utilising the procedure defined by Moffat [127] and Dunn [128]. The full uncertainty analysis pertaining to this investigation is presented in Appendix B.

Tables 3.1 to 3.4 depict the associated uncertainties approximated for the various instrumentation, fluid properties and experimental parameters calculated during the current investigation.

Table 3.1. Range and associated uncertainty of measuring instruments

Instrument	Range	Uncertainty
Thermocouple	< 150 ℃	0.12℃
Flow meter	0 - 50 L/min	± 0.01% of full range and 2% of measured value
Amp meter	0 – 2.5 A	2% of nominal value
Voltmeter	0 – 300 V	1.7% of nominal value
Vernier Caliper	0-150 mm	0.02 mm

Table 3.2. Uncertainties associated with calculated fluid properties

Property	Water	0.025 Vol. %	0.05 Vol. %	0.1 Vol. %	0.25 Vol. %	0.5 Vol. %	1 Vol. %
$\rho\ [kg/m^3]$	0.003%	0.003%	0.003%	0.003%	0.003%	0.003%	0.003%
$c_p\ [J/kg \cdot K]$	0.04%	0.044%	0.044%	0.044%	0.043%	0.043%	0.042%
$k\ [W/m \cdot K\ ]$	2%	2%	2%	2.01%	2.03%	2.05%	2.12%
$\mu\ [kg/m \cdot s]$	1%	1%	1%	1%	1%	1%	1%

Table 3.3. Uncertainties associated with calculated parameters at varying particle volume concentrations

Parameter	Uncertainty at particle volume fraction						
	0%	0.025%	0.05%	0.1%	0.25%	0.5%	1%
$\dot{q}$	0.15%	0.15%	0.15-0.16%	0.15%	0.14-0.15%	0.14-0.15%	0.14-0.15%
h	1.75-3.55%	1.37-3.17%	1.38-3.33%	1.69-3.26%	1.58-2.9%	1.26- 2.99%	1.28-2.92%
Nu	2.66-4.08%	2.43-3.75%	2.43-3.88%	2.63-3.83%	2.57- 3.54%	2.41- 3.63%	2.47-3.61%

3.6. Summary and conclusions

The experimental set-up, data reduction methodology as well as the experimental procedure and resulting uncertainty analysis were all discussed in this chapter.

The constructed test rig consisted of a heated copper cylinder of 42 mm diameter, which was cooled by means of a 1.65 mm orifice jet nozzle, located four nozzle lengths above the target surface. During the investigation, jet-impingement cooling under steady-state and transient conditions were considered, where varying volume fractions of TiO_2-water nanofluid were compared.

With respect to the steady-state tests, the heated target surface was subject to a constant heat flux and cooled at varying Reynolds numbers ranging between 10 000 and 30 000. Thermal data for both the fluid and test specimen was recorded by means of strategically placed thermocouples inside the copper specimen, along the edge of the impingement surface and within the jet itself. The volumetric flow rates of the varying HTF were recorded through a current output signal that was produced by the ultrasonic flow meter.

As for the transient investigation, the transient cooling curves of the copper surface temperature against time were obtained and compared. These tests ignored the phenomenon of boiling and were limited to the

maximum pumping power due to the time-sensitive nature of the transient surface temperature. To eliminate the unwanted effects of the inlet jet temperature, the surface temperature data was non-dimensionalised before analysis.

Upon completion of the appropriate uncertainty analysis, it was observed that the uncertainty in the approximated surface heat flux remained constant at 0.15%. Regarding the uncertainties of the other calculated parameters, it was shown that the uncertainty of the HTC remained between 1.26 and 3.55%, while the maximum uncertainty of the calculated Nusselt number remained below 4%. The magnitude of these uncertainty values appeared to be directly proportional to the flow rate or Reynolds number of the respective fluid tests. Additional uncertainty data for the appropriate instrumentation and calculated fluid properties was also included in the uncertainty analysis.

4. Nanofluid preparation, characterisation and stability analysis

4.1. Introduction

This chapter presents the preparation, characterisation and resulting stability of the different volume fractions of TiO_2-water nanofluids that were prepared during the experimental study. Therefore, the various thermophysical properties obtained through experimental measurements as well as by means of existing models are presented and discussed. With respect to the reported stability of the prepared samples, the different tests conducted as well as their appropriate results are also included and discussed. Lastly, the particle morphology of the TiO_2 nanoparticles is also included and discussed in this chapter.

4.2. Preparation

Concentrated TiO_2-water nanofluid (15 wt. %), prepared through a single-step method, was procured from US Research Nanomaterials Inc (USA), where the average particle size was specified to be 5 to 30 nm. For the purpose of the investigation, six different particle volume fractions, namely 0.025, 0.05, 0.1, 0.25, 0.5 and 1%, were prepared by means of diluting the concentrated mixture with deionised water. As the study's focus was to investigate the thermal performance of the selected nanofluid in jet impingement applications, the particle volume fraction was modified until heat transfer was no longer enhanced. Consequently, and as will be discussed in section 5, it was not necessary to test fluids at a higher or lower particle concentration.

To determine the initial volume concentration of the supplied TiO_2-water dispersion, the following expression relating weight to volume fraction was used in conjunction with the material properties presented in Table 4.1:

$$\varphi = \frac{\emptyset \cdot \rho_{bf}}{\emptyset \cdot \rho_{bf} + \rho_{np}(1 - \emptyset)} \tag{4.1}$$

Table 4.1. Thermophysical properties of TiO_2 nanoparticles and DI-water at an average temperature of 25 °C

Property	Base fluid (DI-water)	TiO_2 nanoparticles
$\boldsymbol{\rho}$ $(\boldsymbol{kg/m^3})$	997.1	4 250
$\boldsymbol{c_p}$ $(\boldsymbol{J/kg \cdot K})$	4 180	686
$\boldsymbol{k}$ $(\boldsymbol{W/m \cdot K})$	0.607	8.954
$\boldsymbol{\mu}$ $(\boldsymbol{kg/m \cdot s})$	8.91×10^{-4}	-

Substituting the appropriate quantities into equation 4.1, produced an initial volume concentration of approximately 4%.

As a large volume of nanofluid was required for the jet cooling tests, namely 6 litres, the dilution process occurred in multiple batches of 250 ml. The volume of DI-water to be added, ΔV, in order to attain a particular volume fraction, φ_2, was determined as follows:

$$\Delta V = V_2 - V_1 = V_1 \cdot (\frac{\varphi_1}{\varphi_2} - 1) \tag{4.2}$$

In order to break down particle agglomeration and ensure the preparation of a stable and homogeneous nanofluid, a Q700 ultrasonicator (QSonica, USA) was used. The sonicator was set to an amplitude of 70% for a duration of 30 minutes with a pulsating duration of 5 seconds on and 2 seconds off. In an attempt to prevent evaporation and ensure that the nanoparticles were not burnt, the glass beaker containing the nanofluid was placed in a thermal bath with a temperature setting of 15 °C. Once a batch of fluid had undergone sonication, it was added to a 10-litre container that would be used to transport all the fluid to the main reservoir of the set-up. Before testing of a prepared nanofluid could begin, samples were collected and characterised in terms of their stability and thermophysical properties (this is expanded on in Sections 4.3 and 4.4).

Upon initial analysis of the visual appearance of the different fluid samples, it was observed that particle sedimentation had begun to occur relatively soon after sonication for volume fractions below 0.5%. Based on this phenomenon, it was concluded that the fluid mixtures were not sufficiently stable and hence would not be suitable for the impingement tests. Therefore, it was deemed necessary to make use of a surfactant in order to improve the stability of these lower volume fraction mixtures before continuing with the dilution process and overall experimental investigation.

Using an AS 220.R2 analytical balance (RADWAG, Poland), with built-in accuracy of ±0.005 g, sodium dodecyl sulphate (SDS), procured from Sigma-Aldrich (USA), was measured to produce a dispersion factor of 0.8. Once adding the SDS to a batch of fluid, it was subjected to magnetic stirring for a duration of 15 minutes. This process was conducted using a hotplate stirrer (Lasec, South Africa) with a heat and stir speed setting of 0 and 6 respectively. Following the addition and magnetic stirring of the surfactant into the appropriate batch of nanofluid, the sonication and fluid preparation process was continued.

Figure 4.1 portrays the initial visual stability of the prepared TiO_2-water nanofluid at a volume fraction of 0.25% with and without the addition of SDS.

Figure 4.1. Initial appearance of prepared TiO_2-water nanofluid samples at 0.25% volume fraction with (left) and without (right) the addition of SDS

Figure 4.1 indicates that the prepared sample containing SDS appears to be much more uniform in appearance than that of the sample that is free of any surfactant. Regarding the occurrence of sedimentation, the sample without surfactant shows a heavy presence of particle sedimentation on the bottom of its specimen container, while the other sample shows no sign of sedimentation. Ultimately, it can be concluded that the use of SDS resulted in enhanced stability among lower particle volume concentrations of TiO_2-water nanofluid and hence should be used in the preparation of TiO_2-water nanofluid mixtures below a volume fraction of 0.5%.

4.3. Thermophysical properties

4.3.1. Viscosity

The viscosity of the different nanofluid samples was measured using an SV-10 Sine Wave Vibro-viscometer (A&D, Japan) with an accuracy of 1% over its full range. Before initiating nanofluid measurements, the viscometer was calibrated according to the method outlined by the manufacturer in the associated user manual. The calibration process used DI-water and was conducted for a temperature range of 15 to 45 ℃, whereby viscosity readings were taken at intervals of 5 ℃.

Following the completion of the calibration process, each of the six nanofluid samples was subjected to a similar process and the measured viscosity values at each temperature interval were plotted against that of the DI-water. Figure 4.1 depicts the resulting viscosity values of the samples in comparison with those of the initial DI-water measurements.

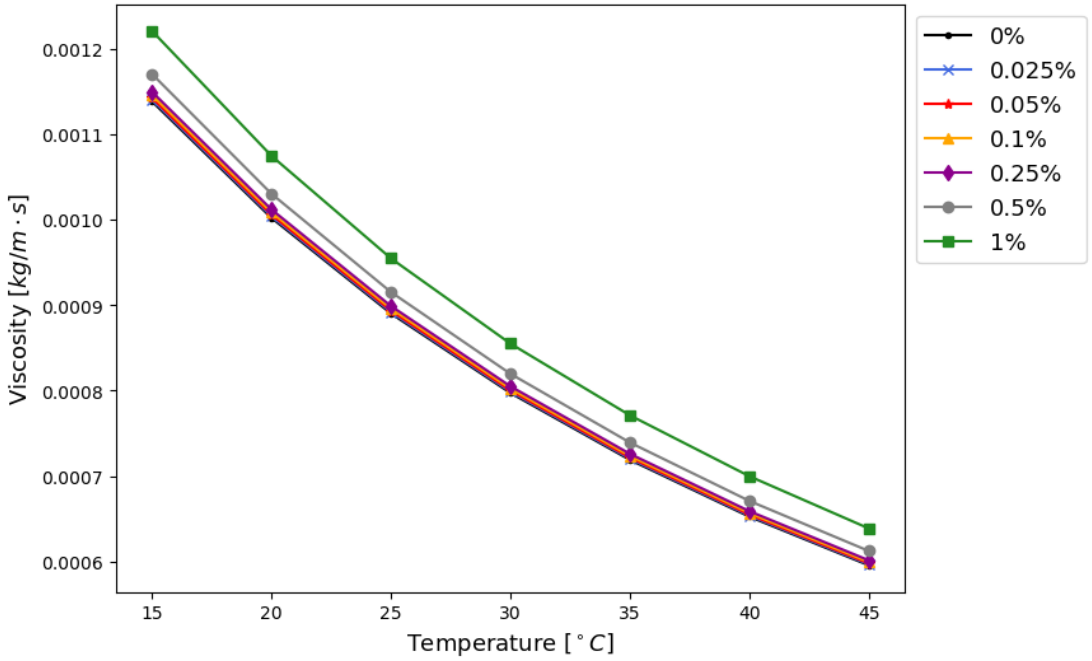

Figure 4.2. Viscosity of TiO_2-water as a function of temperature for varying particle volume fractions

Upon analysing the graph, it is clear that the magnitude of the measured nanofluid viscosity is proportional to its volume fraction. Similar to the case with the base fluid, the measured viscosity of the different samples deteriorated as temperature increased. This trend in viscosity is in line with the observations recorded by many different research groups, some of which are discussed in the review paper of Meyer et al. [10].

For comparison purposes, the experimental viscosity data was compared with the theoretical predictions obtained by means of the Brinkman model and those proposed by Wang et al. [129]. These models are expressed by equation 4.3 and 4.4 respectively as follows:

$$\mu_{nf} = \mu_{bf}(1-\varphi)^{-2.5} \tag{4.3}$$

$$\mu_{nf} = \mu_{bf}(1+7.3\varphi+123\varphi^2) \tag{4.4}$$

Making use of these models, the following figure was generated for the considered particle volume fraction range at a constant temperature of 25 ℃:

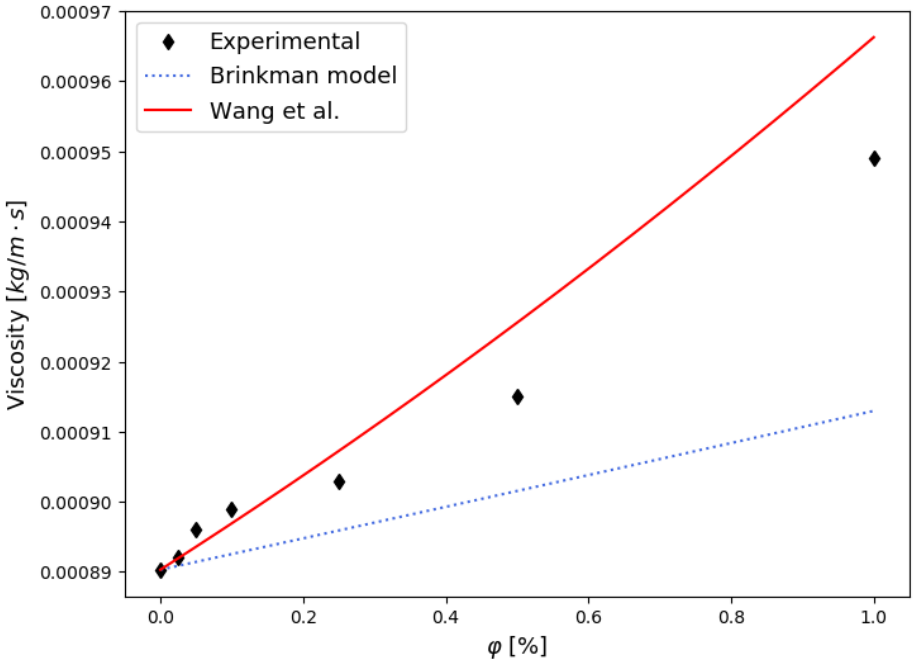

Figure 4.3. Experimental and predicted viscosity values for TiO_2-water nanofluid at varying particle volume fractions and a constant temperature of 25 ℃

According to figure 4.3, the Brinkman model was not suitable for predicting the viscosity data of the prepared volume fraction range of TiO_2-water nanofluid. The reason is that Brinkman's model is merely an adjustment of Einstein's model for a larger particle fraction range and hence does not account for all parameters influencing nanofluid viscosity. Therefore, this particular model underpredicted the fluid viscosity substantially.

The viscosity model proposed by Wang et al. [129] closely approximated the viscosity data for volume fractions less than 0.2%; however, it deviated as the fraction increased. When approximating the relative error between the data and model, it was found that the maximum deviation was less than 2%, which indicated that the experimental data was suitable for defining the viscosity of the appropriate nanofluid samples.

4.3.2. Thermal conductivity

As highlighted in Section 2.5.4, there are a wide range of models for predicting the thermal conductivity of a nanofluid. Unfortunately, no two models are the same nor do they take into account all of the different parameters that may influence the thermal conductivity of the fluid. As a result, most models are still limited in their accuracy and their suitability for real-life industrial applications.

Therefore, the experimental model of He et al. [130], which was specifically formulated for predicting the thermal conductivity of TiO_2-water nanofluids, was used for the approximation of the thermal conductivity of the different nanofluids in this study. Their proposed correlation is presented as follows:

$$k_{nf} = k_{bf}(125.62\varphi^2 + 4.82\varphi + 1) \tag{4.5}$$

By means of equation 4.5, the following plots were generated for varying particle concentrations of TiO_2-water at varying temperature values:

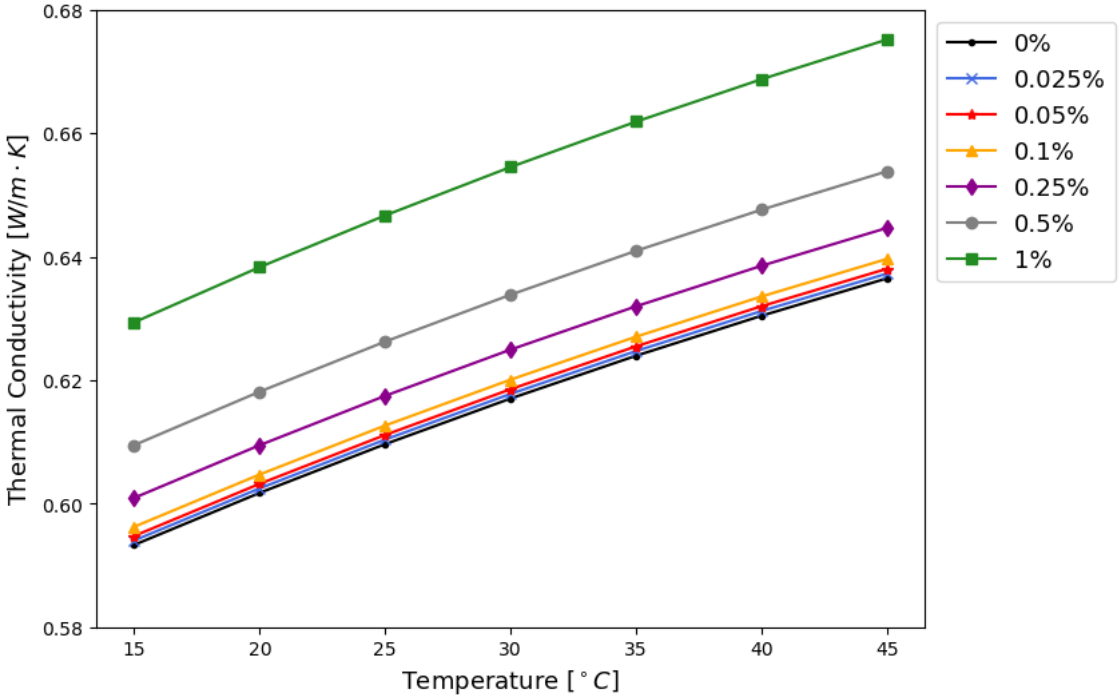

Figure 4.4. Approximated thermal conductivity of TiO_2-water as a function of temperature for varying particle volume fractions

Based on the above data, it is clear that the thermal conductivity of TiO_2-water is directly related to the fluid temperature and the particle fraction of TiO_2 nanoparticles suspended within the base fluid. Both parameters showed a direct correlation to the magnitude of the fluid's thermal conductivity and corresponded to the reported observations of the many researchers that have investigated the thermal conductivity behaviour of different nanofluids.

4.3.3. Other properties

Concerning the approximation of density for the different volume fractions of TiO_2-water, the mixing theory used by both Cheremisinoff [36] and Pak and Cho [37] was used. This expression is defined as follows:

$$\rho_{nf} = (1 - \varphi)\rho_{bf} + \varphi\rho_{np} \tag{4.6}$$

In predicting the specific heat of the different fluids, equation 2.7, which used the mixing theory and the assumption of thermal equilibrium between the particles and base fluid, was redefined as follows:

$$c_{p_{nf}} = \frac{\varphi c_{p_{np}}\rho_{np} + (1 - \varphi)c_{p_{bf}}\rho_{bf}}{\rho_{nf}} \tag{4.7}$$

Figures 4.4 and 4.5 visually illustrate the resulting density and specific heat values for the varying particle concentrations of TiO_2-water nanofluids in relation to temperature, obtained through the use of equation 4.6 and 4.7 respectively.

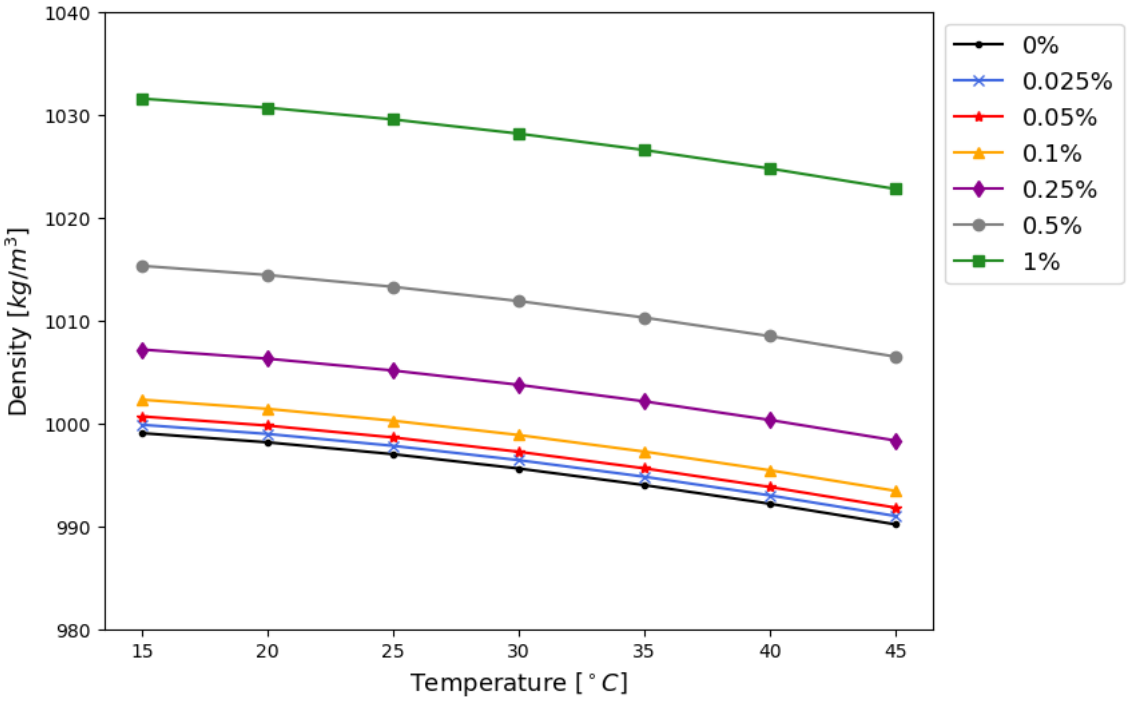

Figure 4.5. Approximated density of TiO_2-water as a function of temperature for varying particle volume fractions

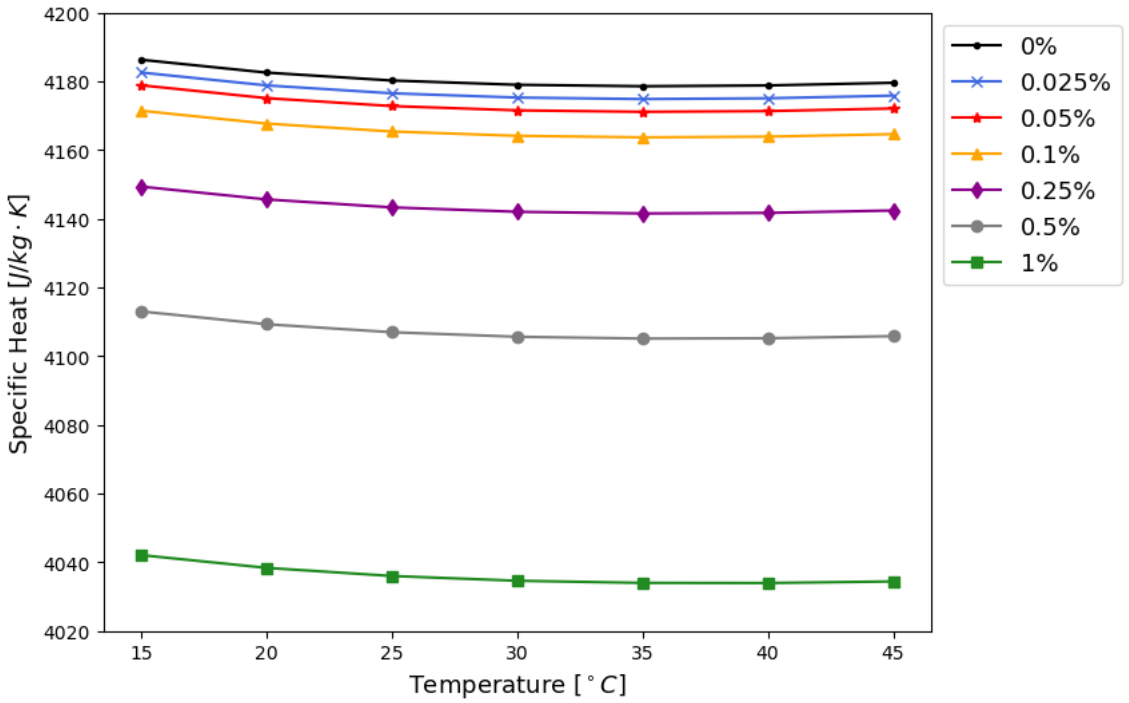

Figure 4.6. Approximated specific heat of TiO_2-water as a function of temperature for varying particle volume fractions

As depicted in Figure 4.6, the density of the prepared nanofluids was directly proportional to the particle volume fraction and inversely proportional to the overall fluid temperature. With respect to the predicted values for specific heat, an inverse relationship existed for the particle volume fraction, while no real trends were shown for the considered temperature range.

4.4. Stability

With the intent of analysing nanofluid stability, two 50 ml specimen containers were collected for each of the prepared nanofluid samples. The containers were labelled with the relevant TiO_2 volume concentration and were subjected to a visual and constant viscosity versus time stability check. Both tests and the results are discussed in the following sections.

4.4.1. Visual stability

When analysing the visual stability of the different samples, the clear specimen containers housing the appropriate nanofluids were positioned in front of a backdrop and photographed at varying time intervals. A black background was used for contrasting purposes and to assist in the overall quality of the visual inspection. Once an initial photograph was captured, further pictures were taken at hourly intervals to monitor sedimentation levels within the different samples. For the stability requirements of this investigation, photographs were taken every hour for a period of four hours. This particular time was much greater than that spent on each experimental run and hence was deemed a suitable value to validate the initial fluid stability.

Figure 4.7 portrays the captured images of the six different samples at time=0 and time=4 hours. As depicted in the figure, no particle sedimentation occurred, and the visual appearance of the multiple samples remained unchanged over the full four-hour time period. Therefore, it was concluded that the prepared fluid samples were visually stable.

(a)

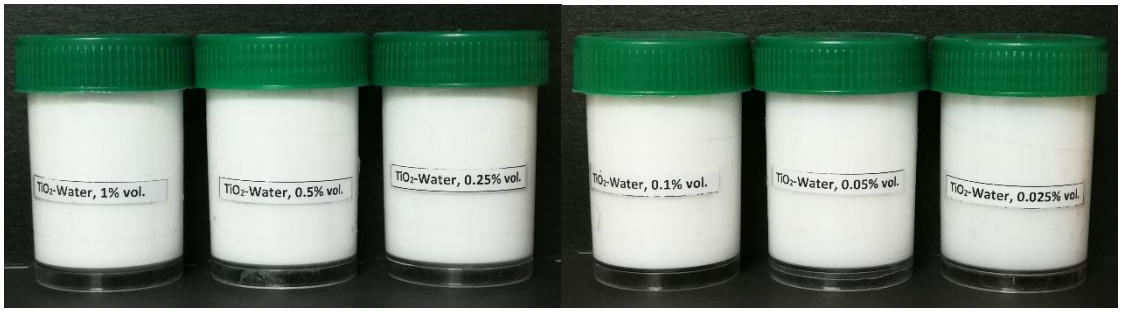

(b)

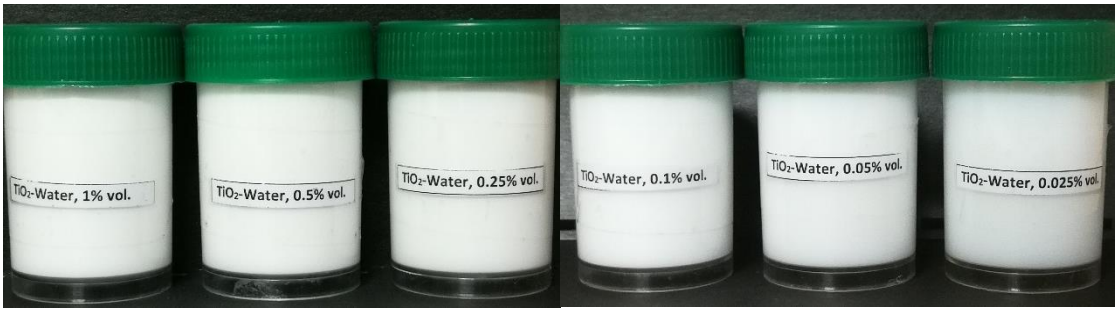

Figure 4.7. Visual stability analysis at (a) time=0 and (b) time=4 hours

4.4.2. Constant viscosity over time

In addition to visual appearance, the thermophysical properties of each fluid sample also had to demonstrate continuity before being deemed suitably stable.

Therefore, each fluid sample was subjected to a viscosity measurement at a constant temperature value for a predetermined period of time. Again, a period of four hours was used to quantify the fluid stability, while the fluid temperature was maintained at a temperature of 25 ℃. Using the SV-10 Sine Wave Vibro-viscometer (A&D, Japan), viscosity measurements were taken every 15 minutes for the full four-hour period.

Figure 4.8 depicts the resulting measurements of the respective fluid samples at each recorded time interval. This figure indicates that the measured viscosity values remained constant with respect to time for the full duration of the considered period. As a result of the continuity in the thermophysical measurement, each fluid sample was regarded as stable and hence could be used in the appropriate jet-impingement cooling tests.

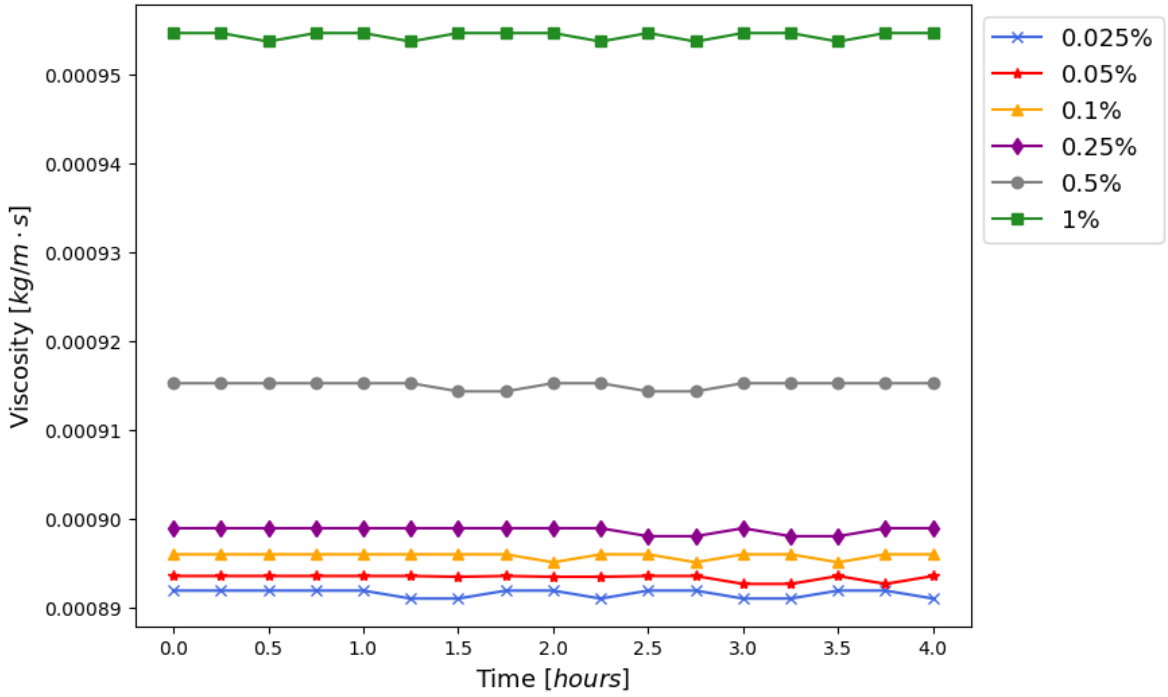

Figure 4.8. Viscosity of TiO_2-water as a function of time for varying particle volume fractions at T=25 ℃

4.5. Nanoparticle size

Based on the information provided by US Research Nanomaterials Inc (USA), the average particle size of the TiO_2 nanoparticles was specified to be within the range of 5 to 30 nm. In order to corroborate this information, a transmission electron microscopy (TEM) analysis of one of the nanofluid samples was conducted. Although this particular technique involves, unfavourably, drying out the sample, it is a common practice reported on in literature and is deemed a suitable method to better understand the morphology of a nanofluid [8].

Figures 4.9 (a) and (b) present the results of the TEM analysis for the coarse- and fine-scale of 200 and 50 nm respectively.

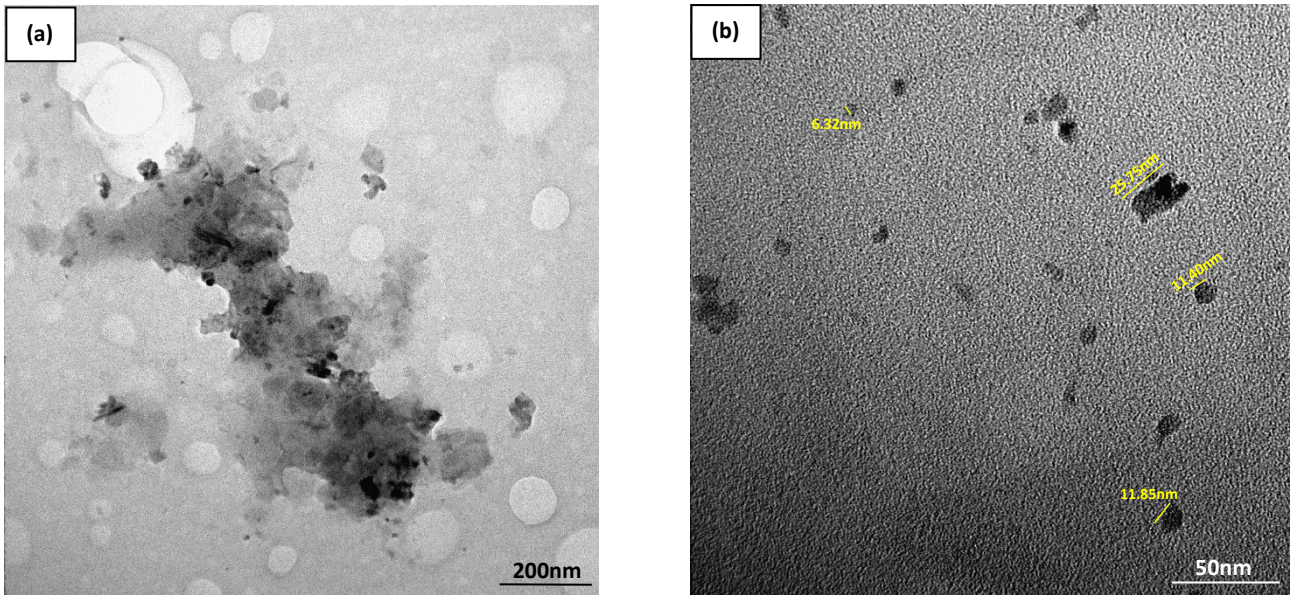

Figure 4.9. TEM analysis results (a) 200nm scale and (b) 50nm scale

The above figures indicate that the average size of TiO_2 nanoparticles fell approximately within the range of 5 to 30nm. Therefore, the figures confirm the information provided by the manufacturer.

However, for a more improved approximation of the TiO_2 nanoparticle size, it is recommended that a Zetasizer be used in conjunction with the TEM analysis. The use of such a tool would also enable one to determine the average particle size as a function of sonication time or even sonication energy input [131].

4.6. Summary and conclusions

This chapter described the preparation, thermophysical characterisation and overall stability analysis of the prepared TiO_2-water nanofluids. As mentioned earlier, only the viscosity of the resulting fluid samples was physically measured, while already existing models were used to approximate density, specific heat and thermal conductivity. To evaluate the stability of the multiple samples, a visual and constant viscosity versus time inspection was conducted.

When considering the viscosity measurements obtained via an SV-10 Sine Wave Vibro-viscometer, it was clear that the viscosity of the prepared nanofluid was directly related to the particle volume concentration and inversely related to its overall temperature. This trend was found to coincide with those already reported on in other related nanofluid studies.

With respect to the approximation of thermal conductivity, the model of He et al. [130], which was specifically formulated for predicting the thermal conductivity of TiO_2-water nanofluids, was used. Based on the nature of this particular model, it was concluded that the fluid's thermal conductivity would be impacted by the particle concentration and overall fluid temperature. However, unlike viscosity, the thermal conductivity would be directly proportional to temperature. Yet again, such behaviour was found to be consistent with that of published works.

Based on the overall duration of the respective cooling tests, it was determined that a minimum stability period of four hours would be suitable to deem a prepared fluid sample "stable". Using the visual and constant

viscosity versus time checks, all nanofluid samples were found to be of suitable stability for the experimental investigation.

Lastly, in an attempt to understand the particle morphology and verify the average nanoparticle size specified by the manufacturer, a TEM analysis was also conducted. Based on the results of the analysis, the information provided by the manufacturer was found to be valid.

5. Results

5.1. Introduction

This chapter describes the validation and the conducted energy balance of the current experimental model. In addition to the validation, the resulting heat transfer data for the various jet impingement tests using the TiO_2-water particle concentrations is also presented and discussed. With reference to the steady-state impingement tests, a correlation fitted to the experimental data is also portrayed and evaluated in this section of the study.

5.2. Validation of the experimental model

Before conducting any jet-impingement cooling tests, using the prepared volume fractions of nanofluid, initial experimental calibration and validation were done using DI-water. The process was conducted to ensure that the physical system behaved as expected and that the heat transfer data obtained through the respective impingement tests was both valid and could be used with confidence. In order to prove that the jet-impingement cooling tests provided valid results, the average steady-state Nusselt numbers obtained for the DI-water tests were compared with already existing correlations for free-surface water jet impingement.

Yaohua et al. [132] conducted numerical and experimental investigations to characterise the conjugate heat transfer coefficient on a copper target surface impinged on normally by a free-surface circular jet. Regarding the considered parameters, nozzle diameter was varied between 0.9 and 2.0 mm and Reynolds numbers were within the range of 8 000 to 25 000. The diameter of the copper target surface was reported to be 10 mm.

The correlation fitted to the experimental data for the Nusselt numbers of their appropriate water tests is as follows:

$$Nu = 0.7212\left(\frac{2d}{D}\right)^{2} Pr^{0.4} Re^{0.5} + 0.89\left(\frac{2d}{D}\right)^{2}\left[\left(\frac{D}{2d}\right)^{3/2} - 1\right] Pr^{1/3} Re^{0.5} \tag{5.1}$$

Based on the considered conditions reported above, the above expression regressed as follows:

$$Nu = 0.9454 Pr^{1/3} Re^{0.43} \tag{5.2}$$

Figure 5.1 shows the comparison of the matched curves of equations 5.1 and 5.2 with the experimental values of the DI-water tests.

Figure 5.1 indicates that equation 5.2 overpredicted the Nusselt number substantially showing an absolute error ranging between 35 and 85%. With respect to equation 5.1, the predicted Nusselt numbers showed a good agreement with the experimental data at higher Reynolds numbers but deviated as the Reynolds number was decreased below 20 000. When calculating the absolute error between the curve of equation 5.1 and the measured data, it was found to be within the range of 0.5 to 25%.

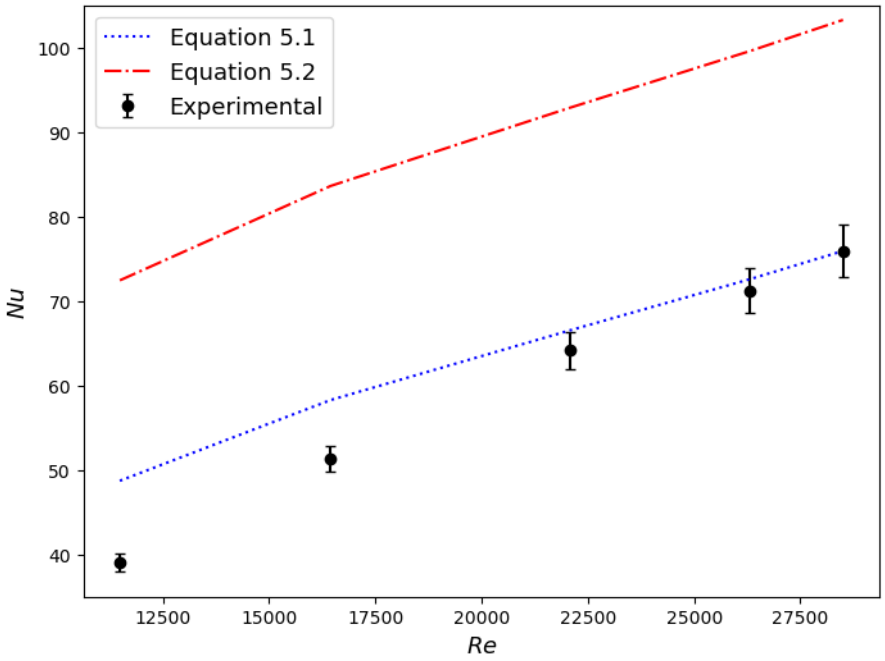

Figure 5.1. Comparison between the experimental and calculated Nusselt numbers for steady-state DI-water jet impingement

In comparing the accuracy of the two correlations with that of the measured data, it should be noted that equation 5.2 was simplified for a particular experimental condition and hence did not take into account the ratio of the nozzle and surface diameter used in this study. As a result, the expected error associated with the correlation would be large. Regarding the error for equation 5.1, although the previously mentioned diameter ratio was considered, the model did not account for other parameters such as nozzle-to-target surface distance that could influence the resulting Nusselt number and thus was also limited in its accuracy.

Regardless of the error between the experimental data and the theoretical correlations, similar trends were indicated with an increase in Reynolds number. Furthermore, despite the slight error at Reynolds numbers < 20 000, the experimental data was closely approximated by equation 5.1 and thus could be deemed valid.

In conjunction with the validation study described above, the experimental system was also validated through an energy balance between the heated target surface, the HTF (water) and the electrical power input. This particular validation, based on equations 3.18 and 3.19, served as an indicator of the physics of the experimental model and was conducted to ensure that all energy losses were as low as possible to prevent any adverse effects on the measured data.

Table 5.1 presents the average energy balance between the copper specimen and the HTF, as well as that between the copper specimen and the electrical power input for the considered Reynolds numbers of the respective water impingement tests.

Table 5.1. Average energy balances for steady-state water jet impingement tests

Tested Reynolds number	**11 486**	**16 449**	**22 075**	**26 318**	**28 503**
Average energy balance between copper specimen and water	2.18%	3.51%	3.09%	3.21%	2.31%
Average energy balance between electrical power input and copper specimen	2.27%	3.28%	2.67%	2.35%	5.26%

As shown in Table 5.1, the average energy balance between the heat transfer of the copper specimen and the impingement fluid (water) was less than 4% across the entire range of tested Reynolds numbers, while that of the specimen and electrical power input was within the range of 2.27% to 5.26%. Based on these energy balances, it could be concluded that the system was valid in its operation and that the effects of energy losses on the experimental data would be negligible.

5.3. Steady-state jet impingement of TiO_2-water nanofluids

5.3.1. Average convective heat transfer coefficients

Figure 5.2 plots the average HTC against the different Reynolds numbers for the varying volume particle concentrations of TiO_2-water. The figure indicates that the resulting convective HTC for the different fluid tests was directly proportional to the Reynolds number and increased in a near-linear manner. This behaviour is commonly observed in jet impingement studies and is described as a direct consequence of an increasing convection effect under higher fluid flow rates.

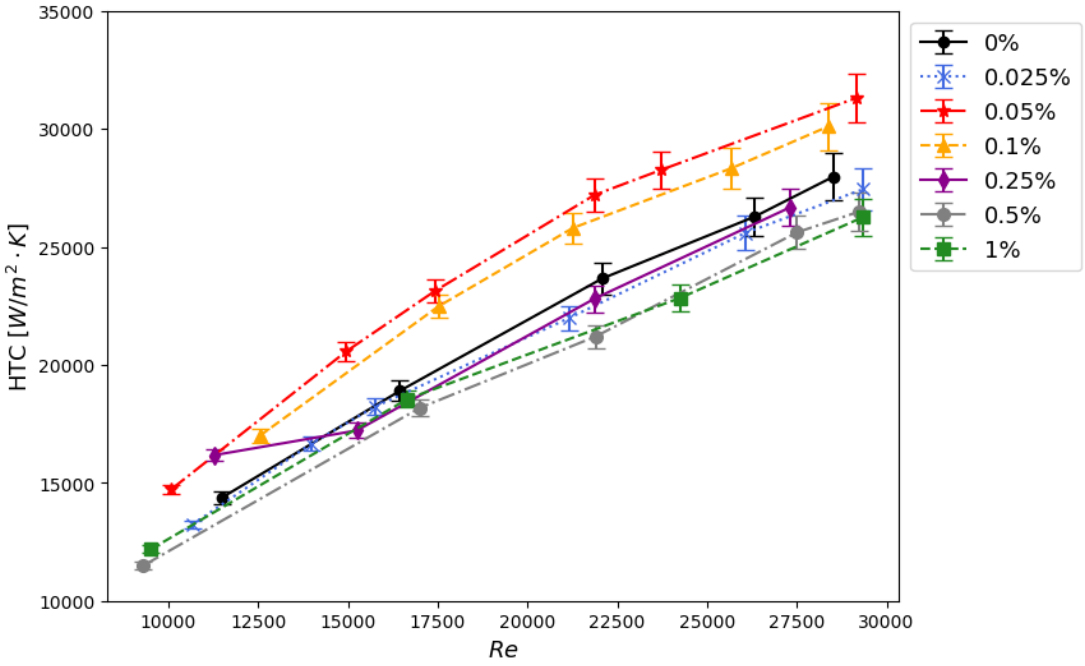

Figure 5.2. Average HTC values for varying volume fractions of TiO_2-water at varying Reynolds numbers

In terms of the effect of nanoparticle concentration on the average steady state HTC, it was found that the use of nanofluids produced adverse effects. As seen in Figure 5.2, the use of TiO_2-water within the volume fraction range of 0.25 to 1% produced an unfavourable effect on the HTC when compared with using DI-water. As for the particle volume fractions of 0.1 and 0.05%, it was found that the average HTC was enhanced by an average of approximately 10 and 14% respectively. However, when decreasing the particle volume concentration to 0.025%, the average HTC was again less favourable than for DI-water. As a result, the optimum volume fraction of TiO_2 particles was found to be 0.05%.

In an attempt to explain these observations, the works of Tie et al. [4], Jaberi et al. [107] were used. In both works, the authors report on the adverse effects encountered in jet-impingement cooling when using different particle concentrations of nanofluid. According to their works, the convective HTC is directly dependent on the fluid thermal conductivity and inversely on the boundary layer thickness. Although the thermal

conductivity of nanofluids increases with particle concentration, the viscosity of the fluid also increases, which, in turn, causes an increase in the boundary layer thickness. Therefore, at higher particle concentrations, the effect of the increase in viscosity on the HTC may overcome the effect of the increase in the thermal conductivity and thus decrease the contribution of the thermal conductivity to the overall HTC. Tie et al. [4] explain that the enhancement in fluid thermal conductivity exceeds the enhancement of the HTC during such an occurrence.

Based on the above explanation, it could be concluded that the thermal conductivity enhancement achieved at a volume fraction of 0.05 and 0.1% produced a positive effect on the HTC. Increasing the volume fraction beyond this range resulted in the thermal conductivity enhancement exceeding the enhancement in HTC (the increase in fluid viscosity and boundary layer thickness outweighed the increase in fluid thermal conductivity). In explaining the performance of the 0.025% volume concentration, it could be deduced that the enhancement offered in thermal conductivity was simply not large enough to offer any improvement in the heat transfer of the jet cooling process.

5.3.2. Average Nusselt numbers

The overall heat transfer performance of the various nanofluid concentrations is presented in non-dimensional form in Figure 5.3.

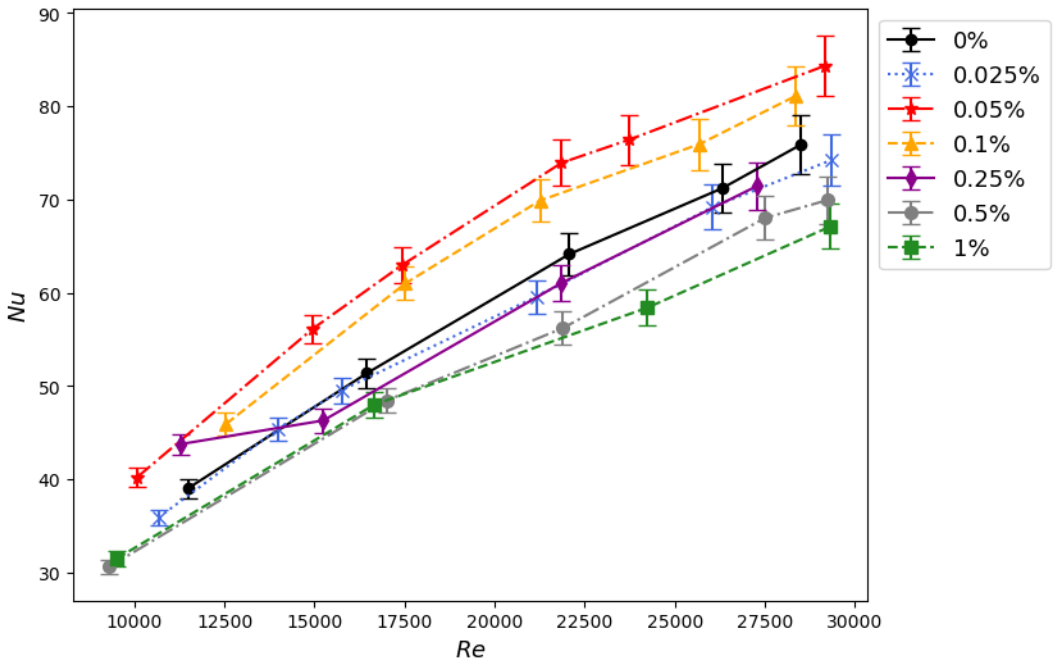

Figure 5.3. Average Nusselt number values or varying volume fractions of TiO_2-water at varying Reynolds numbers

Similar to the data of the HTC, Figure 5.3 illustrates adverse effects on the Nusselt number when using varying particle concentrations of TiO_2-water nanofluid. The overall enhancement showed that a volume fraction of 0.05% produced a maximum average enhancement of 14.75%, while a volume fraction of 1% produced the most adverse effect on the Nusselt number by reducing the value by an average of 13.05%.

With respect to the general trends observed in the data, it can be noted that the Nusselt number of all fluid concentrations increased with an increase in Reynolds number due to the forced convection effect, but only volume fractions of 0.05 and 0.1% were capable of producing an overall enhancement in comparison with the impingement of DI-water. As stated earlier, this behaviour may be associated with the trade-off between

thermal conductivity enhancement and the increase in fluid viscosity and boundary layer thickness due to an increase in particle volume concentration.

5.3.3. Correlation of the results

Based on the experimental measurements of the varying particle volume fractions of TiO_2-water nanofluid, a correlation was formulated using regression software to predict the Nusselt number as a function of the fluid volume fraction and Reynolds number. The correlation is presented as follows:

$$Nu = \begin{cases} 0.1263 \cdot Re^{0.705}\varphi^{0.235}, & \varphi < 0.1\% \\ 0.0669 \cdot Re^{0.67}\varphi^{-0.1}, & \varphi \geq 0.1\% \end{cases} \quad (5.3)$$

where R^2 is 0.98%.

Figure 5.4 portrays the fitted lines of equation 5.3 to the experimentally measured Nusselt numbers of each particle volume fraction of TiO_2-water.

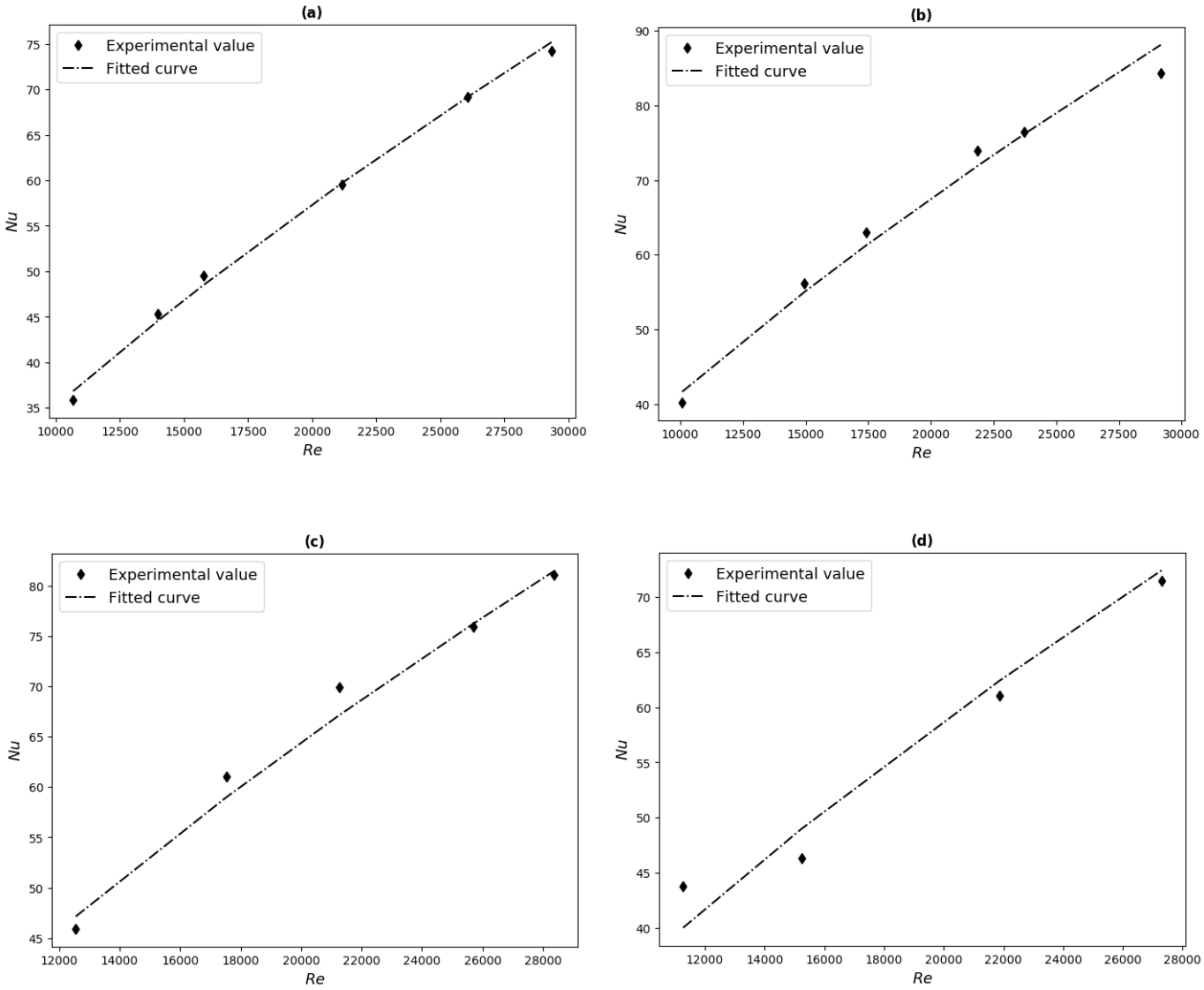

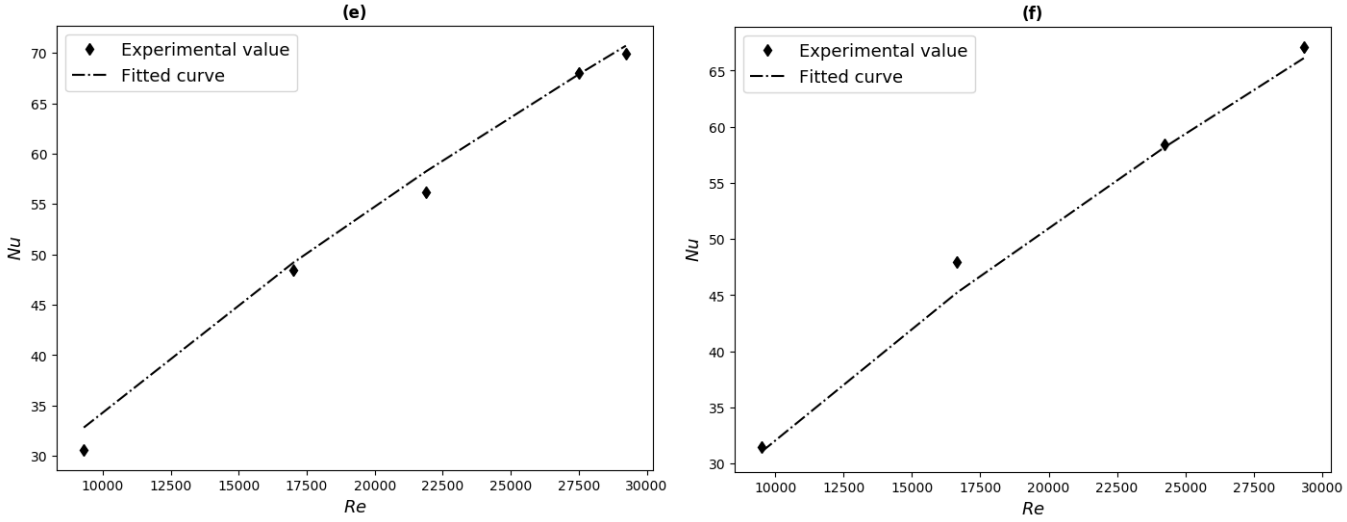

Figure 5.4. Comparison between the calculated and experimental Nusselt numbers for varying volume fractions of TiO_2-water: (a) 0.025 Vol. %, (b) 0.05 Vol. %, (c) 0.1 Vol. %, (d) 0.25 Vol. %, (e) 0.5 Vol. % and (f) 1 vol. %

As shown by the sub-plots, the proposed correlation showed a good agreement with the experimentally measured data and predicted the Nusselt numbers for a particular volume fraction at the various Reynolds numbers very closely. To quantitatively compare the predicted data of equation 5.3 and that measured experimentally, Figure 5.5 was generated below.

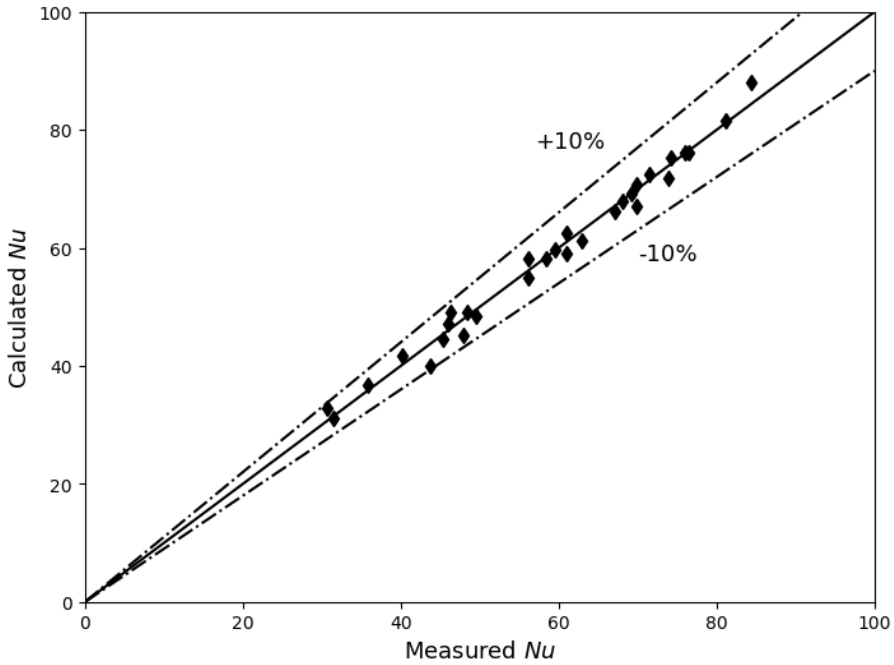

Figure 5.5. Comparison between the calculated and the experimental Nusselt numbers

Figure 5.5 shows that equation 5.3 predicted the experimentally measured Nusselt number within an error range of less than 10%. Therefore, it is proved that the proposed correlation is capable of accurately predicting the non-dimensional HTC of TiO_2-water nanofluid for free-surface single jet impingement with a circular jet nozzle.

5.4. Transient jet impingement of TiO_2-water nanofluids

As highlighted in Chapter 3, the time-sensitive nature of the transient cooling impingement tests did not provide ample time for flow rate stabilisation and as a result, only the maximum pump flow rate could be considered. Subsequently, the cooling curves of the different nanofluid concentrations were compared at the same volume flow rate of approximately 2 L/min.

To eliminate the influence of the jet inlet temperature on the cooling curves, the surface temperature data as opposed to time data was non-dimensionalised according to the method outlined in Section 3.4.2. Figure 5.6 illustrates the resulting transient curves for the varying volume fractions of TiO_2-water.

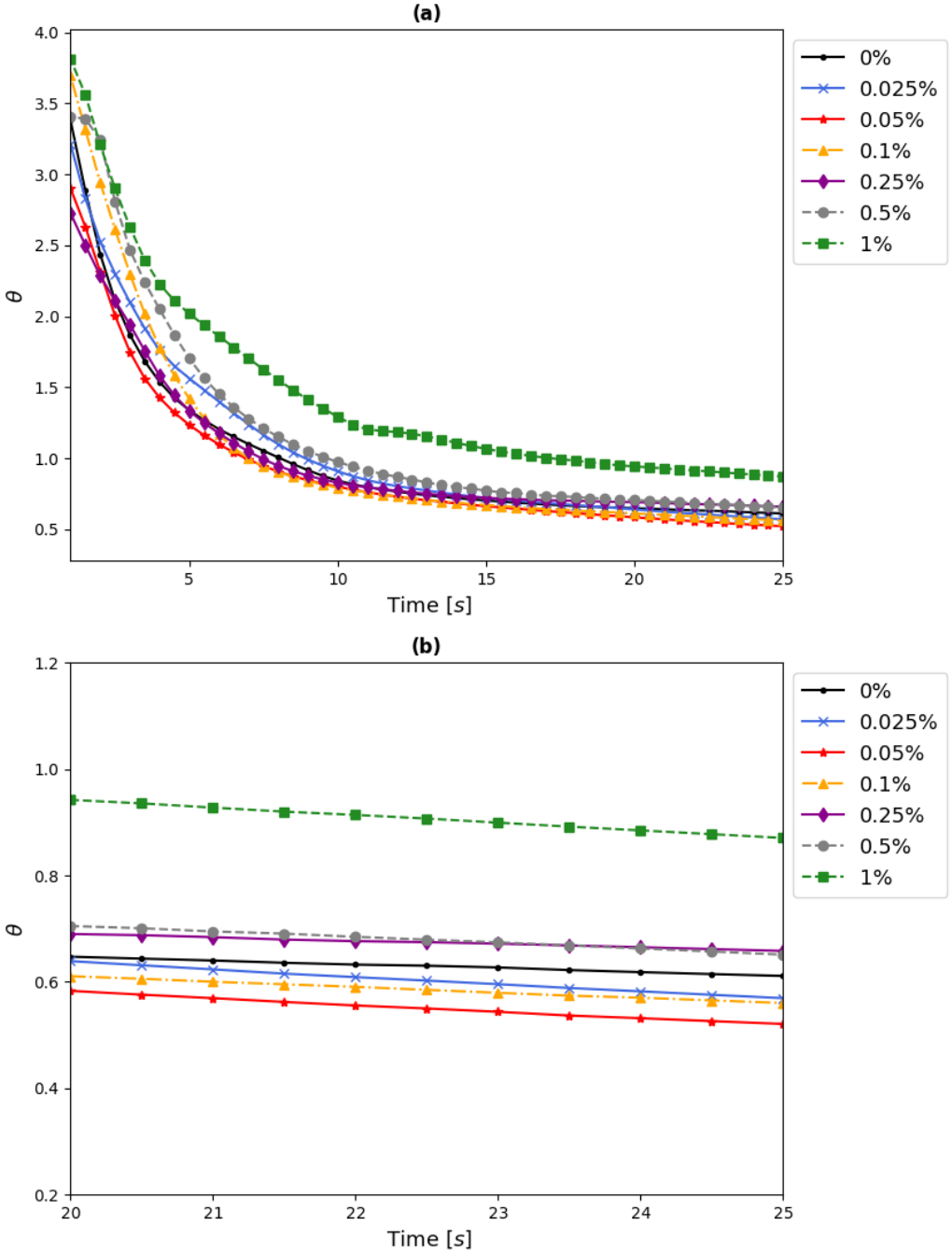

Figure 5.6. Non-dimensionalised cooling curves for varying particle volume fractions of TiO_2-water with respect to time: (a) overall cooling curve and (b) zoomed-in portion for time=20 to time=25 seconds

Figure 5.6 indicates that the transient behaviour of the TiO_2-water nanofluids exhibited similar behaviour to that of the steady-state cooling tests. As was the case in Section 5.3, the higher particle volume fraction range of 0.25 to 1% produced adverse effects on the cooling efficiency when compared with DI-water at a similar volume flow rate. Concerning particle fractions ≤ 0.1%, the opposite effect was observed, and cooling efficiency was improved.

By means of transient cooling with volume fractions of 0.025, 0.05 and 0.1%, the non-dimensional cooling efficiency was observed to improve by approximately 6, 16 and 8% respectively. Consequently, it was concluded that the maximum enhancement was obtained when using a 0.05% volume fraction of TiO_2-water.

When comparing the data above with that of similar transient works, presented in Table 2.15 of the literature review, it was found that cooling efficiency generally increased in relation to the nanoparticle concentration in the base fluid. In addition to the increased particle concentration resulting in the enhancement of the fluid's thermal conductivity, Barewar et al. [133] provide the following reasons for the enhancement in cooling efficiency:

- An increased particle concentration results in increased particle deposition along the target surface, which forms a thin layer and improves the surface wettability (this assists in enhancing the heat transfer rate).
- Higher particle concentrations result in an increased surface area and heat capacity of the nanofluid.
- By increasing the concentration of nanoparticles, there is an increase in the random motion of the particles, which increases turbulence intensity and thus improves the contribution of convective heat transfer (Brownian motion effect).

However, Figure 5.6 indicates that the transient data of the current study did not show the reported trends. A plausible explanation could be that the thermal conductivity enhancement obtained through an increased particle concentration was overcome by the increase in fluid viscosity, thus inhibiting the heat transfer coefficient of the cooling process. In addition, despite an increased particle concentration resulting in particle deposition assisting in heat transfer between the fluid and target surface, Sarkar et al. [121] warn that a very large particle concentration may result in too large a degree of deposition along the target surface and thus may act as a hindrance to heat transfer between the coolant and the test specimen. Because TiO_2 had a much lower thermal conductivity than the copper target surface, the deposition layer could have caused the observed trends at volume fractions greater than 0.1%.

Furthermore, the transient tests were not conducted for identical Reynolds numbers, but rather for volume flow rates. Subsequently, the deviation in tested Reynolds numbers could cause the observed trends in Figure 5.6.

5.5. Summary and conclusions

This chapter defined the initial validation of the experimental model and presented and discussed the resulting data for both the steady-state and transient jet-impingement cooling tests.

The experimental data for DI-water was used to validate the experimental model by means of comparison with the theoretical correlations proposed by Yaohua et al. [132]. Based on the resulting data, it was found that similar trends were shown when using the appropriate correlations and that a good agreement between the experimental data and predicted values existed. Therefore, the results were deemed valid. Through an energy balance for each tested Reynolds number, the energy losses in the system were also shown to be low and hence negligible to the overall experimental data.

The data resulting from the steady-state tests showed that the use of TiO_2-water nanofluid in jet-impingement cooling produced adverse effects on the overall heat transfer performance. Within the experimental parameters considered, a maximum Nusselt number enhancement of 14.75% was obtained at a particle concentration of 0.05%. At particle concentrations greater than 0.1%, the heat transfer capabilities of impingement cooling were reduced when compared with the capabilities of the tested DI-water. This behaviour was justified by the trade-off between thermal conductivity and viscosity of the nanofluid, which both increased in direct proportion to the particle volume fraction. With reference to the effect of Reynolds number on the resulting heating transfer performance, it was observed that both the HTC and Nusselt number increased with an increase in Reynolds number. This behaviour was found to coincide with other works and was a direct result of the forced convection effect.

To predict the resulting Nusselt numbers of free-surface circular jet-impingement cooling by means of TiO_2-water nanofluid, a power correlation was fitted to the appropriate experimental data. The correlation was a function of volume fraction and Reynolds number and was found to be capable of predicting the experimental data within an error range of less than 10%.

Concerning the transient tests conducted for various nanofluid mixtures, it was found that only volume fractions ≤ 0.1% produced improvement in the cooling efficiency. Of the three volume fractions of 0.025, 0.05 and 0.1%, a maximum enhancement of 16% was observed for the 0.05% volume mixture. The trends depicted in these tests appeared to be unusual when compared with previous transient studies; however, they could be explained through increased particle deposition along the target surface and the over-enhancement of fluid viscosity in relation to the thermal conductivity of nanofluids at higher particle concentrations.

6. Conclusions and recommendations

6.1. Conclusions

The study experimentally investigated the potential heat transfer enhancement of free-surface jet impingement by means of varying volume fractions of TiO_2-water for both steady-state and transient cooling applications.

Before commencing the pertinent investigation, a comprehensive literature review on the nature of nanofluids and jet impingement heat transfer was conducted. Based on this study, the structure and thermophysical behaviour of nanofluids were examined with particular focus on the preparation, modelling and stability techniques associated with such fluids. Regarding jet impingement, the general physics and experimental techniques of the heat transfer mechanism were defined. Additionally, the study also summarised the many reported publications relating to jet impingement through the use of nanofluids in both the steady and transient state.

Upon completion of the literature review, an experimental rig was designed and manufactured to conduct the appropriate jet-impingement cooling tests. The system consisted of a free-surface circular jet nozzle, which was positioned above a copper cylinder target surface with a PTFE insulation housing. The target surface was to be heated using cartridge heaters and cooled by water and nanofluid of varying particle concentrations, using a centrifugal pump. Based on the summarised works of the literature review, a nanofluid of TiO_2-water was selected.

Before commencing the respective jet impingement tests, the six volume fractions of TiO_2-water ranging between 0.025 and 1% were prepared and characterised in terms of their thermophysical properties, stability and particle morphology. The preparation technique used was a single-step dilution process in conjunction with sonication to break down particle agglomeration. For lower particle fractions, a surfactant of SDS was used to improve stability and was mixed into the appropriate samples by a magnetic stirrer. The thermophysical properties for density, specific heat and thermal conductivity were all approximated using theoretical models, while the properties of viscosity were determined by physical measurements. In terms of the stability of the different samples, all samples were visually stable and had continuity in their thermophysical properties with respect to time. Through the use of TEM analysis, the particle morphology specified by the manufacturer was also proved to be valid.

Prior to testing the prepared nanofluid samples, base case tests of water were done for validation and comparative purposes. Through the use of existing correlations and an energy balance of heat transfer in the system, the experimental model was concluded to be valid and thus the data obtained through testing could be used with confidence.

The steady-state jet impingement tests were conducted at a constant heat flux where an electrical power input of 145 watt was applied across the cartridge heaters. During the multiple runs with different nanofluid volume fractions, flow rates were adjusted to produce Reynolds numbers within the range of approximately 10 000 to 30 000. Analysis of the resulting steady state heat transfer data (HTC and Nusselt numbers) showed that the use of TiO_2-water nanofluids produced adverse effects on the overall heat transfer performance of the system. Within the experimental parameters considered, a maximum Nusselt number enhancement of 14.75% was obtained at a particle concentration of 0.05%. At particle concentrations greater than 0.1%, the heat transfer capabilities of impingement cooling were reduced when compared with the base tests for DI-water capabilities. This behaviour was justified by the trade-off between thermal conductivity and viscosity of the nanofluid, which both increased in direct proportion to the particle volume fraction. The impact of the

fluid Reynolds number on the resulting heat transfer performance was shown to possess a direct correlation in the sense that both the HTC and Nusselt number increased with an increase in Reynolds number. This trend was shown to coincide with other published works and was a direct result of the forced convection effect.

Using appropriate regression software, a power correlation was determined for predicting the resulting Nusselt numbers of the steady-state impingement tests. The resulting correlation which accounted for volume fraction and Reynolds number was shown to be capable of approximating the experimental Nusselt numbers for a free-surface circular jet impinging upon a target surface by means of TiO_2-water. The resulting accuracy of the correlation was shown to have an error range of less than 10%.

In an attempt to investigate the effects of particle concentration on the transient cooling of the jet system, cooling curves with respect to time were recorded for an initial surface temperature of approximately 105 ℃. Due to the time-sensitive nature of the tests, sufficient time for fluid flow stabilisation was not available and tests were completed at a maximum pumping power. To eliminate the effects of inlet jet temperature, these curves were non-dimensionalised and plotted on the same axes for comparative purposes. Of the volume fractions considered, it was found that only ≤ 0.1% produced improvement in cooling efficiency, while those of higher concentrations showed unfavourable results when compared with DI-water. Of the three particle fractions, 0.025, 0.05 and 0.1%, a maximum enhancement of 16% was observed for the 0.05% volume mixture. Despite the general trend in transient data appearing unusual when compared with previous studies, this behaviour could be explained by means of increased particle deposition along the target surface and the over enhancement of fluid viscosity in relation to the thermal conductivity of nanofluids at higher particle concentrations.

The reported findings of the concluded experimental tests showed that the use of TiO_2-water nanofluids in jet impingement applications could result in an enhancement of heat transfer performance depending on the particle concentration considered. For this particular study an optimum particle concentration of 0.05% was observed for both steady- and transient state jet-impingement cooling.

6.2. Recommendations

Recommendations based on this study are distinctively classified into recommendations for expanding on the completed work and for improving or modifying the current experimental system and its functioning. Each type of recommendation is explained in the following sections.

6.2.1. Recommendations for future works

The current study was conducted for jet-impingement cooling at a non-dimensionalised nozzle-to-target surface height of 4 and an impingement angle normal to the target surface. Therefore, it is recommended that the effects of nozzle height and impingement angle are considered for future works, especially with regard to the impingement cooling of nanofluids.

In addition to modifying the angle and nozzle height, it is also recommended that the geometry of the jet nozzle be varied. As highlighted in Section 2.6.1 of the literature review, slot jets provide higher cooling effectiveness, better controllability, uniformity and thus may be viewed as superior to circular jets. Therefore, it would be worth comparing the performance of nanofluid impingement on the current set-up for both a circular and a slot-shaped jet nozzle.

In more recently published works, some investigators such as Sun et al. [3] have shifted their focus to the jet impingement of nanofluids with induced swirl effects. By introducing swirl, flow speeds are rapidly increased while maintaining the nozzle mass flow rate and thus swirl is believed to improve jet impingement heat

transfer. Therefore, a possible suggestion for future works could be to investigate nanofluid jet impingement with induced swirl effects.

As the focus of the current study was on jet impingement by means of TiO_2-water nanofluid with varying particle concentrations, it is highly recommended that more tests are done with other nanofluid types and volume fractions. In addition to these tests, it may also be worth investigating the impingement behaviour of hybrid nanofluids (fluids consisting of more than one nanoparticle type) in comparison with single-particle colloids.

Regarding the nature of the tests conducted in this experimental investigation, it is suggested that the transient cooling tests be given more focus and that the pressurised air system, accommodated by the test rig, be used to propel the appropriate fluids. The time-sensitive nature of the tests did not allow for flow rate stabilisation at lower pump settings and thus the tests had to be done at a fixed volume flow rate. By using pressurised air, the transient cooling effects may be better tested as the fluid flow would be controlled by a constant pressure of 8 bar rather than that of the centrifugal pump (pressurised air may provide more consistent flow rates for the varying volume fractions of nanofluid).

Lastly, it is recommended that a numerical study also be conducted in addition to the experimental investigation for comparison purposes and extended research opportunities. Validating the results obtained numerically to that of the recorded experimental data will allow for the capturing of physical phenomena that are either not possible or difficult to measure by means of the current experimental model. Examples of such phenomena include, but are not limited to, nanoparticle size, surface size and geometry, fluid flow rates and flow patterns (out of the range offered by the pump) and turbulence intensities.

6.2.2. Recommendations relating to the experimental system

Regarding the improvement of the current experimental system, the following recommendations are made:

- Modify the location and accessibility of the cartridge heaters: The six cartridge heaters were located within the base of the copper specimen, which, in turn, was surrounded by a PTFE housing. Should a heater burn out and require replacement, the entire heated targeted surface will have to be disconnected and removed from the system. Such a process is not only time-consuming, but also involves the removal of other components such as the five internal thermocouples.
- Procure a pump with built variable speed control drive: Despite the solid-state relay system connected to the centrifugal pump, it is recommended to procure a pump that has a built-in control drive for easy and consistent control of the experimental fluid flow rates. Through improving fluid flow control, it will be possible to obtain an increased number of data points at specific fluid flow rates.

References

1. Ranga Babu, J.A., K.K. Kumar, and S. Srinivasa Rao, *State-of-art review on hybrid nanofluids.* Renewable and Sustainable Energy Reviews, 2017. **77**: p. 551-565.
2. Maxwell, J.C., *A Treatise on Electricity and Magnetism, Vol. 1, unabridged 3rd ed*. 1891, Clarendon Press, Oxford, UK.
3. Sun, B., et al., *Experimental study on heat transfer characteristics of hybrid nanofluid impinging jets.* Applied Thermal Engineering, 2019. **151**: p. 556-566.
4. Tie, P., Q. Li, and Y. Xuan, *Heat transfer performance of Cu–water nanofluids in the jet arrays impingement cooling system.* International Journal of Thermal Sciences, 2014. **77**: p. 199-205.
5. Sharifpur, M., J. Meyer, and S. Africa. *Opportunities in nanofluid composites*. in *Proceedings of the 3rd International Conference on Composites: Characterization, Fabrication and Application (CCFA-3), Tehran*. 2012.
6. Krajnik, P., F. Pusavec, and A. Rashid, *Nanofluids: properties, applications and sustainability aspects in materials processing technologies*, in *Advances in Sustainable Manufacturing*. 2011, Springer. p. 107-113.
7. Das, S.K., et al., *Nanofluids: science and technology*. 2007: John Wiley & Sons.
8. Ghodsinezhad, H., M. Sharifpur, and J.P. Meyer, *Experimental investigation on cavity flow natural convection of Al2O3–water nanofluids.* International Communications in Heat and Mass Transfer, 2016. **76**: p. 316-324.
9. Ghadimi, A., R. Saidur, and H. Metselaar, *A review of nanofluid stability properties and characterization in stationary conditions.* International journal of heat and mass transfer, 2011. **54**(17-18): p. 4051-4068.
10. Meyer, J.P., et al., *The Viscosity of Nanofluids: A Review of the Theoretical, Empirical, and Numerical Models.* Heat Transfer Engineering, 2016. **37**(5): p. 387-421.
11. Garbadeen, I., et al., *Experimental study on natural convection of MWCNT-water nanofluids in a square enclosure.* International Communications in Heat and Mass Transfer, 2017. **88**: p. 1-8.
12. Yu, W. and H. Xie, *A review on nanofluids: preparation, stability mechanisms, and applications.* Journal of nanomaterials, 2012. **2012**: p. 1.
13. Sharma, S. and S.M. Gupta, *Preparation and evaluation of stable nanofluids for heat transfer application: a review.* Experimental Thermal and Fluid Science, 2016. **79**: p. 202-212.
14. Wen, D. and Y. Ding, *Experimental investigation into the pool boiling heat transfer of aqueous based γ-alumina nanofluids.* Journal of Nanoparticle Research, 2005. **7**(2-3): p. 265-274.
15. Lee, S., et al., *Measuring thermal conductivity of fluids containing oxide nanoparticles.* Journal of Heat transfer, 1999. **121**(2): p. 280-289.
16. Ju, L., et al., *Aggregation kinetics of SDBS-dispersed carbon nanotubes in different aqueous suspensions.* Colloids and Surfaces A: Physicochemical and Engineering Aspects, 2012. **409**: p. 159-166.
17. Wang, X., L. Ma, and R. Lin, *Enthalpic interactions of N, N-dimethylformamide in aqueous glucose and sucrose solutions at 298.15 K.* Thermochimica Acta, 2009. **491**(1-2): p. 1-4.
18. Li, X., D. Zhu, and X. Wang, *Evaluation on dispersion behavior of the aqueous copper nano-suspensions.* Journal of colloid and interface science, 2007. **310**(2): p. 456-463.
19. Oh, D.-W., et al., *Thermal conductivity measurement and sedimentation detection of aluminum oxide nanofluids by using the 3ω method.* International Journal of Heat and Fluid Flow, 2008. **29**(5): p. 1456-1461.
20. Chiesa, M. and S.K. Das, *Experimental investigation of the dielectric and cooling performance of colloidal suspensions in insulating media.* Colloids and Surfaces A: Physicochemical and Engineering Aspects, 2009. **335**(1-3): p. 88-97.
21. Wang, X.-j. and D.-s. Zhu, *Investigation of pH and SDBS on enhancement of thermal conductivity in nanofluids.* Chemical Physics Letters, 2009. **470**(1-3): p. 107-111.

22. Witharana, S., et al., *Stability of glycol nanofluids—the theory and experiment.* Powder technology, 2013. **239**: p. 72-77.
23. Das, S.K., et al., *Temperature dependence of thermal conductivity enhancement for nanofluids.* Journal of heat transfer, 2003. **125**(4): p. 567-574.
24. Chung, S., et al., *Characterization of ZnO nanoparticle suspension in water: Effectiveness of ultrasonic dispersion.* Powder Technology, 2009. **194**(1-2): p. 75-80.
25. Hwang, Y., et al., *Investigation on characteristics of thermal conductivity enhancement of nanofluids.* Current Applied Physics, 2006. **6**(6): p. 1068-1071.
26. Song, Y.Y., H. Bhadeshia, and D.-W. Suh, *Stability of stainless-steel nanoparticle and water mixtures.* Powder Technology, 2015. **272**: p. 34-44.
27. Bandyopadhyaya, R., et al., *Stabilization of individual carbon nanotubes in aqueous solutions.* Nano letters, 2002. **2**(1): p. 25-28.
28. Islam, M., et al., *High weight fraction surfactant solubilization of single-wall carbon nanotubes in water.* Nano letters, 2003. **3**(2): p. 269-273.
29. Wu, G.S., et al. *Thermal conductivity measurement for carbon-nanotube suspensions with 3ω method*. in *Advanced Materials Research*. 2009. Trans Tech Publ.
30. Xie, H., et al., *Nanofluids containing multiwalled carbon nanotubes and their enhanced thermal conductivities.* Journal of Applied physics, 2003. **94**(8): p. 4967-4971.
31. Chen, H., Y. Ding, and A. Lapkin, *Rheological behaviour of nanofluids containing tube/rod-like nanoparticles.* Powder Technology, 2009. **194**(1-2): p. 132-141.
32. Yu, J., et al., *Controlling the dispersion of multi-wall carbon nanotubes in aqueous surfactant solution.* Carbon, 2007. **45**(3): p. 618-623.
33. Wusiman, K., et al., *Thermal performance of multi-walled carbon nanotubes (MWCNTs) in aqueous suspensions with surfactants SDBS and SDS.* International Communications in Heat and Mass Transfer, 2013. **41**: p. 28-33.
34. Kim, H.-S., et al., *Multiple light scattering measurement and stability analysis of aqueous carbon nanotube dispersions.* Journal of Physics and Chemistry of Solids, 2008. **69**(5-6): p. 1209-1212.
35. Yu, W., et al., *Enhancement of thermal conductivity of kerosene-based Fe3O4 nanofluids prepared via phase-transfer method.* Colloids and surfaces A: Physicochemical and engineering aspects, 2010. **355**(1-3): p. 109-113.
36. Cheremisinoff, N.P., *Encyclopedia of fluid mechanics*. 1986, Houston: Gulf Pub. Co., Book Division.
37. Pak, B.C. and Y.I. Cho, *Hydrodynamic and heat transfer study of dispersed fluids with submicron metallic oxide particles.* Experimental Heat Transfer an International Journal, 1998. **11**(2): p. 151-170.
38. Sharifpur, M., S. Yousefi, and J.P. Meyer, *A new model for density of nanofluids including nanolayer.* International Communications in Heat and Mass Transfer, 2016. **78**: p. 168-174.
39. Balla, H.H., et al., *Numerical study of the enhancement of heat transfer for hybrid CuO-Cu Nanofluids flowing in a circular pipe.* Journal of oleo science, 2013. **62**(7): p. 533-9.
40. O'Hanley, H., et al., *Measurement and model validation of nanofluid specific heat capacity with differential scanning calorimetry.* Advances in Mechanical Engineering, 2012. **4**: p. 181079.
41. Ho, C.J., et al., *Natural convection heat transfer of alumina-water nanofluid in vertical square enclosures: An experimental study.* International Journal of Thermal Sciences, 2010. **49**(8): p. 1345-1353.
42. Suresh, S., et al., *Synthesis of Al 2O 3-Cu/water hybrid nanofluids using two step method and its thermo physical properties.* Colloids and Surfaces A: Physicochemical and Engineering Aspects, 2011. **388**(1): p. 41-48.
43. Aybar, H.S., et al., *A Review of Thermal Conductivity Models for Nanofluids.* Heat Transfer Engineering, 2015. **36**(13): p. 1085-1110.
44. Evans, W., J. Fish, and P. Keblinski, *Role of Brownian motion hydrodynamics on nanofluid thermal conductivity.* Applied Physics Letters, 2006. **88**(9): p. 093116.
45. Keblinski, P., et al., *Mechanisms of heat flow in suspensions of nano-sized particles (nanofluids).* International Journal of Heat and Mass Transfer, 2002. **45**(4): p. 855-863.

46. Xuan, Y., Q. Li, and W. Hu, *Aggregation structure and thermal conductivity of nanofluids.* AIChE Journal, 2003. **49**(4): p. 1038-1043.
47. Jang, S.P. and S.U. Choi, *Role of Brownian motion in the enhanced thermal conductivity of nanofluids.* Applied physics letters, 2004. **84**(21): p. 4316-4318.
48. Yu, W. and S.U.S. Choi, *The Role of Interfacial Layers in the Enhanced Thermal Conductivity of Nanofluids: A Renovated Maxwell Model.* Journal of Nanoparticle Research : An Interdisciplinary Forum for Nanoscale Science and Technology, 2003. **5**(1-2): p. 167-171.
49. Yu, W. and S. Choi, *The role of interfacial layers in the enhanced thermal conductivity of nanofluids: a renovated Hamilton–Crosser model.* Journal of Nanoparticle Research, 2004. **6**(4): p. 355-361.
50. Zhou, X. and L. Gao, *Thermal conductivity of nanofluids: Effects of graded nanolayers and mutual interaction.* Journal of Applied Physics, 2008. **103**(8): p. 083503.
51. Wang, B.-X., L.-P. Zhou, and X.-F. Peng, *A fractal model for predicting the effective thermal conductivity of liquid with suspension of nanoparticles.* International Journal of Heat and Mass Transfer, 2003. **46**(14): p. 2665-2672.
52. Prasher, R., et al., *Effect of aggregation on thermal conduction in colloidal nanofluids.* Applied Physics Letters, 2006. **89**(14): p. 143119.
53. Karthikeyan, N., J. Philip, and B. Raj, *Effect of clustering on the thermal conductivity of nanofluids.* Materials Chemistry and Physics, 2008. **109**(1): p. 50-55.
54. Feng, Y., et al., *The effective thermal conductivity of nanofluids based on the nanolayer and the aggregation of nanoparticles.* Journal of Physics D: Applied Physics, 2007. **40**(10): p. 3164.
55. Girtu, M., et al., *Effects of nanoparticle clustering on the heat transport in nanofluids through fractal theories.* REVISTA DE CHIMIE-BUCHAREST-ORIGINAL EDITION-, 2008. **59**(2): p. 195.
56. Okeke, G., et al., *Computational analysis of factors influencing thermal conductivity of nanofluids.* Journal of Nanoparticle Research, 2011. **13**(12): p. 6365-6375.
57. Avsec, J., *The combined analysis of phonon and electron heat transfer mechanism on thermal conductivity for nanofluids.* International Journal of Heat and Mass Transfer, 2008. **51**(19-20): p. 4589-4598.
58. Corcione, M., *Empirical correlating equations for predicting the effective thermal conductivity and dynamic viscosity of nanofluids.* Energy Conversion and Management, 2011. **52**(1): p. 789-793.
59. Kumar, D.H., et al., *Model for heat conduction in nanofluids.* Physical Review Letters, 2004. **93**(14): p. 144301.
60. Motevasel, M., A. Soleimanynazar, and M. Jamialahmadi, *Comparing mathematical models to calculate the thermal conductivity of nanofluids.* American Journal of Oil and Chemical Technologies: Volume, 2014. **2**(11).
61. Hamilton, R.L. and O. Crosser, *Thermal conductivity of heterogeneous two-component systems.* Industrial & Engineering chemistry fundamentals, 1962. **1**(3): p. 187-191.
62. Wasp, E.J., J.P. Kenny, and R.L. Gandhi, *Solid--liquid flow: slurry pipeline transportation.[Pumps, valves, mechanical equipment, economics].* Ser. Bulk Mater. Handl.;(United States), 1977. **1**(4).
63. Bruggeman, V.D., *Berechnung verschiedener physikalischer Konstanten von heterogenen Substanzen. I. Dielektrizitätskonstanten und Leitfähigkeiten der Mischkörper aus isotropen Substanzen.* Annalen der physik, 1935. **416**(7): p. 636-664.
64. Kumar, P.M., J. Kumar, and S. Suresh, *Review on nanofluid theoretical viscosity models.* IJEIR, 2012. **1**(2): p. 128-134.
65. Ottermann, T.L., *Experimental and numerical investigation into the natural convection of TiO2-water nanofluid*. 2016, University of Pretoria.
66. Einstein, A., *A new determination of molecular dimensions.* Ann. Phys., 1906. **19**: p. 289-306.
67. Krieger, I.M. and T.J. Dougherty, *A mechanism for non-Newtonian flow in suspensions of rigid spheres.* Transactions of the Society of Rheology, 1959. **3**(1): p. 137-152.
68. Nielsen, L.E., *Generalized equation for the elastic moduli of composite materials.* Journal of Applied Physics, 1970. **41**(11): p. 4626-4627.

69. Batchelor, G., *The effect of Brownian motion on the bulk stress in a suspension of spherical particles.* Journal of fluid mechanics, 1977. **83**(1): p. 97-117.
70. Brinkman, H., *The viscosity of concentrated suspensions and solutions.* The Journal of Chemical Physics, 1952. **20**(4): p. 571-571.
71. Lundgren, T.S., *Slow flow through stationary random beds and suspensions of spheres.* Journal of Fluid Mechanics, 1972. **51**(2): p. 273-299.
72. Taylor, G.I., *The Viscosity of a Fluid Containing Small Drops of Another Fluid.* Proceedings of the Royal Society A: Mathematical, Physical and Engineering Sciences, 1932. **138**(834): p. 41-48.
73. Mooney, M., *The viscosity of a concentrated suspension of spherical particles.* Journal of Colloid Science, 1951. **6**(2): p. 162-170.
74. Frankel, N.A. and A. Acrivos, *On the viscosity of a concentrated suspension of solid spheres.* Chemical Engineering Science, 1967. **22**(6): p. 847-853.
75. Graham, A.L., *On the viscosity of suspensions of solid spheres.* Applied Scientific Research, 1981. **37**(3-4): p. 275-286.
76. Haisheng, C., D. Yulong, and T. Chunqing, *Rheological behaviour of nanofluids.* New Journal of Physics, 2007. **9**(10): p. 367-367.
77. Masoumi, N., N. Sohrabi, and A. Behzadmehr, *A new model for calculating the effective viscosity of nanofluids.* Journal of Physics D: Applied Physics, 2009. **42**(5).
78. Masoud Hosseini, S., A.R. Moghadassi, and D.E. Henneke, *A new dimensionless group model for determining the viscosity of nanofluids.* Journal of Thermal Analysis and Calorimetry : An International Forum for Thermal Studies, 2010. **100**(3): p. 873-877.
79. Graf, W.H., *Hydraulics of sediment transport*. McGraw-Hill series in water resources and environmental engineering. 1971, New York: McGraw-Hill.
80. Bieber, M., R. Kneer, and W. Rohlfs, *Self-similarity of heat transfer characteristics in laminar submerged and free-surface slot jet impingement.* International Journal of Heat and Mass Transfer, 2017. **104**: p. 1341-1352.
81. Lv, J., et al., *Experimental investigation of free single jet impingement using SiO2-water nanofluid.* Experimental Thermal and Fluid Science, 2017. **84**: p. 39-46.
82. Molana, M. and S. Banooni, *Investigation of heat transfer processes involved liquid impingement jets: a review.* Brazilian Journal of Chemical Engineering, 2013. **30**(3): p. 413-435.
83. Webb, B. and C.-F. Ma, *Single-phase liquid jet impingement heat transfer*, in *Advances in heat transfer*. 1995, Elsevier. p. 105-217.
84. Glynn, C., et al. *Jet impingement cooling*. in *Proceedings of the 9th UK National Heat Transfer Conference, Manchester, England, September*. 2005.
85. Behnia, M., et al., *Numerical study of turbulent heat transfer in confined and unconfined impinging jets.* International Journal of Heat and Fluid Flow, 1999. **20**(1): p. 1-9.
86. Choo, K.S. and S.J. Kim, *Comparison of thermal characteristics of confined and unconfined impinging jets.* International Journal of Heat and Mass Transfer, 2010. **53**(15-16): p. 3366-3371.
87. Zuckerman, N. and N. Lior, *Jet impingement heat transfer: physics, correlations, and numerical modeling.* Advances in heat transfer, 2006. **39**: p. 565-631.
88. Lienhard, J. *Heat transfer by impingement of circular free-surface liquid jets*. in *Proceedings of 18th National and 7th ISHMT-ASME Heat and Mass Transfer Conference, Guwahati, India*. 2006.
89. Carlomagno, G.M. and A. Ianiro, *Thermo-fluid-dynamics of submerged jets impinging at short nozzle-to-plate distance: A review.* Experimental thermal and fluid science, 2014. **58**: p. 15-35.
90. Saad, N., W. Douglas, and A. Mujumdar, *Prediction of heat transfer under an axisymmetric laminar impinging jet.* Industrial & Engineering Chemistry Fundamentals, 1977. **16**(1): p. 148-154.
91. Chen, Y., et al., *Theoretical study on impingement heat transfer with single-phase free-surface slot jets.* International journal of heat and mass transfer, 2005. **48**(16): p. 3381-3386.
92. Bilen, K., et al., *Heat transfer from a plate impinging swirl jet.* International journal of energy research, 2002. **26**(4): p. 305-320.

93. Hee, L.D., et al., *Turbulent heat transfer from a flat surface to a swirling round impinging jet.* International Journal of Heat and Mass Transfer, 2002. **45**(1): p. 223-227.
94. Nozaki, A., Y. Igarashi, and K. Hishida, *Heat transfer mechanism of a swirling impinging jet in a stagnation region.* Heat Transfer—Asian Research: Co-sponsored by the Society of Chemical Engineers of Japan and the Heat Transfer Division of ASME, 2003. **32**(8): p. 663-673.
95. Tawfek, A., *Heat transfer studies of the oblique impingement of round jets upon a curved surface.* Heat and Mass Transfer, 2002. **38**(6): p. 467-475.
96. Göppert, S., et al., *Heat transfer under a precessing jet: effects of unsteady jet impingement.* International Journal of Heat and Mass Transfer, 2004. **47**(12-13): p. 2795-2806.
97. Gau, C. and C. Chung, *Surface curvature effect on slot-air-jet impingement cooling flow and heat transfer process.* Journal of Heat Transfer, 1991. **113**(4): p. 858-864.
98. Fleischer, A., K. Kramer, and R. Goldstein, *Dynamics of the vortex structure of a jet impinging on a convex surface.* Experimental Thermal and Fluid Science, 2001. **24**(3-4): p. 169-175.
99. Gau, C. and C. Lee, *Impingement cooling flow structure and heat transfer along rib-roughened walls.* International Journal of Heat and Mass Transfer, 1992. **35**(11): p. 3009-3020.
100. Everts, M., *Heat transfer and pressure drop of developing flow in smooth tubes in the transitional flow regime*. 2014, University of Pretoria.
101. Cengel, Y. and A. Ghajar, *Heat and mass transfer: fundamentals and applications.* Tata McGraw-Hill, New Delhi, India, 2011.
102. Nayak, S.K., P.C. Mishra, and S.K.S. Parashar, *Enhancement of heat transfer by water-Al2O3 and water-TiO2 nanofluids jet impingement in cooling hot steel surface.* Journal of Experimental Nanoscience, 2016. **11**(16): p. 1253-1273.
103. Beck, J.V., B. Blackwell, and C.S. Clair Jr, *Inverse heat conduction problems.* Wiley&Interscience, New York, NY, 1985.
104. Bellerová, H., et al., *Spray cooling by solid jet nozzles using alumina/water nanofluids.* International Journal of Thermal Sciences, 2012. **62**: p. 127-137.
105. Tiara, A.M., et al., *Heat transfer in jet impingement on a hot steel surface using surfactant based Cu-Al layered double hydroxide nanofluid.* International Journal of Heat and Mass Transfer, 2016. **101**: p. 825-833.
106. Gherasim, I., et al., *Experimental investigation of nanofluids in confined laminar radial flows.* International Journal of Thermal Sciences, 2009. **48**(8): p. 1486-1493.
107. Jaberi, B., et al., *Experimental investigation on heat transfer enhancement due to Al2O3-water nanofluid using impingement of round jet on circular disk.* International Journal of Thermal Sciences, 2013. **74**: p. 199-207.
108. Li, Q., Y. Xuan, and F. Yu, *Experimental investigation of submerged single jet impingement using Cu-water nanofluid.* Applied Thermal Engineering, 2012. **36**(1): p. 426-433.
109. Liu, Z.-H. and Y.-H. Qiu, *Boiling heat transfer characteristics of nanofluids jet impingement on a plate surface.* Heat and Mass Transfer, 2007. **43**(7): p. 699-706.
110. Naphon, P. and S. Wongwises, *Experimental study of jet nanofluids impingement system for cooling computer processing unit.* Journal of Electronics Cooling and Thermal Control, 2011. **1**(03): p. 38.
111. Nguyen, C.T., et al., *An experimental study of a confined and submerged impinging jet heat transfer using Al2O3-water nanofluid.* International Journal of Thermal Sciences, 2009. **48**(2): p. 401-411.
112. Nguyen, C., et al. *Experimental investigation of impinging jet heat transfer and erosion effect using Al2O3-water nanofluid*. in *Proceedings of the 6th IASME/WSEAS International Conference on Fluid Mechanics and Aerodynamics (FMA'08)*. 2008. Citeseer.
113. Sun, B., Y. Qu, and D. Yang, *Heat transfer of Single Impinging Jet with Cu Nanofluids.* Applied Thermal Engineering, 2016. **102**: p. 701-707.
114. Teamah, M.A., M.M.K. Dawood, and A. Shehata, *Numerical and experimental investigation of flow structure and behavior of nanofluids flow impingement on horizontal flat plate.* Experimental Thermal and Fluid Science, 2016. **74**: p. 235-246.

115. Wongcharee, K., V. Chuwattanakul, and S. Eiamsa-ard, *Heat transfer of swirling impinging jets with TiO2-water nanofluids.* Chemical Engineering & Processing: Process Intensification, 2017. **114**: p. 16-23.
116. Yousefi, T., et al., *An experimental investigation on the impingement of a planar jet of Al2O3-water nanofluid on a V-shaped plate.* Experimental Thermal and Fluid Science, 2013. **50**: p. 114-126.
117. Zeitoun, O. and M. Ali, *Nanofluid impingement jet heat transfer.* Nanoscale Research Letters, 2012. **7**(1): p. 1-13.
118. Zhou, M., G. Xia, and L. Chai, *Heat transfer performance of submerged impinging jet using silver nanofluids.* Heat and Mass Transfer : Wärme- und Stoffübertragung, 2015. **51**(2): p. 221-229.
119. Mitra, S., et al., *Study on boiling heat transfer of water-TiO2 and water-MWCNT nanofluids based laminar jet impingement on heated steel surface.* Applied Thermal Engineering, 2012. **37**: p. 353-359.
120. Modak, M., et al., *Experimental investigation of heat transfer characteristics of the hot surface using Al2O3–water nanofluids.* Chemical Engineering and Processing: process intensification, 2015. **91**: p. 104-113.
121. Sarkar, I., et al., *Ultrafast cooling of a hot steel plate using Cu-Al layered double hydroxide nanofluid jet.* International Journal of Thermal Sciences, 2017. **116**: p. 52-62.
122. Singh, M.K., et al., *Effect of nanofluid concentration and composition on laminar jet impinged cooling of heated steel plate.* Applied Thermal Engineering, 2016. **100**: p. 237-246.
123. Tiara, A.M., et al., *Effect of alumina nanofluid jet on the enhancement of heat transfer from a steel plate.* Heat and Mass Transfer : Wärme- und Stoffübertragung, 2017. **53**(6): p. 2187-2197.
124. Sajid, M., et al., *Impact of nanoparticles on human and environment: review of toxicity factors, exposures, control strategies, and future prospects.* Environmental Science and Pollution Research, 2015. **22**(6): p. 4122-4143.
125. Popiel, C.O. and J. Wojtkowiak, *Simple Formulas for Thermophysical Properties of Liquid Water for Heat Transfer Calculations (from 0°C to 150°C).* Heat Transfer Engineering, 1998. **19**(3): p. 87-101.
126. Lv, J., et al., *Experimental investigation of free single jet impingement using Al2O3-water nanofluid.* International Communications in Heat and Mass Transfer, 2017. **88**: p. 126-135.
127. Moffat, R.J., *Describing the uncertainties in experimental results.* Experimental Thermal and Fluid Science, 1988. **1**(1): p. 3-17.
128. Dunn, P.F., *Measurement and data analysis for engineering and science*. 2nd ed. ed. 2010, Boca Raton, FL: CRC Press/Taylor & Francis.
129. Wang, X., X. Xu, and S.U. S. Choi, *Thermal conductivity of nanoparticle-fluid mixture.* Journal of thermophysics and heat transfer, 1999. **13**(4): p. 474-480.
130. He, Y., et al., *Numerical investigation into the convective heat transfer of TiO2 nanofluids flowing through a straight tube under the laminar flow conditions.* Applied Thermal Engineering, 2009. **29**(10): p. 1965-1972.
131. Joubert, J., M. University of Pretoria. Department of, and E. Aeronautical, *Influence of a magnetic field on magnetic nanofluids for the purpose of enhancing natural convection heat transfer*. 2017, BUniversity of Pretoria: Pretoria.
132. Yaohua, Z., et al., *Conjugated Heat Transfer on a Horizontal Surface Impinged by Circular Free-Surface Liquid Jet.* JSME international journal. Ser. B, Fluids and thermal engineering., 2002. **45**(2): p. 307-314.
133. Barewar, S.D., S. Tawri, and S.S. Chougule, *Heat transfer characteristics of free nanofluid impinging jet on flat surface with different jet to plate distance: An experimental investigation.* Chemical Engineering and Processing - Process Intensification, 2019. **136**: p. 1-10.
134. Beckwith, T.G., R.D. Marangoni, and J.H. Lienhard, *Mechanical measurements*. 5th ed. ed. 1993, Reading, Mass.: Addison-Wesley.

Appendix A: Thermocouple calibration

A.1. Introduction

A thermocouple is an electrical device or sensor that may be utilised to measure temperature. Thermocouples are composed of two dissimilar electrical conductors that form a junction at varying temperatures. Depending on the nature of the thermocouple junction, the channel of the data logger in which it is connected, as well as several other factors, no two thermocouples will produce the same temperature measurement. As a result, thermocouples should undergo calibration in order to guarantee accuracy of their readings.

The following section describes the process conducted to ensure the successful calibration of the 12 different thermocouples used in the study, as well as the resulting calibration factors for each thermocouple and the random measurements taken to ensure successful calibration.

A.2. Thermocouple calibration

To successfully calibrate the different thermocouples used in the investigation, a thermal bath (Polyscience PD20R-30-A12E, USA) with temperature stability of ±0.005 ℃ was used. During the calibration process, the temperature of the bath was varied from 15 ℃ to 80 ℃, at intervals of 2.5 ℃, and the temperature readings of the different thermocouples were compared with those of an internal PT-100 probe. This internal PT-100 probe had an accuracy of 0.1 ℃.

In terms of the measurement process, 600 measuring points with a frequency of 2kHz were used. Once all measurements were taken, the resulting averaged data for each thermocouple was plotted against the readings generated by the internal PT-100 probe. Using linear regression, the following expression was valid in terms of obtaining the calibrated thermocouple temperature reading:

$$T_{cal} = \frac{T_{uncal} - c}{\hat{m}} \tag{A.1}$$

where m and c are the regression constants and T_{cal} and T_{uncal} are the calibrated and uncalibrated thermocouple temperature readings respectively.

Note: The appropriate regression constants were obtained through the use of the built-in regression function of Microsoft Excel for a confidence level of 95%.

Table A.1 displays the appropriate regression constants for each of the thermocouples when calibrated against the PT-100 probe.

Table A.1. Thermocouple calibration factors

Thermocouple number	$\hat{m}$	c
1	0.98181	0.9254
2	0.98062	1.1080
3	0.99412	0.5374
4	0.99317	0.6041
5	0.99410	0.4141
6	0.99441	0.2562

7	0.99296	0.6635
8	0.97849	1.1080
9	0.97704	1.0757
10	0.97822	1.1076
11	0.97731	1.1744
12	0.97731	0.97856

To ensure that the calibration of the different thermocouples was successful, four random temperature values, namely 34.25, 48.4, 63.8 and 76.1 ℃ were chosen. Figure A.1 graphically compares the calibrated and uncalibrated readings of the different thermocouples for each of the selected temperature values.

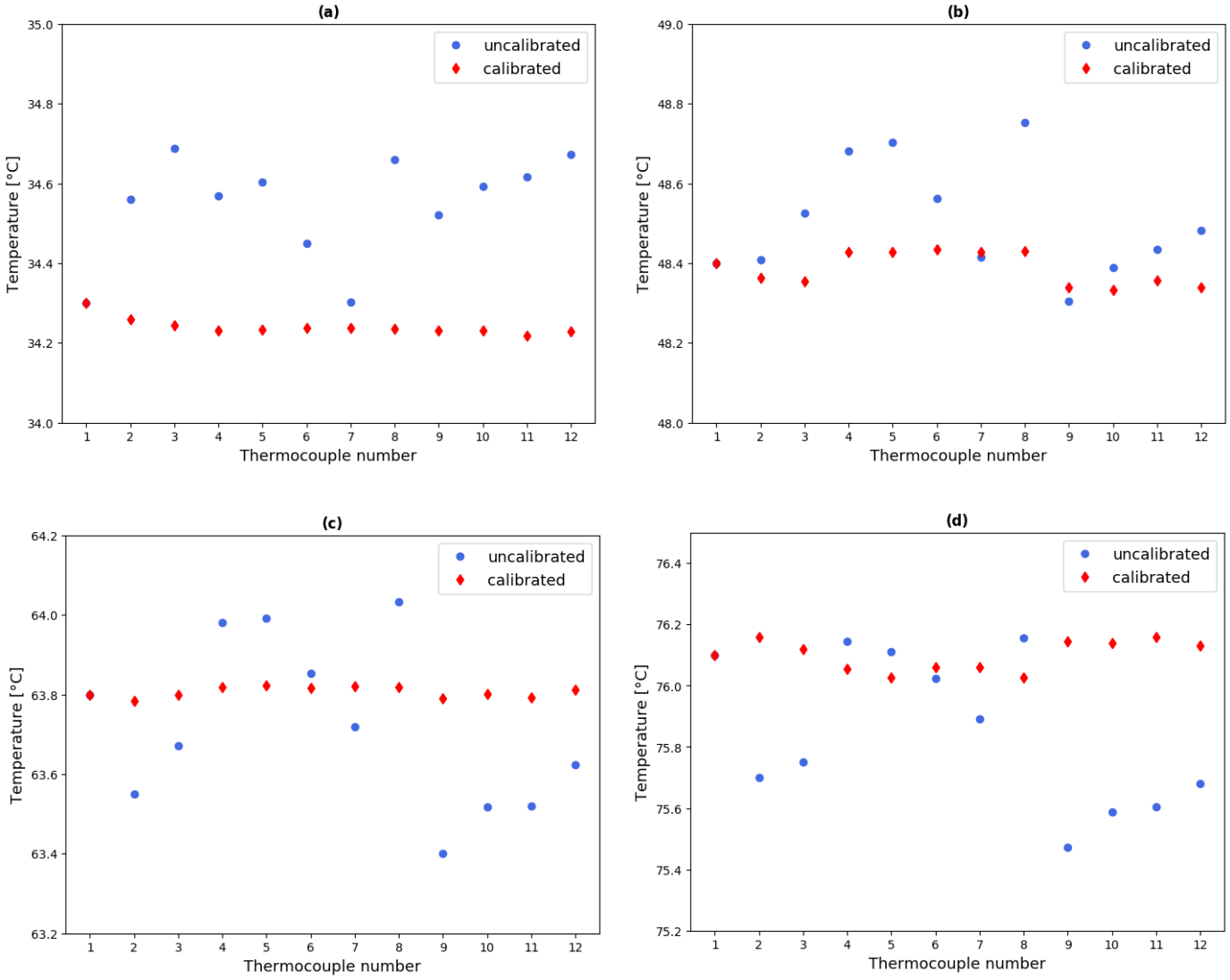

Figure A.1. Calibrated and uncalibrated thermocouple readings for (a) 34.25 ℃, (b) 48.4 ℃, (c) 63.8 ℃ and (d) 76.1 ℃

The above plots clearly indicate that the calibration process was a success. Based on the data in Figure A.1, it was found that the average standard deviation in thermocouples was approximately 0.029 ℃.

Furthermore, upon completing the applicable uncertainty analysis, discussed in further detail in Appendix B, it was found that the maximum thermocouple uncertainty was 0.119 ℃.

A.3. Conclusion

The previous section discussed the calibration process for the twelve different thermal couples used in the experimental investigation (7 K-type and 5 T-type thermocouples). As stated above, calibration produced a maximum thermocouple uncertainty of 0.119 ℃ and was conducted by means of a thermal bath with internal probe accuracy of ±0.1 ℃ and thermal stability of ±0.005 ℃.

Once successful calibration was confirmed, the different thermocouples were positioned in their appropriate locations in the test rig. No thermocouple was soldered to the set-up, but they were rather fixed by alternative means. The thermocouples positioned within the heated target surface or copper cylinder were coated in a suitable thermal paste to eliminate any air gaps that could potentially hinder their thermal readings.

A.4. Nomenclature

$\hat{c}$	y-intercept	
$\hat{m}$	Slope	
T	Temperature	℃ or K

A.4.1. Subscripts

cal	Calibrated value
$uncal$	Uncalibrated value

Appendix B: Uncertainty analysis

B.1. Introduction

During the investigation, multiple parameters applicable to the study were measured and calculated. Therefore, it was of paramount importance to define the level of uncertainty associated with these parameters. The following section defines the uncertainty analysis conducted as well as resulting uncertainties for the various parameters of interest. Additionally, this section also discusses some initial theory relating to the uncertainty analysis with particular focus on the types of errors.

B.2. Theory of the uncertainty analysis

To accurately estimate the size of errors in the measurement process, it is first important to have some understanding of the classification and cause of such errors. According to Beckwith et al. [134], there are two basic types of errors, namely bias or systematic error and precision or random error. The bias or systematic error refers to deviations that are not due to chance alone, but rather associated with equipment calibration error and other related imperfections. Usually, bias errors will be specified by the manufacturer of the appropriate instrument or piece of equipment being used. The precision or random error, also referred to as "variability", is a direct result of fluctuations or noise that arises during the measurement process.

As highlighted by Everts [100], the magnitudes of the bias and precision errors correspond to the 95% probability that the actual error will not be more than the estimated figure. The uncertainty in a single measurement, defined by Dunn [128], was calculated as follows:

$$\delta x_i = \sqrt{b_i^2 + p_i^2} \tag{B.1}$$

where x_i is a single observation and δx_i is the standard deviation multiplied by the appropriate *t*-variable.

For the case of R, which is a function of multiple variables, it was calculated from a group of equations as indicated by the following expression:

$$R = R(x_1, x_2, x_3, \dots, x_n) \tag{B.2}$$

The uncertainty of R, provided that the uncertainties of x_i were known, was determined as follows:

$$\delta R = \frac{\partial R}{\partial x_i}\delta x_i \tag{B.3}$$

The sensitivity coefficient, δR, indicates the effect that x_i has on the overall uncertainty of R.

To calculate the uncertainty of a parameter, R, with several independent variables, the root square method was used. The root square method was expressed as follows:

$$\delta R = \sqrt{\left[\left(\frac{\partial R}{\partial x_1}\right)^2 \delta x_1 + \left(\frac{\partial R}{\partial x_2}\right)^2 \delta x_2 + \left(\frac{\partial R}{\partial x_3}\right)^2 \delta x_3 + \dots + \left(\frac{\partial R}{\partial x_n}\right)^2 \delta x_n\right]} \tag{B.4}$$

According to Dunn [128], regression analysis is a tool that is used to determine the relationship between two or more variables. Despite the multiple forms of regression analysis, they all aim to examine the influence of one or more independent variables on a dependent variable.

In general, the *x*-variable is known and is, therefore, termed the independent variable, while the *y*-variable, obtained through measurements, is the dependent variable. As a result, the uncertainty arose from the *y*-variable and was determined as follows:

$$\delta y = \pm t S_{yx} \sqrt{\frac{1}{N} + \frac{1}{M} + \frac{(x_i - \bar{x})^2}{S_{xx}}} \tag{B.5}$$

where t is the appropriate *t*-variable, N is the number of measuring points and M is the number of observations.

The sum of the difference between the x and $\bar{x}$ (mean x value), S_{xx}, was defined as follows:

$$S_{xx} = \sum_{i=1}^{N} (x_i - \bar{x})^2 \tag{B.6}$$

The approximation of S_{yx} is as follows:

$$S_{yx} = \sqrt{\frac{\sum_{i=1}^{N} (y_i - y_{ci})^2}{N - 2}} \tag{B.7}$$

where y_{ci} was determined using the following expression:

$$y_{ci} = \hat{m}\bar{x} + \hat{c} \tag{B.8}$$

Parameters $\hat{m}$ and $\hat{c}$ were calculated using equations B.9 and B.10 respectively.

$$\hat{m} = \frac{S_{xy}}{S_{xx}} \tag{B.9}$$

$$\hat{c} = \bar{y} - \hat{m}\bar{x} \tag{B.10}$$

With respect to equation B.9, S_{xy} was determined as follows:

$$S_{xy} = \sum_{i=1}^{N} (x_i - \bar{x})(y_i - \bar{y}) \tag{B.11}$$

To determine the uncertainty within the *x*-variable, the uncertainty in the *y*-variable was divided by the slope of the regression line as follows:

$$\delta x = \frac{\delta y}{\hat{m}} \tag{B.12}$$

This method of linear regression analysis was used in determining the uncertainty of the different thermocouples after completing the calibration process discussed in Appendix A.

B.3. Instrumentation

Regarding the uncertainty of the instrumental measurements, the bias as specified by the manufacturer was used. The precision of the readings was determined from the standard deviation of 600 measuring points, which was then multiplied by the appropriate *t*-variable to fall within the 95% confidence region. With both the bias and precision errors known, the total uncertainty of each instrument was approximated using equation B.1.

B.3.1. Thermocouples

To successfully calibrate the different thermocouples, a thermal bath (Polyscience PD20R-30-A12E, USA) with temperature stability of ±0.005 ℃ and an internal PT-100 probe with an accuracy of 0.1 ℃ was utilised. During the calibration process, the readings of 27 observation points of 600 measurements were taken between 15 ℃ and 80 ℃.

The readings of each thermocouple were then plotted against that of the internal PT-100 probe, where linear regression was used to obtain the appropriate calibration factors of each probe. Using equations B.5 to B.12, the precision of each thermocouple was approximated. The bias factor was taken to be that of the PT-100 probe (0.1 ℃). Through the use of equation B.1, the uncertainty values of the different thermocouples were found to be between 0.11 ℃ and 0.12 ℃.

B.3.2. Flow meter

The volumetric flow rate of the fluid within the test rig was measured by means of an ultrasonic flow meter (Type 8081, supplied Bürkert) with an accuracy of 0.01% of the full scale and 2% of the measured value.

B.3.3. Amp and voltmeter

To determine the total electric power applied to the heaters in the target section, the power-law relation of current and voltage was utilised. To measure the current and voltage across the heaters, both an amp meter (Type 2053, supplied by Yokogawa) and voltmeter (Type 2052, supplied by Yokogawa) were connected in series and parallel respectively. The accuracies of these meters, with respect to the tested ranges, were 0.05 A and 5 V.

B.3.4. Diameter and length

All length- and diameter-related measurements of the test specimen were taken using a 150 mm Vernier Caliper with an accuracy of 0.02 mm (Tricle Brand, China).

B.4. Fluid properties

Because water and varying volume fractions of TiO_2-water nanofluid were used in the experimental study, both fluids required an uncertainty analysis in terms of their associated thermophysical properties. Therefore, the following subsection discusses the relative uncertainties of the calculated thermophysical properties of water and the TiO_2-nanofluids.

B.4.1. Water properties

All water properties used in the experimental investigation were derived from the simple formulations proposed by Popiel and Wojtkowiak [125]. Table B.1 exhibits the appropriate uncertainties of these equations.

Table B.1. Uncertainties of calculated thermophysical properties of water

Thermophysical property	Uncertainty
Density [$\boldsymbol{kg/m^3}$]	0.003%
Specific heat [$\boldsymbol{J/kg \cdot K}$]	0.04%
Thermal conductivity [$\boldsymbol{W/m \cdot K}$]	2%
Dynamic viscosity [$\boldsymbol{kg/m \cdot s}$]	1%

B.4.2. TiO_2-water properties

The thermophysical properties of the different volume concentrations of TiO_2-water nanofluid were calculated using several different equations and measurements. As a result, each property and its corresponding uncertainty, based on the formula used, is discussed independently in the following sections.

B.4.2.1. Density

The density of the nanofluid was approximated using the mixing theory, expressed as follows:

$$\rho_{nf} = (1-\varphi)\rho_{bf} + \varphi\rho_{np} \tag{B.13.1}$$

Therefore, the uncertainty of the density of the fluid is expressed as follows:

$$\delta\rho_{nf} = \left[\left(\frac{\partial\rho_{nf}}{\partial\rho_{bf}}\cdot\delta\rho_{bf}\right)^2 + \left(\frac{\partial\rho_{nf}}{\partial\rho_{np}}\cdot\delta\rho_{np}\right)^2\right]^{\frac{1}{2}}$$

$$\delta\rho_{nf} = \left[\left((1-\varphi)\cdot\delta\rho_{bf}\right)^2 + \left(\varphi\cdot\delta\rho_{np}\right)^2\right]^{\frac{1}{2}} \tag{B.13.2}$$

The density of the TiO_2 nanoparticles was specified to be 4250 kg/m^3 and therefore it could be assumed that no uncertainty was associated with this quantity. Therefore, equation B.13.2 was simplified as follows:

$$\delta\rho_{nf} = (1-\varphi)\cdot\delta\rho_{bf}$$

B.4.2.2. Specific heat

Equation B.14.1 was used to determine the appropriate specific heat of each of the different volume fractions of nanofluid as follows:

$$c_{p_{nf}} = \frac{\varphi c_{p_{np}}\rho_{np} + (1-\varphi)c_{p_{bf}}\rho_{bf}}{\rho_{nf}} \tag{B.14.1}$$

The resulting uncertainty of this approximated quantity was found as follows:

$$\delta c_{p_{nf}} = \left[\left(\frac{\partial c_{p_{nf}}}{\partial c_{p_{np}}}\cdot\delta c_{p_{np}}\right)^2 + \left(\frac{\partial c_{p_{nf}}}{\partial\rho_{np}}\cdot\delta\rho_{np}\right)^2 + \left(\frac{\partial c_{p_{nf}}}{\partial c_{p_{bf}}}\cdot\delta c_{p_{bf}}\right) + \left(\frac{\partial c_{p_{nf}}}{\partial\rho_{bf}}\cdot\delta\rho_{bf}\right)^2 + \left(\frac{\partial c_{p_{nf}}}{\partial\rho_{nf}}\cdot\delta\rho_{nf}\right)^2\right]^{\frac{1}{2}}$$

$$\delta c_{p_{nf}} = \left[\left(\frac{\varphi \rho_{np}}{\rho_{nf}} \cdot \delta c_{p_{np}} \right)^2 + \left(\frac{\varphi c_{p_{np}}}{\rho_{nf}} \cdot \delta \rho_{np} \right)^2 + \left(\frac{(1-\varphi)\rho_{bf}}{\rho_{nf}} \cdot \delta c_{p_{bf}} \right)^2 + \left(\frac{(1-\varphi)c_{p_{bf}}}{\rho_{nf}} \cdot \delta \rho_{bf} \right)^2 + \left(-\frac{\left(\varphi c_{p_{np}} \rho_{np} + (1-\varphi) c_{p_{bf}} \rho_{bf}\right)}{\rho_{nf}^2} \cdot \delta \rho_{nf} \right)^2 \right]^{\frac{1}{2}} \quad \text{(B.14.2)}$$

As mentioned previously, the thermophysical properties of the TiO_2 nanoparticles were given and therefore had been assumed to possess no uncertainty. Based on this assumption, the above expression was simplified as follows:

$$\delta c_{p_{nf}} = \left[\left(\frac{(1-\varphi)\rho_{bf}}{\rho_{nf}} \cdot \delta c_{p_{bf}} \right)^2 + \left(\frac{(1-\varphi)c_{p_{bf}}}{\rho_{nf}} \cdot \delta \rho_{bf} \right)^2 + \left(-\frac{\left(\varphi c_{p_{np}} \rho_{np} + (1-\varphi) c_{p_{bf}} \rho_{bf}\right)}{\rho_{nf}^2} \cdot \delta \rho_{nf} \right)^2 \right]^{\frac{1}{2}}$$

B.4.2.3. Thermal conductivity

The empirical model of He et al. [130], specifically developed for predicting the thermal conductivity of TiO_2-water nanofluids, was used as follows:

$$k_{nf} = k_{bf} \cdot (125.62\varphi^2 + 4.82\varphi + 1) \quad \text{(B.15.1)}$$

The associated uncertainty of the quantities, found by these means, was expressed as follows:

$$\delta k_{nf} = \left[\left(\frac{\partial k_{nf}}{\partial k_{bf}} \cdot \delta k_{bf} \right)^2 \right]^{1/2}$$

$$\delta k_{nf} = (125.62\varphi^2 + 4.82\varphi + 1) \cdot \delta k_{bf} \quad \text{(B.15.2)}$$

B.4.2.4. Viscosity

The viscosity of the different nanofluid samples was measured using an SV-10 Sine Wave Vibro-viscometer (A&D, Japan) with an accuracy of 1% over its full range (0.3 to 10 000 $mPa \cdot s$).

B.5. Calculated parameters

B.5.1. Temperature

B.5.1.1. Inlet jet temperature

To monitor the inlet temperature of the fluid before being expelled by the nozzle, a single thermocouple was positioned within the jet and was secured through the use of a compression fitting. The associated uncertainty for the inlet jet temperature was therefore found to be 0.113 ℃.

B.5.1.2. Surface temperature

As stated in Chapter 3, six thermocouples were positioned in the heated test section at varying axial distances from the target surface. Using Fourier's law of heat conduction, it was possible to approximate the temperature at the surface using any of the thermocouples. By taking an average of the five surface temperatures, obtained using the different thermocouples, a representative surface temperature was obtained. Therefore, the average surface temperature was defined as follows:

$$\bar{T}_s = \frac{T_{s,1} + T_{s,2} + T_{s,3} + T_{s,4} + T_{s,5}}{5} \tag{B.16.1}$$

where the surface temperature, based on a particular internal thermocouple, was calculated using equation B.16.2:

$$T_{s,i} = T_{TC,i} - \frac{\dot{q}_{weight}\Delta x_{s,i}}{k_c} \tag{B.16.2}$$

Therefore, the uncertainty of each surface temperature was approximated as follows:

$$\delta T_{s,i} = \left[\left(\frac{\partial T_{s,i}}{\partial T_{TC,i}} \cdot \delta T_{TC,i}\right)^2 + \left(\frac{\partial T_{s,i}}{\partial \dot{q}_{weight}} \cdot \delta \dot{q}_{weight}\right)^2 + \left(\frac{\partial T_{s,i}}{\partial \Delta x_{s,i}} \cdot \delta \Delta x_{s,i}\right)^2 + \left(\frac{\partial T_{s,i}}{\partial k_c} \cdot \delta k_c\right)^2\right]^{1/2}$$

$$\delta T_{s,i} = \left[\left(\delta T_{TC,i}\right)^2 + \left(-\frac{\Delta x_{s,i}}{k_c} \cdot \delta \dot{q}_{weight}\right)^2 + \left(-\frac{\dot{q}_{weight}}{k_c} \cdot \delta \Delta x_{s,i}\right)^2 + \left(\frac{\dot{q}_{weight}\Delta x_{s,i}}{k_c^2} \cdot \delta k_c\right)^2\right]^{1/2} \tag{B.16.3}$$

It was assumed that the thermal conductivity of the copper specimen was without any associated error and is represented as follows:

$$\delta T_{s,i} = \left[\left(\delta T_{TC,i}\right)^2 + \left(-\frac{\Delta x_{s,i}}{k_c} \cdot \delta \dot{q}_{weight}\right)^2 + \left(-\frac{\dot{q}_{weight}}{k_c} \cdot \delta \Delta x_{s,i}\right)^2\right]^{1/2}$$

The resulting error in the averaged surface temperature was then calculated as follows:

$$\delta\bar{T}_s = \left[\left(\frac{\delta T_{s,1}}{5}\right)^2 + \left(\frac{\delta T_{s,2}}{5}\right)^2 + \left(\frac{\delta T_{s,3}}{5}\right)^2 + \left(\frac{\delta T_{s,4}}{5}\right)^2 + \left(\frac{\delta T_{s,5}}{5}\right)^2\right]^{\frac{1}{2}} \quad \text{(B.16.4)}$$

B.5.1.3. Jet exit temperature

Similar to the approximation of the surface temperature of the heated target surface, the exit jet temperature was also determined by taking an average reading of the appropriate thermocouples at the location.

The average exit temperature and the uncertainty of quantity were determined by means of equation B.17.1 and B.17.2 respectively as follows:

$$\bar{T}_e = \frac{T_{e,1} + T_{e,2} + T_{e,3} + T_{e,4} + T_{e,5}}{5} \quad \text{(B.17.1)}$$

$$\delta\bar{T}_e = \left[\left(\frac{\delta T_{e,1}}{5}\right)^2 + \left(\frac{\delta T_{e,2}}{5}\right)^2 + \left(\frac{\delta T_{e,3}}{5}\right)^2 + \left(\frac{\delta T_{e,4}}{5}\right)^2 + \left(\frac{\delta T_{e,5}}{5}\right)^2\right]^{\frac{1}{2}} \quad \text{(B.17.2)}$$

*B.5.1.4. Bulk fluid tem*perature

With the jet inlet and exit fluid temperature values and their respective uncertainties known, the bulk fluid temperature and its associated uncertainty were determined as follows:

$$T_b = \frac{(T_j + T_e)}{2} \quad \text{(B.18.1)}$$

$$\delta T_b = \left[\left(\frac{\delta T_j}{2}\right)^2 + \left(\frac{\delta T_e}{2}\right)^2\right]^{\frac{1}{2}} \quad \text{(B.18.2)}$$

B.5.2. Mass flow rate

Based on the flow rate readings obtained from the ultrasonic flow meter, the mass flow rate of fluid within the system was determined as follows:

$$\dot{m} = \rho\dot{V} \quad \text{(B.19.1)}$$

Therefore, the associated uncertainty in the mass flow rate was dependent on the uncertainty of the fluid density and that of the flow meter. The uncertainty was determined as follows:

$$\delta\dot{m} = \left[\left(\frac{\partial\dot{m}}{\partial\rho}\cdot\delta\rho\right)^2 + \left(\frac{\partial\dot{m}}{\partial\dot{V}}\cdot\delta\dot{V}\right)^2\right]^{\frac{1}{2}}$$

$$\delta\dot{m} = \left[\left(\dot{V}\cdot\delta\rho\right)^2 + \left(\rho\cdot\delta\dot{V}\right)^2\right]^{\frac{1}{2}} \quad \text{(B.19.2)}$$

The total degree of uncertainty in the mass flow rate was then determined as follows:

$$\frac{\delta \dot{m}}{\dot{m}} = \left[\left(\frac{\delta \rho}{\rho}\right)^2 + \left(\frac{\delta \dot{V}}{\dot{V}}\right)^2\right]^{\frac{1}{2}} \tag{B.19.3}$$

B.5.3. Fluid velocity

With the volume flow rate and cross-sectional area of the jet nozzle known, the fluid velocity and the uncertainty of the parameter were approximated as follows:

$$U = \frac{\dot{V}}{A_j} \tag{B.20.1}$$

$$\delta U = \left[\left(\frac{\partial U}{\partial \dot{V}} \cdot \delta \dot{V}\right)^2 + \left(\frac{\partial U}{\partial A_j} \cdot \delta A_j\right)^2\right]^{\frac{1}{2}}$$

$$\delta U = \left[\left(\frac{1}{A_j} \cdot \delta \dot{V}\right)^2 + \left(-\frac{\dot{V}}{A_j^2} \cdot \delta A_j\right)^2\right]^{\frac{1}{2}} \tag{B.20.2}$$

Based on the assumption that the diameter of the jet nozzle provided by the manufacturer was correct, there was no uncertainty in the cross-sectional area of the nozzle. Therefore, Equation B.20.2 was simplified as follows:

$$\delta U = \frac{1}{A_j} \cdot \delta \dot{V}$$

Combining equation B.20.1 and B.20.2 produced the following relation for determining the total uncertainty in the jet fluid velocity:

$$\frac{\delta U}{U} = \frac{\delta \dot{V}}{\dot{V}} \tag{B.20.3}$$

B.5.4 Reynolds number

The Reynolds number and the uncertainty of the parameter were determined as follows:

$$Re = \frac{\rho \cdot U \cdot D_j}{\mu} \tag{B.21.1}$$

$$\delta Re = \left[\left(\frac{\partial Re}{\partial \rho} \cdot \delta \rho\right)^2 + \left(\frac{\partial Re}{\partial U} \cdot \delta U\right)^2 + \left(\frac{\partial Re}{\partial D_j} \cdot \delta D_j\right)^2 + \left(\frac{\partial Re}{\partial \mu} \cdot \delta \mu\right)^2\right]^{\frac{1}{2}}$$

$$\delta Re = \left[\left(\frac{U \cdot D_j}{\mu} \cdot \delta\rho\right)^2 + \left(\frac{\rho \cdot D_j}{\mu} \cdot \delta U\right)^2 + \left(\frac{\rho \cdot U}{\mu} \cdot \delta D_j\right)^2 + \left(-\frac{\rho \cdot U \cdot D_j}{\mu^2} \cdot \delta\mu\right)^2\right]^{\frac{1}{2}} \quad \text{(B.21.2)}$$

Again, based on the assumption that the jet nozzle diameter was exactly as specified by the manufacturer, the uncertainty of the parameter was 0%. Therefore, equation B.21.2 is written as follows:

$$\delta Re = \left[\left(\frac{U \cdot D_j}{\mu} \cdot \delta\rho\right)^2 + \left(\frac{\rho \cdot D_j}{\mu} \cdot \delta U\right)^2 + \left(-\frac{\rho \cdot U \cdot D_j}{\mu^2} \cdot \delta\mu\right)^2\right]^{\frac{1}{2}}$$

The total degree of uncertainty in the Reynolds number was finally found as follows:

$$\frac{\delta Re}{Re} = \left[\left(\frac{\delta\rho}{\rho}\right)^2 + \left(\frac{\delta U}{U}\right)^2 + \left(-\frac{\delta\mu}{\mu}\right)^2\right]^{\frac{1}{2}} \quad \text{(B.21.3)}$$

B.5.5. Heated target surface area

The surface area of the target surface and its corresponding uncertainty were determined by means of equations B.22.1 and B.22.2 respectively as follows:

$$A_s = \frac{\pi}{4} \cdot D_s^2 \quad \text{(B.22.1)}$$

$$\delta A_s = \left[\left(\frac{\partial A_s}{\partial D_s} \cdot \delta D_s\right)^2\right]^{\frac{1}{2}}$$

$$\delta A_s = \frac{\pi D_s}{2} \cdot \delta D_s \quad \text{(B.22.2)}$$

Through the use of equations B.22.1 and B.22.2, the following expression was obtained for the total uncertainty in the approximated target surface area:

$$\frac{\delta A_s}{A_s} = 2 \cdot \frac{\delta D_s}{D_s} \quad \text{(B.22.3)}$$

B.5.6. Heater power input (electrical power input)

As specified in Section B.3.3, the total electrical power supplied to the heaters was determined by means of the following relation:

$$\dot{Q}_{elec} = V \cdot I \quad \text{(B.23.1)}$$

Because the uncertainties in the current and voltage readings were known, the uncertainty in the calculated electrical power was found as follows:

$$\delta\dot{Q}_{elec} = \left[\left(\frac{\partial\dot{Q}_{elec}}{\partial V}\delta V\right)^2 + \left(\frac{\partial\dot{Q}_{elec}}{\partial I}\delta I\right)^2\right]^{\frac{1}{2}}$$

$$\delta\dot{Q}_{elec} = [(I\cdot\delta V)^2 + (V\cdot\delta I)^2]^{\frac{1}{2}} \tag{B.23.2}$$

Combining equations B.23.1 and B.23.2 produced the following expression for the overall uncertainty of the electrical input power:

$$\frac{\delta\dot{Q}_{elec}}{\dot{Q}_{elec}} = \left[\left(\frac{\delta V}{V}\right)^2 + \left(\frac{\delta I}{I}\right)^2\right]^{\frac{1}{2}} \tag{B.23.3}$$

B.5.7. Heat flux

The heat flux between any two thermocouple levels within the copper specimen was approximated by means of Fourier's heat conduction law as follows:

$$\dot{q} = -k_c\cdot\frac{\Delta T}{\Delta x} \tag{B.24.1}$$

Therefore, the associated uncertainty with the calculated heat flux at a particular level in the copper specimen was determined as follows:

$$\delta\dot{q} = \left[\left(\frac{\partial\dot{q}}{\partial k_c}\delta k_c\right)^2 + \left(\frac{\partial\dot{q}}{\partial\Delta x}\delta\Delta x\right)^2 + \left(\frac{\partial\dot{q}}{\partial\Delta T}\delta\Delta T\right)^2\right]^{\frac{1}{2}}$$

$$\delta\dot{q} = \left[\left(-\frac{\Delta T}{\Delta x}\delta k_c\right)^2 + \left(\frac{k_c\Delta T}{\Delta x^2}\delta\Delta x\right)^2 + \left(-\frac{k_c}{\Delta x}\delta\Delta T\right)^2\right]^{\frac{1}{2}} \tag{B.24.2}$$

Assuming that the thermal conductivity of the copper specimen was without any associated error, it was expressed as follows:

$$\delta\dot{q} = \left[\left(\frac{k_c\Delta T}{\Delta x^2}\delta\Delta x\right)^2 + \left(-\frac{k_c}{\Delta x}\delta\Delta T\right)^2\right]^{\frac{1}{2}}$$

The total heat flux of the copper target surface was determined by taking a weighted average of the different heat fluxes located at the five varying axial levels. The weighted average and associated uncertainty are presented by equations B.24.3 and B.24.4 respectively as follows:

$$\dot{q}_{weight} = \frac{4}{28}\dot{q}_{12} + \frac{6}{28}\dot{q}_{23} + \frac{8}{28}\dot{q}_{34} + \frac{10}{28}\dot{q}_{45} \tag{B.24.3}$$

$$\delta\dot{q}_{weight} = \left[\left(\frac{4\cdot\delta\dot{q}_{12}}{28}\right)^2 + \left(\frac{6\cdot\delta\dot{q}_{23}}{28}\right)^2 + \left(\frac{8\delta\dot{q}_{34}}{28}\right)^2 + \left(\frac{10\cdot\delta\dot{q}_{45}}{28}\right)^2\right]^{\frac{1}{2}} \quad \text{(B.24.4)}$$

The total uncertainty of the weighted heat flux was approximated as follows:

$$\frac{\delta\dot{q}_{weight}}{\dot{q}_{weight}} = \left[\left(\frac{4\cdot\delta\dot{q}_{12}}{4\dot{q}_{12}+6\dot{q}_{23}+8\dot{q}_{34}+10\dot{q}_{45}}\right)^2 + \left(\frac{6\cdot\delta\dot{q}_{23}}{4\dot{q}_{12}+6\dot{q}_{23}+8\dot{q}_{34}+10\dot{q}_{45}}\right)^2 + \left(\frac{8\delta\dot{q}_{34}}{4\dot{q}_{12}+6\dot{q}_{23}+8\dot{q}_{34}+10\dot{q}_{45}}\right)^2 + \left(\frac{10\cdot\delta\dot{q}_{45}}{4\dot{q}_{12}+6\dot{q}_{23}+8\dot{q}_{34}+10\dot{q}_{45}}\right)^2\right]^{\frac{1}{2}} \quad \text{(B.24.5)}$$

B.5.8. Heat transfer coefficient

The heat transfer coefficient of the experimental runs was determined as follows:

$$h = \frac{\dot{q}}{T_s - T_j} \quad \text{(B.25.1)}$$

Based on the correlation, the total uncertainty of the parameter was determined as follows:

$$\delta h = \left[\left(\frac{\partial h}{\partial q}\delta q\right)^2 + \left(\frac{\partial h}{\partial T_s}\delta T_s\right)^2 + \left(\frac{\partial h}{\partial T_j}\delta T_j\right)^2\right]^{\frac{1}{2}} \quad \text{(B.25.2)}$$

$$\delta h = \left[\left(\frac{1}{T_s - T_j}\cdot\delta q\right)^2 + \left(\frac{-q}{(T_s - T_j)^2}\cdot\delta T_s\right)^2 + \left(\frac{q}{(T_s - T_j)^2}\cdot\delta T_j\right)^2\right]^{\frac{1}{2}}$$

$$\frac{\delta h}{h} = \left[\left(\frac{\delta q}{q}\right)^2 + \left(-\frac{\delta T_s}{T_s - T_j}\right)^2 + \left(\frac{\delta T_j}{T_s - T_j}\right)^2\right]^{\frac{1}{2}} \quad \text{(B.25.3)}$$

B.5.9. Nusselt number

With the heat transfer coefficient and thermal conductivity of the HTF known, the Nusselt number was calculated using the relation presented by equation B.26.1 as follows:

$$Nu = \frac{hD_j}{k} \quad \text{(B.26.1)}$$

Therefore, the following expression was used to determine the uncertainty of the Nusselt number:

$$\delta Nu = \left[\left(\frac{\partial Nu}{\partial h}\cdot \delta h\right)^2 + \left(\frac{\partial Nu}{\partial D_j}\cdot \delta D_j\right)^2 + \left(\frac{\partial Nu}{\partial k}\cdot \delta k\right)^2\right]^{\frac{1}{2}}$$

$$\delta Nu = \left[\left(\frac{D_j}{k}\cdot \delta h\right)^2 + \left(\frac{h}{k}\cdot \delta D_j\right)^2 + \left(-\frac{h\cdot D_j}{k^2}\cdot \delta k\right)^2\right]^{\frac{1}{2}} \quad \text{(B.26.2)}$$

Equation B.26.2 was further simplified based on the assumption that the provided nozzle diameter, as stated by the manufacturer, was 100% correct. The resulting expression is as follows:

$$\delta Nu = \left[\left(\frac{D_j}{k}\cdot \delta h\right)^2 + \left(-\frac{h\cdot D_j}{k^2}\cdot \delta k\right)^2\right]^{\frac{1}{2}}$$

Combining equations B.26.1 and B.26.2 produced the following equation that was used to approximate the total uncertainty in the calculated Nusselt number:

$$\frac{\delta Nu}{Nu} = \left[\left(\frac{\delta h}{h}\right)^2 + \left(-\frac{\delta k}{k}\right)^2\right]^{\frac{1}{2}} \quad \text{(B.26.3)}$$

B.6. Results

By means of the information and relations described in Sections B.3 to B.5, the various levels of uncertainties relating to the current experimental investigation were determined. Therefore, Sections B.6.1 to B.6.3 present the appropriate instrumental, fluid property and calculated parameter uncertainties.

B.6.1. Instruments

Table B.2 depicts the associated uncertainties of the various instrumentation used during the experimental investigation.

Table B.2. Instrumental measurement uncertainties

Instrument	Range	Uncertainty
Thermocouple	< 150 ℃	0.12 ℃
Flow meter	0 - 50 L/min	± 0.01% of full range and 2% of measured value
Amp meter	0 – 2.5 A	2% of nominal value
Voltmeter	0 – 300 V	1.7% of nominal value
Vernier Caliper	0-150 mm	0.02 mm

B.6.2. Fluid properties

The calculated uncertainties of the various HTFs used in the experimental runs are presented in Table B.3.

Table B.3. Fluid property uncertainties

Property	Water	0.025 Vol. %	0.05 Vol. %	0.1 Vol. %	0.25 Vol. %	0.5 Vol. %	1 Vol. %
$\rho\ [kg/m^3]$	0.003%	0.003%	0.003%	0.003%	0.003%	0.003%	0.003%
$c_p\ [J/kg \cdot K]$	0.04%	0.044%	0.044%	0.044%	0.043%	0.043%	0.042%
$k\ [W/m \cdot K\ ]$	2%	2%	2%	2.01%	2.03%	2.05%	2.12%
$\mu\ [kg/m \cdot s]$	1%	1%	1%	1%	1%	1%	1%

B.6.3. Calculated parameters

By means of equations B.16.1 to B.23.2, the following uncertainties were calculated for the parameters that were fixed during the different experimental runs:

- $\delta\bar{T}_s$ = 0.047 ℃
- $\delta\bar{T}_e$ = 0.046 ℃
- δT_b = 0.061 ℃
- $\frac{\delta\dot{m}}{\dot{m}}$ = 2%
- $\frac{\delta U}{U}$ = 2%
- $\frac{\delta A_s}{A_s}$ = 0.095%
- $\frac{\delta Re}{Re}$ = 2.24%
- $\frac{\delta\dot{Q}_{elec}}{\dot{Q}_{elec}}$ = 5.95%

Concerning the other calculated parameters pertaining to the experimental investigation, Table B.4 presents the appropriate uncertainties for all volume fractions of TiO_2-water nanofluids.

Table B.4. Uncertainties of calculated parameters for varying volume fractions of TiO_2-water nanofluid

Parameter	Uncertainty at particle volume fraction						
	0%	0.025%	0.05%	0.1%	0.25%	0.5%	1%
$\dot{q}$	0.15%	0.15%	0.15-0.16%	0.15%	0.14-0.15%	0.14-0.15%	0.14-0.15%
h	1.75-3.55%	1.37-3.17%	1.38-3.33%	1.69-3.26%	1.58-2.9%	1.26- 2.99%	1.28-2.92%
Nu	2.66-4.08%	2.43-3.75%	2.43-3.88%	2.63-3.83%	2.57- 3.54%	2.41- 3.63%	2.47-3.61%

B.7. Conclusion

This section presented the uncertainty analysis used during the experimental investigation as well as the resulting instrumental, fluid thermophysical property and calculated parameter uncertainties. Additionally, it also defined the linear regression analysis that was used for approximating the uncertainties of the various thermocouples used in the investigation.

B.8. Nomenclature

A	Area	m^2
b	Bias	
c_p	Specific heat	$J/kg \cdot K$
$\hat{c}$	Best-fit intercept	
D	Diameter	m
h	Heat transfer coefficient	$W/m^2 \cdot K$
I	Current	A
k	Thermal conductivity	$W/m \cdot K$
M	Measuring points	
$\hat{m}$	Best-fit slope	
$\dot{m}$	Mass flow rate	kg/s
N	Number of data points	
Nu	Nusselt number	
p	Precision	
$\dot{Q}$	Heat input	W
$\dot{q}$	Heat flux	W/m^2
R	Result	
Re	Reynolds number	
S_{xx}	Sum of the squares of x	
S_{xy}	Sum of the squares of x and y	
S_{yx}	Standard error of best fit	
S_{yy}	Sum of the squares of y	
T	Temperature	℃ or K
t	*t*-variable	
U	Velocity	m/s
V	Voltage	V
$\dot{V}$	Volume flow rate	m^3/s
x	*x*-axis variable	
$\bar{x}$	Mean *x*-variable	
y	*y*-axis variable	
$\bar{y}$	Mean *y*-variable	

B.8.1. Subscripts

b	Bulk fluid
bf	Base fluid
ci	Calculated value
e	Exit
$elec$	Electrical
i	Index
j	Jet
nf	Nanofluid
np	Nanoparticle
s	Surface

B.8.2. Greek letters

δ	Uncertainty	
ρ	Density	kg/m^3
μ	Dynamic viscosity	$kg/m \cdot s$

φ	Particle volume fraction	%